



저작자표시 2.0 대한민국

이용자는 아래의 조건을 따르는 경우에 한하여 자유롭게

- 이 저작물을 복제, 배포, 전송, 전시, 공연 및 방송할 수 있습니다.
- 이차적 저작물을 작성할 수 있습니다.
- 이 저작물을 영리 목적으로 이용할 수 있습니다.

다음과 같은 조건을 따라야 합니다:



저작자표시. 귀하는 원저작자를 표시하여야 합니다.

- 귀하는, 이 저작물의 재이용이나 배포의 경우, 이 저작물에 적용된 이용허락조건을 명확하게 나타내어야 합니다.
- 저작권자로부터 별도의 허가를 받으면 이러한 조건들은 적용되지 않습니다.

저작권법에 따른 이용자의 권리는 위의 내용에 의하여 영향을 받지 않습니다.

이것은 [이용허락규약\(Legal Code\)](#)을 이해하기 쉽게 요약한 것입니다.

[Disclaimer](#) 

공학박사 학위논문

**Development of Practical Method for
Prediction of Cavitation Erosion with
Turbulent Flow using
Computational Fluid Dynamics
- Cavitation Erosion Prediction -**

전산유체역학을 이용한 난류 유동의 캐비테이션
침식 추정을 위한 실용적인 방법 개발

2013년 2월

서울대학교 대학원

산업조선공학부

박 선 호

**Development of Practical Method for
Prediction of Cavitation Erosion with
Turbulent Flow using
Computational Fluid Dynamics
- Cavitation Erosion Prediction -**

지도 교수 이 신 형

이 논문을 공학박사 학위논문으로 제출함
2013년 2월

서울대학교 대학원
산업조선공학부
박 선 호

박선호의 박사 학위논문을 인준함
2013년 2월

위 원 장 _____ (인)

부위원장 _____ (인)

위 원 _____ (인)

위 원 _____ (인)

위 원 _____ (인)

Abstract

**Development of Practical Method for
Prediction of Cavitation Erosion with
Turbulent Flow using
Computational Fluid Dynamics**

Sunho Park

Dept. Industrial Engineering and Naval Architecture

The Graduate School

Seoul National University

Cavitation erosion can be observed on hydraulic mechanical devices and has long been studied, yet a difficult research subject for many years. In the present study, a practical method to predict cavitation erosion, which caused a critical damage on hydraulic machineries, was developed.

Impact and critical velocities were defined to develop a practical method for the prediction of cavitation erosion. When the impact velocity was larger than the critical velocity, it was predicted that cavitation erosion could be observed. To close the practical method, the computational fluid dynamics (CFD) was introduced.

To simulate cavitating flows using CFD, pressure-based incompressible and isothermal compressible flow solvers based on a cell-centered finite volume method were developed using the open source libraries, respectively. Time derivative terms were discretized using the first-order accurate backward implicit scheme. Second order accurate discretized scheme was

applied it to the convection and diffusion terms.

To validate the developed solvers, incompressible and isothermal compressible cavitating flows were studied carefully and validated against existing experimental data. An incompressible flow with sheet, super, and cloud cavitations were simulated. A sheet cavitating flow around a hemispherical head-form body was simulated, and selected cavitation and turbulence models. A sheet cavitating flow around a modified NACA66 section (Brockett, 1966) was simulated and tested for various condensation and evaporation model constants. From the simulation of sheet cavitation, model constants were selected carefully. A super-cavitating flow behind a wedge-shaped cavitator was simulated. The computed cavity lengths on the body were compared with an analytic solution and numerical results using a potential flow solver. Fairly good agreement was observed in the three-way comparison. And then, a super cavitating flow around a body equipped with a cavitator was simulated and validated by comparisons with existing experimental data. A cloud cavitating flow around a three-dimensional twisted hydrofoil (Foeth, 2008) was simulated, and the cavity shedding dynamics by a re-entrant jet and a side entrant jet were investigated in terms of the cavity shedding cycles. The computed lift force and Strouhal number were compared against existing experimental data. From the results, the developed solver predicted well the incompressible cavitating flows. An isothermal compressible sheet cavitating flow around a hemispherical head-form body was simulated. The cavity shedding behavior, length of a re-entrant jet, drag history, and Strouhal number were investigated. Based on the results, it was confirmed that computations of the cavitating flow including compressibility effects improved the reproduction of cavitation dynamics. Thus, the isothermal compressible cavitating flow solver was selected to simulate the flow with cavitation erosion.

To close the practical method for the prediction of cavitation erosion,

cavitating flows with erosion in a converging-diverging nozzle (Keil et al., 2011) and around a hydrofoil (Dular and Coutier-Delgosha, 2009) were simulated by developed and validated code. From the simulations, the cavitation erosion coefficients were calculated. Based on the CFD results, the cavitation erosion coefficient was derived by a metamodeling and curve fitting methods. A kriging metamodel, which had an advantage in a non-linear problem, was selected. The cavitation erosion coefficient surface, which consisted of the cavitation and Reynolds numbers, was introduced by the kriging metamodel. In a curve fitting method, the cavitation erosion coefficient was formulated as the function of the cavitation and Reynolds numbers. A function of the cavitation number was formulated as an exponential function, while, a function of the Reynolds number was formulated as a log function for a slight change at high Reynolds number.

A cavitating flow in an axisymmetric nozzle followed by radial divergence (Franc, 2009) was simulated to validate the developed practical method. Predicted damage extent showed acceptable agreement with the existing experimental data. For the application to a propeller, a cavitating flow around a propeller was simulated. Predicted damage extent showed similar with damaged full-scale propeller blade.

The developed practical method helps predict cavitation erosion observed on the blades of pumps, turbines, and propellers. The prediction method including a bubble cavitation, fatigue of a material, high Reynolds number, and cavity shedding cycle is needed.

Keywords: Cavitation, Cavitation Erosion, Computational Fluid Dynamics (CFD)

Student Number: 2009-30283

Contents

List of Tables.....	vi
List of Figures.....	vii
Nomenclature.....	xii
Chapter 1 Introduction.....	1
1.1 Background.....	1
1.2 Literature review.....	3
1.2.1 Cavitation.....	3
1.2.2 Cavitation erosion.....	7
1.3 Objectives.....	9
Chapter 2 Development of Practical Method.....	11
2.1 Impact velocity.....	11
2.2 Critical velocity.....	14
Chapter 3 Code Development.....	17
3.1 Incompressible flow solver.....	18
3.1.1 Mathematical modeling.....	18
3.1.2 Pressure-correction equation.....	23
3.2 Isothermal compressible flow solver.....	26
3.2.1 Mathematical modeling.....	26
3.2.2 Pressure-correction equation.....	26
3.3 Numerical methods.....	30

Chapter 4 Code Validation.....	32
4.1 Incompressible flow.....	32
4.1.1 Sheet cavitation.....	32
4.1.2 Super cavitation.....	57
4.1.3 Cloud cavitation.....	80
4.2 Isothermal compressible flow.....	100
Chapter 5 Cavitation Erosion Coefficient.....	113
5.1 Converging-diverging nozzle.....	113
5.2 Hydrofoil.....	121
5.3 Determination of cavitation erosion coefficient.....	125
5.3.1 Kriging metamodeling method.....	126
5.3.2 Curve fitting method.....	130
Chapter 6 Validation and Application.....	135
6.1 Validation.....	135
6.2 Application.....	142
Chapter 7 Conclusions.....	152
Chapter 8 Future Works.....	154
References.....	155
Appendix.....	166
Abstract (Korean).....	176

List of Tables

Table 1. Formulas of barotropic relation-based cavitation model.....	21
Table 2. Formulas of two phase mixture flow model.....	23
Table 3. Test conditions of 2D modified NACA66 hydrofoil.....	48
Table 4. Test conditions of wedge-shaped cavitator.....	59
Table 5. Numerical uncertainty assessment.....	63
Table 6. Cavity lengths behind wedge-shaped cavitator.	70
Table 7. Velocity along cavity interface.	72
Table 8. Test conditions of 3D twisted hydrofoil.....	83
Table 9. Coarse, medium, and fine meshes for 3D twisted hydrofoil.	84
Table 10. Numerical uncertainty assessment of isothermal compressible flow code.	100
Table 11. Test conditions of converging-diverging nozzle.	114
Table 12. Cavitation erosion coefficient of converging-diverging nozzle....	121

List of Figures

Figure 1. Cavitation erosion on rudder surface.....	2
Figure 2. Cavitation erosion on blade surface (Krella and Steller, 2011).....	2
Figure 3. Category of cavitation models.	5
Figure 4. Normal shock configuration.	15
Figure 5. Flow chart of incompressible flow solver.....	25
Figure 6. Flow chart of isothermal compressible flow solver.....	29
Figure 7. Boundary conditions and domain extent.	34
Figure 8. Mesh for hemispherical head-form body.	34
Figure 9. Influence of cavitation model.	37
Figure 10. Influence of turbulence model.	39
Figure 11. Contours of right-hand side terms in cavitation model (Singhal et al., 2002).....	40
Figure 12. Influence of cavitation number.	41
Figure 13. Pressure coefficient contours and streamlines around hemispherical head-form body.	44
Figure 14. Vapor volume fraction contours around hemispherical head-form body.....	46
Figure 15. Cavity inception and closure region.	50
Figure 16. Influence of evaporation and condensation coefficients at cavity closure.	51
Figure 17. Influence of evaporation and condensation coefficients at cavity inception.	52
Figure 18. Pressure coefficient distribution on suction side of hydrofoil with leading edge cavitation.....	54
Figure 19. Liquid volume fraction contours with angle of attack of 4 degrees.	55
Figure 20. Pressure coefficient distributions on suction side of hydrofoil with	

mid-chord cavitation.	56
Figure 21. Liquid volume fraction contours with angle of attack of 1 degree.	57
Figure 22. Problem description of wedge-shaped cavitator.....	58
Figure 23. Boundary conditions and domain extent.	60
Figure 24. Mesh for wedge-shaped cavitator.....	61
Figure 25. Streamwise velocity component contours without cavitation of wedge angle of 45 degrees.	64
Figure 26. Pressure coefficient contours without cavitation of wedge angle of 45 degrees.....	64
Figure 27. Initial cavity of wedge angle of 45 degrees.	65
Figure 28. Fully developed cavity of wedge angle of 45 degrees.....	66
Figure 29. Streamwise velocity component contours in cavitating flow of wedge angle of 45 degrees.	67
Figure 30. Pressure coefficient contours in cavitating flow of wedge angle of 45 degrees.....	67
Figure 31. Turbulent eddy viscosity contours in cavitating flow of wedge angle of 45 degrees.	68
Figure 32. Streamwise velocity component contours in cavitating flow of wedge angle of 15 degrees.	68
Figure 33. Cavity lengths behind wedge-shaped cavitator.	71
Figure 34. Body with cavitator geometry and cavitation tunnel extent (unit: <i>mm</i>).	73
Figure 35. Mesh for body with cavitator.	74
Figure 36. Volume fraction contours of body with cavitator.	76
Figure 37. Volume fraction contours of body with cavitator with cavitation number of 1.....	77
Figure 38. Vapor volume fraction contours and meshes behind body with cavitator with cavitation number of 1.	78

Figure 39. Snap shot of cavity around cavitator with body in experiment.	79
Figure 40. Comparison of cavity lengths for body with cavitator.....	79
Figure 41. Top, side and front view of 3D twisted hydrofoil.	81
Figure 42. Spanwise distribution of angle of attack.....	82
Figure 43. Boundary conditions and domain extent.	84
Figure 44. Mesh for 3D twisted hydrofoil.....	85
Figure 45. Pressure coefficient distributions at mid-span section of hydrofoil in non-cavitating flow.	86
Figure 46. Pressure coefficient distributions on pressure and suction sides...	87
Figure 47. Pressure coefficient distributions at mid-span section of hydrofoil in cavitating flow.	89
Figure 48. Cavity shedding cycle – view from above suction side (left: present, right: data).	92
Figure 49. Vectors on cavity interface (left: cavity bottom, right: cavity top).	93
Figure 50. Cavity shedding cycle - view from side of mid-span plane (left: present, right: data).	94
Figure 51. Streamlines on cavity and pressure coefficient distributions on hydrofoil.....	97
Figure 52. Cavity roll up due to upstream re-entrant jet and external flows. .	98
Figure 53. Lift force coefficient history in cavitating flow.	99
Figure 54. Pressure coefficient distribution influenced by compressibility..	103
Figure 55. Volume fraction contours after cavity fully developed.....	105
Figure 56. Volume fraction contours with the greatest length of re-entrant jet.	106
Figure 57. Streamwise velocity component contours and streamlines with the greatest length of re-entrant jet.	108
Figure 58. Turbulent viscosity contours with the greatest length of re-entrant jet.	109

Figure 59. Drag coefficient history in surface of $0 \leq x/D \leq 2$	110
Figure 60. Strouhal number.....	111
Figure 61. Problem description of converging-diverging nozzle.....	114
Figure 62. Boundary conditions and domain extent of converging-diverging nozzle.....	115
Figure 63. Mesh for converging-diverging nozzle.....	116
Figure 64. Sheet cavity length of converging-diverging nozzle.....	117
Figure 65. Pressure difference of converging-diverging nozzle.....	119
Figure 66. Damage extent by cavitation erosion of converging-diverging nozzle (Keil et al., 2011).....	120
Figure 67. Problem description of hydrofoil.....	122
Figure 68. Boundary conditions and domain extent of hydrofoil.....	123
Figure 69. Mesh for Hydrofoil.....	123
Figure 70. Pressure difference on hydrofoil surface.....	124
Figure 71. Predicted cavitation erosion coefficient by kriging metamodel (circle symbol: design points).....	130
Figure 72. Pressure difference for cavitation number.....	132
Figure 73. Pressure difference for Reynolds number.....	133
Figure 74. Problem description of axisymmetric nozzle followed by radial divergence.....	136
Figure 75. Boundary conditions and domain extent of axisymmetric nozzle followed by radial divergence.....	138
Figure 76. Pressure coefficient contours of axisymmetric nozzle followed by radial divergence.....	139
Figure 77. Vapor volume fraction contours of axisymmetric nozzle followed by radial divergence.....	140
Figure 78. Pressure difference of axisymmetric nozzle followed by radial divergence.....	141

Figure 79. Principal particulars of KP505.....	143
Figure 80. Mesh for KP505 propeller blade.....	145
Figure 81. Pressure coefficient contours on pressure blade.....	147
Figure 82. Pressure coefficient contours on suction blade.....	148
Figure 83. Cavitation on KP505 propeller blade.....	149
Figure 84. Predicted cavitation erosion extent on KP505 propeller blade. ..	150
Figure 85. Cavitation erosion on propeller blade.....	151

Nomenclature

c	Speed of sound [m/s]
C_{ce}	Cavitation erosion coefficient [-]
C_{cond}	Condensation coefficient [-]
C_{evap}	Evaporation coefficient [-]
C_P	Pressure coefficient [-]
C_D	Drag force coefficient [-]
C_L	Lift force coefficient [-]
D	Diameter of hemisphere [m]
H	Channel height [-]
I	Unit tensor [-]
k	Turbulent kinetic energy [m^2/s^2]
L_{ch}	Characteristic length [m]
l_c	Cavity length [m]
l_w	Wedge length [m]
n_o	Nuclei concentration per unit volume of pure liquid [-]
P	Static pressure [Pa]
p	Estimated order of accuracy of computational method [-]
P_{atm}	Ambient pressure [Pa]
P_o	Reference pressure [Pa]
P_Y	Yield stress [Pa]
P_v	Vapor pressure [Pa]
R	Radius of bubble [m]

RE	Richardson extrapolated value [-]
Re	Reynolds number [-]
s	Entropy [J/K]
St	Strouhal number [-]
U_c	Total velocity along cavity boundary [m/s]
U_∞	Free stream velocity [m/s]
\vec{v}_m	Velocity vector [m/s]
y_o	Wedge height [m]
α	Volume fraction [-]
ε	Turbulent dissipation rate [m^2/s^3]
γ	Specific-heat ratio [-]
μ	Viscosity [kg/m-s]
μ_{eff}	Effective viscosity [kg/m-s]
μ_t	Turbulent viscosity [kg/m-s]
ν_t	Turbulent eddy viscosity [m^2/s]
ρ	Density [kg/m ³]
σ	Cavitation number [-]
$\overline{\tau}$	Turbulent stress tensor [Pa]
ϕ	Wedge angle [°]
ω	Dissipation per unit turbulence kinetic energy [s^{-1}]
φ	Computational solution variable for uncertainty assessment [-]

Chapter 1. Introduction

1.1 Background

Cavitation is observed in many hydrodynamic mechanical devices, such as marine propellers, pumps, turbines and nozzles, and can have an intensive effect on the performance of these devices. Cavitation causes erosion and abrasion of a metal surface, and vibration and noise in a system. Among those disadvantages of cavitation, especially, cavitation erosion on a metal surface, which causes performance reduction or defect for hydrodynamic machineries, is significant, as shown in Figure 1 and Figure 2.

The prediction method for cavitation erosion was not studied so much, while, the mechanism of cavitation erosion was done by many researchers. Thus, the prediction method for cavitation erosion has been needed and issued for decades.



Figure 1. Cavitation erosion on rudder surface.



Figure 2. Cavitation erosion on blade surface (Krella and Steller, 2011).

1.2 Literature review

1.2.1 Cavitation

A large amount of knowledge concerning cavitation in the form of thousands of studies has been compiled over the past few decades. In recent years, due to the development of computational fluid dynamics (CFD) and computing resources, numerical studies of cavitation mathematical modeling have advanced rapidly. To capture the cavitation phenomenon numerically, additional equations, such as the barotropic relation, or volume fraction transport equations have been introduced. These are generally known as “cavitation models.” Cavitation models are divided into the Lagrangian (discrete bubble) and Eulerian (continuum) approaches according to their computational framework, as summarized in Figure 3. The Lagrangian approach focuses on the behavior of discrete bubbles using bubble tracking and bubble dynamics equations. Chahine (2004) computed the cavitation inception and noise of a marine propeller using this approach. The Eulerian approach is based on an approximation of a homogeneous mixture flow. The mixture flow moves at the same velocity, and each phase is identified by solving a volume fraction transport equation. The Eulerian approach was divided into the barotropic relation model and two phase mixture flow model. The barotropic relation model solves a single continuity equation with a

barotropic relation equation between the pressure and density (Delannoy and Kueny, 1990; Kubota et al., 1992; Chen and Heister, 1994). On the other hand, the two-phase mixture flow model deals with two-phase continuity equations by employing a volume fraction transport equation (Merkle et al., 1998; Kunz et al., 1999; Ahuja et al., 2001; Schnerr and Sauer, 2001; Singhal et al., 2002). Transport equations have been implemented by many different developers and have shown reasonable results against existing experimental data. Park and Rhee (2010) summarized the characteristics of various ad-hoc cavitation models for CFD. Along with cavitation models, research on numerical schemes for the cavitating flow simulations has been done. Edwards et al. (2000) presented a preconditioned variant of the advective upwind splitting method-plus (AUSM+) low-diffusion flux-splitting scheme. Kunz et al. (2000) suggested a preconditioning strategy with favorable eigen-system characteristics and a block implicit dual-time solution strategy for a high-density-ratio cavitating flow. Senocak and Shyy (2002) developed a pressure-velocity-density scheme into a pressure correction equation and applied upwind density interpolation in the cavity region. Bilanceri et al. (2006) suggested an implicit low-diffusive Harten-Lax-van Leer (HLL) scheme with implicit time advancing for a barotropic cavitating flow.

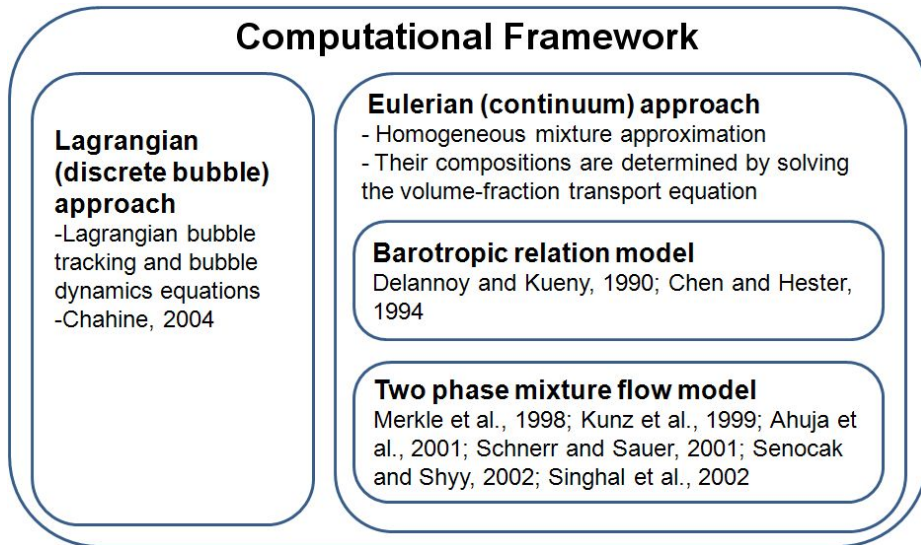


Figure 3. Category of cavitation models.

Besides general cavitating flows, many studies on super-cavitating flows have been done using experimental and numerical methods. Experimental methods rely mostly on pressure measurements and image process technology. Hrubec (2001) studied super-cavitating underwater projectiles using images and analyzed the flight behavior, stability mechanism, cavity shape and in-barrel launch characteristics. Wu and Chahine (2007) observed super-cavitation behind a simulated projectile head and measured the properties of the fluid inside the super-cavity. Li et al. (2008) studied a cavitating flow visualization using a high-speed camera and detailed velocity measurements using a particle image velocimetry (PIV) to offer information for validating computational models. Varghese et al. (2005) modeled super-cavitation using a steady potential flow boundary element method (BEM)

and studied various conditions including cavity closure on the conical/cylindrical portions of a vehicle, variants in the cone angle, and the variation in the radius of the cylindrical section. Shafaghat et al. (2009) studied the shape optimization of two-dimensional (2D) cavitators using a multi-objective optimization algorithm and BEM. Nouri and Eslamdoost (2009) developed an iterative algorithm to obtain the cavity length and applied it to a super-cavitating potential flow by BEM. Ahn et al. (2010) computed the cavity lengths generated by a cavitator using a potential flow solver by BEM and validated their computations by experimental observation (2012). Serebryakov (2001) predicted super-cavitating flows based on slender body theory. Lindau et al. (2003) simulated a supercavitating flow around a flat disk cavitator geometry using the RANS approach. Hu et al. (2009) modified the dispersion-controlled dissipative (DCD) scheme, initially proposed for capturing shock waves in vapor dynamics, and applied it to a super-cavitating flow. Choi and Ruzzene (2006) described the stability characteristics of a super-cavitating vehicle using a finite element method (FEM). Lin et al. (2008) carried out a nonlinear analysis of the dive-plane dynamics of a super-cavitating body analytically and numerically. Howe et al. (2009) derived the approximate representation of the transfer function and directly determined the level of self-noise at the cavitator nose produced by ventilating vapor impinging on a vapor-liquid, super-cavity interface. Savchenko (2001) summarized problems and perspectives on super-cavitation.

1.2.2 Cavitation erosion

A wide range of experimental studies, that deal with problems from bubble dynamics to material tests, have been done to understand the phenomenon of cavitation erosion. Lush (1983) and Grant and Lush (1987) investigated a impact load of a bubble on plastic solid and bilinear elastic-plastic solid, respectively. Karimi and Avellan (1986) set up a cavitation erosion test facility and investigated the erosion mechanism. Okada et al. (1989) measured the pressure at collapse in cavitation bubbles. Richman and McNaughton (1990) showed a correlation of cavitation erosion behavior with the mechanical properties of metals. Soyama et al. (2001) suggested the threshold level of material to predict a cavitation erosion rates. Hattori and Nakao (2002) evaluated the volume loss rate in terms of the material hardness and the fatigue crack growth rate. Soyama and Futakawa (2004) and Franc (2009) measured the incubation time of cavitation erosion and erosion rate for various cavitating flow conditions. Hattori and Kishimoto (2008) tested cavitation erosion on stainless steel components and obtained a correlation of the Vickers hardness and cavitation erosion rate. Abouel-Kasem and Ahmed (2008) investigated the mechanism of cavitation erosion through observations of the removed particles from pure aluminum. Keil et al. (2011) observed the cloud cavitation and cavitation erosion in a converging-diverging nozzle, and defined a dimensionless damage function.

Thanks to the rapid advancement of computational fluid dynamics (CFD) and computing resources, numerical studies on cavitation erosion have been

tried recently. Fortes-Patella et al. (2001) calculated the material's response to the pressure wave impact using a finite element method (FEM). Schnerr et al. (2008) computed shock waves with sampling frequency of 18 MHz for a twisted hydrofoil. Sedlar et al. (2009) computed the shock wave energy dissipated during the bubble collapse using the pressure inside the bubble against the ambient liquid pressure to expand the bubble from the minimum to the maximum radius for a pump impeller. Dular and Coutier-Delgosha (2009) computed the pit area and compared its experimental data. Ochiai et al. (2009) proposed the prediction method for cavitation erosion using a one-way coupling method for analyses of a cavitating flow field and bubble motion in the flow.

Besides cavitation erosion mechanism and influence factor on erosion, many researchers have developed mathematical models to predict cavitation erosion. Kato et al. (1996) proposed a scenario for quantitative prediction of the impact force distribution on the solid surface caused by cavitation based on a model for an isolated implosion of a sing bubble in a finite space. Forstes-Patella et al. (2002) proposed the relation between the pressure wave energy, created by bubble collapses, and the pit volume, representing the solid damage, and evaluated numerically and experimentally for three materials, such as aluminum, copper, stainless steel. Berchiche et al. (2002) proposed cavitation erosion model for ductile materials using the strain profile and the stress-strain relationship of the material. Dular et al. (2007) performed cavitation erosion tests for simple-shaped hydrofoils and developed theoretical model, which could predict the pit extent. Hattori and Kishimoto

(2008) predicted the erosion rate with the Vickers hardness. Szkodo (2008) presented a mathematical model describing cavitation erosion resistance of materials based on Weibull's distribution. van Terwisga et al. (2009) reviewed physical mechanism and cavitation erosion models

1.3 Objectives

In the present study, a practical method for the prediction of cavitation erosion was suggested, and CFD analyses for cavitating flows were introduced to close a practical method. For the CFD analyses, an unsteady flow solver that couples velocity, phase compositions, and pressure was developed based on a cell-centered finite volume method. Turbulence was considered using the RANS approach. Thus developed solver, termed SNUFOAM-Cavitation, was validated by applying it to sheet, super, and cloud cavitating flows (Park and Rhee, 2012, 2013). SNUFOAM-Cavitation can handle both incompressible and compressible flows with multiple cavitation models based on a barotropic relation and two-phase mixture flow models.

The present study focused on the development of a practical method for the prediction of cavitation erosion. The objective therefore was as follows

- to develop a practical method for the predict of cavitation erosion

To achieve the main-objective, the sub-objectives were as follows

- to develop a CFD code to simulate cavitating flows
- to define the cavitation erosion coefficient using CFD
- to validate and apply the developed cavitation erosion prediction method

The paper is organized as follows. The development of a practical method for the prediction of cavitation erosion is presented first, and this is followed by the code development and validation. The cavitation erosion coefficient is introduced and discussed. The developed method is then validated and applied. Finally, the conclusions and future works are provided.

Chapter 2. Development of Practical Method

The cavity implosion generates a powerful jet near a solid surface and erodes the surface. When the jet velocity was larger than the critical velocity, cavitation erosion could be predicted on the surface. To predict cavitation erosion, the jet and critical velocities should be defined. Here, the jet velocity indicated an impact velocity to the surface, and the critical velocity indicated a threshold velocity, which deformed a solid surface. In this paper, the impact and critical velocities were defined as described below.

2.1 Impact velocity

When a spherical bubble with the incompressible flow in a quiescent fluid collapses near a solid surface, the jet reaches a high speed quite early in the collapse process. The jet velocity was found to be

$$v_{jet} = \gamma \sqrt{\frac{\Delta P}{\rho_l}} \quad (1)$$

where ρ_l was the fluid density, and ΔP was the pressure difference between the far-field pressure, which would maintain the bubble at equilibrium at its maximum or initial radius, and the far-field pressure present during a collapse. γ was related to the non-dimensional distance from the bubble center to the surface (Plesset and Chapman, 1971; Brennen, 1995). From the equation, it is

seen that the velocity was independent of the size of the bubble.

An unsteady cavity was not a single bubble in a spherical shape, while it was a group of bubbles. So the above equation could not be applied to agglomerated cavitating flow. Especially, in the computational analysis, a computed cavity structure was identified as a structure of vortices rather than a group of bubbles due to the assumption of the homogeneous mixture flow (Park and Rhee, 2013). Thus, another approach for the jet velocity was needed.

A jet velocity induced a cavity collapse that causes the pressure variation on a solid surface. The pressure difference between the far-field and pressure and the far-field pressure present during a collapse was replaced by the pressure difference between maximum and minimum pressures on the surface during a cavity shedding cycle. The liquid density was replaced by the mixture density to present the pressure shock wave. The variation of the pressure was replaced by the variation of the pressure and density because the pressure shock wave generated in the compressible flow. The new coefficient, which was the cavitation erosion coefficient, C_{ce} , was introduced. Thus, the impact velocity could be expressed as

$$\begin{aligned}
 v_{impact} &= C_{ce} \sqrt{\Delta \left(\frac{P}{\rho_m} \right)} \\
 &= C_{ce} \sqrt{\left(\frac{P}{\rho_m} \right)_{\max} - \left(\frac{P}{\rho_m} \right)_{\min}}
 \end{aligned} \tag{2}$$

where the subscript m indicates the “mixture phase.” C_{ce} was a cavitation erosion coefficient, related to dimensional variables which were the reference and vapor pressures, density, dynamic viscosity, velocity, characteristic length, and cavity shedding frequency. Using the Buckingham pi theorem, variables formed three pi groups, and C_{ce} was expressed as a function of the cavitation, Reynolds, and Strouhal numbers. C_{ce} was expressed as a multiplication form rather than a superposition form due to the velocity, which was a nonlinear variable. The cavitation, Reynolds, and Strouhal numbers influenced on C_{ce} independently, C_{ce} could be defined as

$$\begin{aligned}
 C_{ce} &= f(P_o, P_v, \rho, \mu, U, L, f) \\
 &= f\left(\frac{P_o - P_v}{\frac{1}{2}\rho U^2}, \frac{\rho UL}{\mu}, \frac{fL}{U}\right) \\
 &= f(\sigma, Re, St) \\
 &= f_1(\sigma) \times f_2(Re) \times f_3(St)
 \end{aligned} \tag{3}$$

The pressure in the RANS equations expressed a mean pressure. To express the instantaneous pressure and consider the effect of turbulence, a fluctuating pressure, P' , was added to the mean pressure. The fluctuating pressure was expressed as in Hinze (1975)

$$P' = 0.39\rho_m k \quad (4)$$

where k is the turbulent kinetic energy. Thus, ΔP calculated using both the pressure from the solution of the RANS equations and the fluctuating pressure.

2.2 Critical velocity

The impact of a plane-ended liquid mass on a plane solid surface was considered (Lush, 1983). The direction of motion of the liquid mass was at right angles to the surface, the plane end being parallel to the surface. When the liquid strikes this surface, a normal shock wave was propagated the liquid stream, and behind the shock the liquid velocity decreased and the pressure increased. Assuming, for the moment, the liquid stream was an isentropic and incompressible flow, a specific volume was constant. Thus, the flow treated as an isothermal flow.

$$dV = 0, c_p = c_v = c$$

$$ds \cong \frac{du}{T} \cong \frac{c}{T} dT \quad (5)$$

$$s_2 - s_1 = \int_1^2 c \frac{dT}{T} = c \ln\left(\frac{T_2}{T_1}\right)$$

where V was a specific volume, T was a temperature, s was a entropy, and c was specific heat ratio. Thus, from the assumption of an isentropic and incompressible flow, the impact velocity was derived excluding a temperature. Assuming, the liquid mass is infinitely wide, the problem could be analyzed in one-dimensional terms as shown in Figure 4. In a steady flow, the equation of continuity was

$$\rho_1(v+c) = \rho_2(u+c) \quad (6)$$

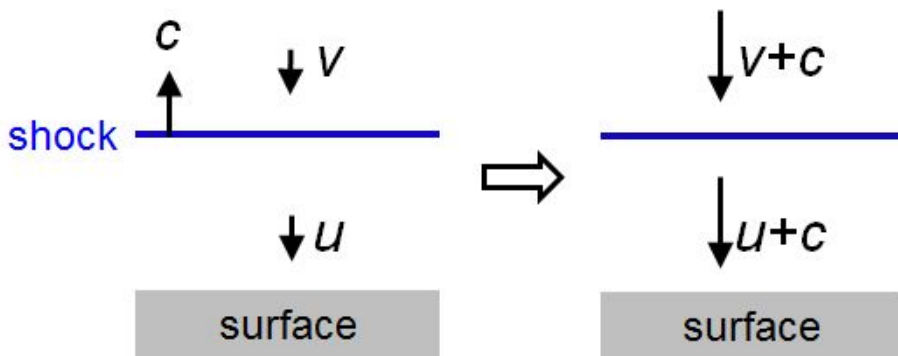


Figure 4. Normal shock configuration.

where v was the initial velocity, u was the velocity behind the shock, $-c$ was the velocity of the shock wave, ρ_1 was the ambient density of the liquid, and ρ_2 was the density behind the shock. The conservation of momentum could be shown

$$P - P_{atm} = \rho_l(v+c)(v-u) \quad (7)$$

where P_{atm} was the ambient pressure. The continuity and momentum equations could be solved by assuming that the relation for liquid had the form

$$\frac{P+B}{P_{atm}+B} = \left(\frac{\rho}{\rho_l} \right)^n \quad (8)$$

where $n = 7$ and $B = 300 \text{ MPa}$. The ambient pressure could be neglected due to the large value of the liquid and shock speeds. A critical value of the impact velocity, which causes plastic deformation on a solid surface, can be derived as

$$v_{critical} = \left[\frac{P_Y}{\rho} \left(1 - \left(1 + \frac{P_Y}{B} \right)^{-1/n} \right) \right]^{1/2} \quad (9)$$

where P_Y is the yield stress of the material. Here, n and B are 7 and 300 MPa, respectively (Lush, 1983). A surface could be eroded by a small impact velocity, which was smaller than the critical velocity, due to the fatigue. In this paper, however, the erosion by the fatigue was not considered.

Chapter 3. Code Development

Incompressible, isothermal compressible, and fully compressible cavitating flow codes were used to compute cavitating flows. An incompressible flow code didn't allow a density change in the liquid and vapor phases, and, thus, didn't well simulate a cavity dynamics. To compute cavity dynamics, therefore, isothermal compressible (Venkateswaran, et al., 2002) and fully compressible cavitating (Saurel and Lemetayer, 2001) flow codes were needed. In an isothermal compressible cavitating flow code, the densities of the liquid and vapor phases were assumed to be function of the pressure not the temperature, while, in a compressible cavitating flow code, the densities were assumed to be function of the temperature. This paper focused on the hydrodynamic machineries, which were operated without a big change in the temperature. Also, a temperature change caused by the cavitation in hydrodynamic mechanical devices was known to be very small (Shin, 2011). This paper didn't include the equation for the conservation of the energy and, thus, developed the isothermal compressible cavitating flow code to simulate a cavity dynamics.

3.1 Incompressible flow solver

3.1.1 Mathematical modeling

The equations for the mass and momentum conservation were solved to obtain the velocity and pressure fields. The equation for the conservation of mass, or the continuity equation, can be written as

$$\nabla \cdot (\rho \bar{v}_m) = 0 \quad (10)$$

where \bar{v} is the velocity vector. The subscript m indicates the “mixture phase.”

The equation for the conservation of momentum can be written as

$$\frac{\partial \rho_m \bar{v}_m}{\partial t} + \nabla \cdot (\rho \bar{v}_m \bar{v}_m) = -\nabla P + \nabla \cdot (\bar{\tau}) \quad (11)$$

where P is the static pressure and the turbulent stress tensor, $\bar{\tau}$, is given by

$$\bar{\tau} = \mu_{eff} \left[(\nabla \bar{v}_m + \nabla \bar{v}_m^T) - \frac{2}{3} \nabla \cdot \bar{v}_m I \right] \quad (12)$$

with the second term on the right-hand side representing the volume dilation effect, where $\mu_{eff} = \mu + \mu_t$, μ is the viscosity, and the subscripts *eff* and *t* denote “effective” and “turbulent,” respectively. I is the unit tensor.

The mixture properties of the density and viscosity are computed as a function of α , as

$$\rho_m = \alpha_v \rho_v + \alpha_l \rho_l \quad (13)$$

$$\mu_m = \alpha_v \mu_v + \alpha_l \mu_l \quad (14)$$

where α is the volume fraction, and subscripts v and l indicate “vapor” and “liquid,” respectively.

Once the Reynolds averaging approach for turbulence modeling is applied, the unknown term, i.e., the Reynolds stress term, is related to the mean velocity gradients by the Boussinesq hypothesis, as follows

$$-\rho \overline{v'v'} = \mu_t \left[\left(\nabla \overline{v} + \nabla \overline{v}^T \right) - \frac{2}{3} \left(\rho k + \mu_t \nabla \overline{v} \right) \right] I \quad (15)$$

The standard k - ε turbulence model, which is based on the Boussinesq hypothesis with transport equations for the turbulent kinetic energy (k) and its dissipation rate (ε) was adopted for turbulence closure (Launder and Spalding, 1972). The turbulent viscosity (μ_t) is computed by combining k and ε via $\mu_t = \rho C_\mu k^2 / \varepsilon$, and the turbulence kinetic energy and its rate of dissipation are obtained from the transport equations, which are

$$\frac{\partial}{\partial t}(\rho k) + \nabla \cdot (\rho k \bar{v}) = \nabla \cdot \left[\left(\mu + \frac{\mu_t}{\sigma_k} \right) \nabla k \right] + G_k + G_b - \rho \varepsilon - Y_M \quad (16)$$

$$\frac{\partial}{\partial t}(\rho \varepsilon) + \nabla \cdot (\rho \varepsilon \bar{v}) = \nabla \cdot \left[\left(\mu + \frac{\mu_t}{\sigma_\varepsilon} \right) \nabla \varepsilon \right] + \rho C_1 S \varepsilon - \rho C_2 \frac{\varepsilon^2}{k + \sqrt{v \varepsilon}} + C_{1\varepsilon} \frac{\varepsilon}{k} C_{3\varepsilon} G_b \quad (17)$$

where C_μ is an empirical constant of 0.09. Here, the model constants $C_{1\varepsilon}$, $C_{2\varepsilon}$, σ_k , and σ_ε are 1.44, 1.92, 1.0, and 1.3, respectively. The turbulent viscosity was used to calculate the Reynolds stresses to close the momentum equations. The wall function was used for the near-wall treatment.

The volume fraction transport equation was considered to account for the cavitation dynamics. The cavitation process was governed by the thermodynamics and the kinetics of the phase change dynamics in the system. In this paper, six cavitation models were tested to solve for the cavitating flow. The general form of the barotropic relation-based cavitation model can be expressed as

$$\left(\frac{P}{\rho} \right)_m = R_v \alpha_v \left(\frac{P}{\rho} \right)_v + R_l (1 - \alpha_v) \left(\frac{P}{\rho} \right)_l \quad (18)$$

Detailed formulas for the linear interpolation and Wallis model (1969) are given in Table 1. Here, the subscript *sat* indicates ‘‘saturated.’’ The Wallis model (1969) allowed smooth phase changes, and thus enhanced the numerical stability.

Table 1. Formulas of barotropic relation-based cavitation model.

	R_v	R_l
Linear interpolation	1	1
Wallis model (Wallis, 1969)	$(\alpha_v \rho_{v,sat} + (1 - \alpha_v) \rho_{l,sat}) \left(\frac{1}{\rho_{v,sat}} \right)$	$(\alpha_v \rho_{v,sat} + (1 - \alpha_v) \rho_{l,sat}) \left(\frac{1}{\rho_{l,sat}} \right)$

The transport equations for two-phase mixture flow models can be expressed in a general form as follows

$$\frac{\partial Q}{\partial t} + \nabla \cdot (E) = R_{cond} + R_{evap} + R_s \quad (19)$$

Each variable is presented in Table 2 for the cavitation models proposed by Merkle et al. (1998), Kunz et al. (1999), Schnerr and Sauer (2001), and Singhal et al. (2002). In the equation, except for the model proposed by Kunz et al. (1999), either evaporation (R_{evap}) or condensation (R_{cond}) source term was activated depending on the local pressure level compared to the vapor pressure. For example, when the local pressure was higher than the vapor pressure, the condensation source term was activated. In the model proposed by Kunz et al. (1999), the condensation source term was always

activated, while the evaporation source term was activated when the local pressure level was lower than the vapor pressure. Schnerr and Sauer's cavitation model (2001) assumed that the vapor consisted of mini-spherical bubbles, which were included in the model as a model constant. The cavitation model proposed by Singhal et al. (2002) used the turbulent kinetic energy in the evaporation and condensation terms. In these equations, L_{ch} is the characteristic length and U_∞ is the free-stream velocity. f_v is the vapor mass fraction, while α_v is the vapor volume fraction. σ_v is the turbulent Prandtl number for the vapor, γ is the surface tension, and v_{ch} is the characteristic velocity, which reflects the effect of the local slip velocity and takes a value approximately equal to \sqrt{k} with k being the local turbulent kinetic energy. The model constants, C_{cond} for condensation and C_{evap} for evaporation, were respectively set to 100 and 1 in Merkle et al. (1998), 1000 and 1000 in Kunz et al. (1999), 1 and 1 in Schnerr and Sauer (2001), 0.01 and 0.01 in Singhal et al. (2002). R is the radius of a bubble and computed as

$$R = \left(\frac{\alpha_v}{1 - \alpha_v} \frac{3}{4\pi} \frac{1}{n_o} \right)^{1/3} \quad (20)$$

where n_o is the nuclei concentration per unit volume of pure liquid. Here, n_o was set to 1×10^{13} following Schnerr and Sauer (2001).

Table 2. Formulas of two phase mixture flow model.

	Q	E	R_{cond}	R_{evap}	R_s
Merkle et al. (1998)	f_v	$f_v \vec{v}_m$	$-C_{cond} \frac{ P - P_v f_v}{\left(\frac{1}{2} \rho_l U_\infty^2\right) \left(\frac{L_{ch}}{U_\infty}\right)}$	$C_{evap} \frac{ P_v - P (1 - f_v)}{\left(\frac{1}{2} \rho_l U_\infty^2\right) \left(\frac{L_{ch}}{U_\infty}\right)}$	0
Kunz et al. (1999)	α_v	$\alpha_v \vec{v}_m$	$-C_{cond} \frac{\alpha_v (1 - \alpha_v)^2}{\left(\frac{L_{ch}}{U_\infty}\right)}$	$-C_{evap} \frac{MIN(P - P_v, 0) (1 - \alpha_v)}{\left(\frac{1}{2} \rho_l U_\infty^2\right) \left(\frac{L_{ch}}{U_\infty}\right)}$	0
Schnerr and Sauer (2001)	$\alpha_v \rho_v$	$\alpha_v \rho_v \vec{v}_m$	$-C_{cond} \frac{\rho_v \rho_l}{\rho_m} \alpha_v (1 - \alpha_v) \frac{3}{R} \sqrt{\frac{2}{3} \frac{P - P_v}{\rho_l}}$	$C_{evap} \frac{\rho_v \rho_l}{\rho_m} \alpha_v (1 - \alpha_v) \frac{3}{R} \sqrt{\frac{2}{3} \frac{P_v - P}{\rho_l}}$	0
Singhal et al. (2002)	$f_v \rho_m$	$f_v \rho_m \vec{v}_m$	$-C_{cond} \frac{\nu_{ch}}{\gamma} \rho_l \rho_l \sqrt{\frac{2}{3} \frac{P - P_v}{\rho_l}} f_v$	$C_{evap} \frac{\nu_{ch}}{\gamma} \rho_v \rho_l \sqrt{\frac{2}{3} \frac{P_v - P}{\rho_l}} (1 - f_v)$	$\nabla \cdot \left(\frac{\mu_l}{\sigma_v} \nabla f_v \right)$

3.1.2 Pressure-correction equation

The equation for the conservation of momentum was discretized as follows

$$a_p \vec{v}_p + \sum a_N \vec{v}_N = S - \nabla P \quad (21)$$

where the subscripts P and N denote an owner and neighbor cells, respectively. a_p and a_N are matrix coefficients of each cell. S is a source term. For simplicity, new operator ($H(\vec{v})$) was introduced which contains the off-diagonal part of the momentum equation matrix. Using the new operator, the equation for momentum conservation was written as

$$a_p \vec{v}_p = H(\vec{v}) - \nabla P \quad (22)$$

Substituting the expression for \vec{v}_p into the incompressible continuity equation, $\nabla \cdot \vec{v} = 0$, yielded

$$\nabla \cdot \left(\frac{1}{a_p} H(\vec{v}) \right) - \nabla \cdot \left(\frac{1}{a_p} \nabla P \right) = 0 \quad (23)$$

This is the form of the pressure-correction equation for incompressible flows. The flow chart of the incompressible flow solver is shown in Figure 5. The volume fraction transport and turbulence model equations were solved sequentially. The pressure and velocity were then solved by PISO algorithm (Issa, 1985), and finally the time step was increased. More details on the pressure-correction equation used are described in Kissling et al. (2010).

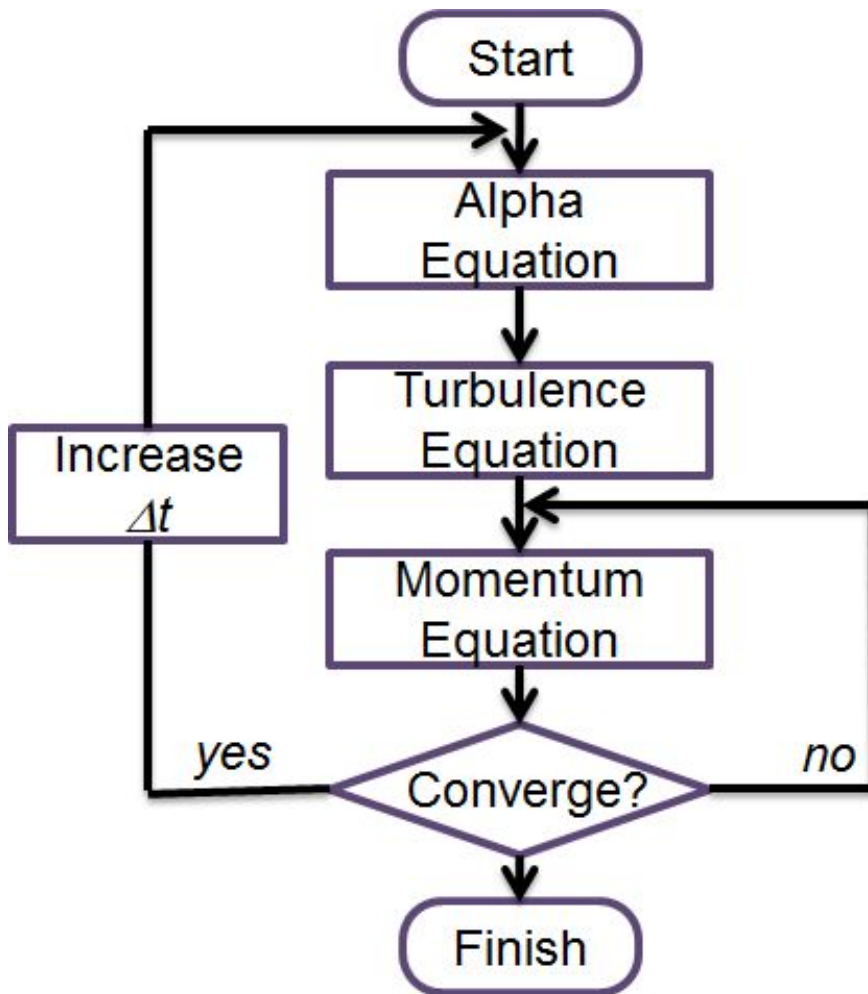


Figure 5. Flow chart of incompressible flow solver.

3.2 Isothermal compressible flow solver

3.2.1 Mathematical modeling

Different equation with the incompressible flow solver is the equation for the mass conservation. The equation for the conservation of mass, or the continuity equation, can be written as

$$\frac{\partial \rho_m}{\partial t} + \nabla \cdot (\rho_m \vec{v}_m) = 0$$
$$\frac{1}{\rho_m} \left(\frac{\partial \rho_m}{\partial t} + \vec{v}_m \cdot \nabla \rho_m \right) + \nabla \cdot \vec{v}_m = 0$$
(24)

3.2.2 Pressure-correction equation

In isothermal compressible flows, the density was not cancelled in the equation for the conservation of mass. The density can substitute for the pressure from the equation of state for both phases. The ideal gas equation of state for the vapor phase and the adiabatic or isentropic equation of state for the liquid phase were expressed as, respectively (Park et al., 2012)

$$\frac{P}{\rho} = \text{constant} \quad (25)$$

$$\left(\frac{\partial P}{\partial \rho} \right)_s = \frac{1}{c^2} \quad (26)$$

where c was the speed of sound.

The equation for momentum conservation for incompressible and isothermal compressible flows was same. Substituting the expression for \vec{v}_p into the isothermal compressible continuity equation, $\nabla \cdot \vec{v} = -\frac{1}{\rho} \left(\frac{\partial \rho}{\partial t} + \vec{v} \cdot \nabla \rho \right)$, yielded (Senocak and Shyy, 2002)

$$\frac{1}{P} \left(\frac{\partial P}{\partial t} + \nabla \cdot (\vec{v}P) - P \nabla \cdot \vec{v} \right) + \nabla \cdot \left(\frac{1}{a_p} H(\vec{v}) \right) - \nabla \cdot \left(\frac{1}{a_p} \nabla P \right) = 0 \quad (27)$$

This is the form of the pressure-correction equation for isothermal compressible flows. Here, $1/P$ was calculated using the harmonic relation.

$$\frac{1}{P} = \frac{1}{P_v} + \frac{1}{P_l} \quad (28)$$

Overall procedure of the developed isothermal compressible cavitating flow solver was similar to the code of Senocak and Shyy (2002). The

difference was the density variation of each phase. Senocak and Shyy (2002) used one equation to close the density for both phases.

$$\rho' = C(1 - \alpha_l)P' \quad (29)$$

where primed variables represented the correction terms. C was an arbitrary constant. Here, $C = 4$ was adopted. In the liquid phase, the variation of the density was not allowed, while, the variation of the density was allowed by the pressure variations in the vapor phase.

The flow chart of the isothermal compressible flow solver is shown in Figure 6. The difference between the incompressible and isothermal compressible flow solvers was the step of the continuity equation. In the isothermal compressible flow solver, the continuity equation was solved separately. However, in the incompressible flow solver, the continuity equation was included in the pressure-correction equation. The volume fraction transport, turbulence model, and continuity equations were solved sequentially. The pressure and velocity were then solved by PISO algorithm (Issa, 1985), and finally the time step was increased.

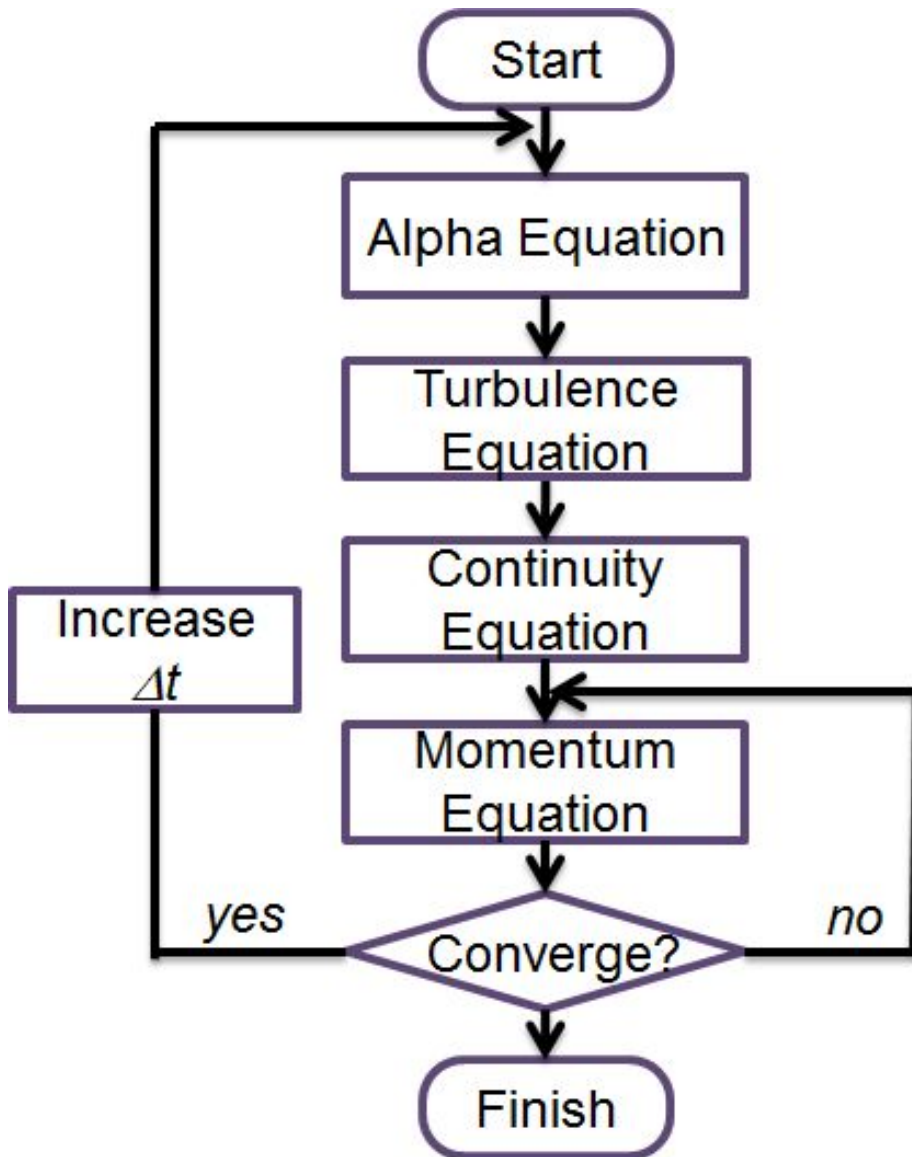


Figure 6. Flow chart of isothermal compressible flow solver.

3.3 Numerical methods

A pressure-based cell-centered finite volume method was employed along with a linear reconstruction scheme that allows the use of computational cells of arbitrary shapes. Time derivative terms were discretized using the first-order accurate backward implicit scheme, which has proved sufficient for engineering accuracy with carefully chosen time step sizes. The solution gradients at the cell centers were evaluated by the least-square method. The convection terms were discretized using the total variation diminishing (TVD) scheme, and the second-order accurate van Leer limiter (van Leer, 1979) was selected. The TVD scheme was written as

$$\phi_e = \phi_P + \frac{1}{2} \Psi(r)(\phi_E - \phi_P) \quad (30)$$

where the van Leer limiter (van Leer, 1979) was defined as

$$\Psi(r) = \frac{(r + |r|)}{1 + r} \quad (31)$$

where

$$r = \frac{(\phi_E - \phi_W)}{(\phi_E - \phi_P)} \quad (32)$$

where P was the cell center of a focusing cell, E and W were the cell center of the east and west cells, and e was the face center between E and P cells. For the diffusion terms, a central differencing scheme was used. The velocity–pressure coupling and overall solution procedure were based on a pressure-implicit with splitting order (PISO) type segregated algorithm (Issa, 1985) adapted to an unstructured grid. The discretized algebraic equations were solved using a pointwise Gauss–Seidel iterative algorithm, while an algebraic multi-grid method was employed to accelerate solution convergence.

Chapter 4. Code Validation

To validate the developed solvers, incompressible and isothermal compressible cavitating flows were studied carefully and validated against existing experimental data. An incompressible flow with sheet, super, and cloud cavitations, and an isothermal compressible flow with sheet cavitation were simulated.

4.1 Incompressible flow

4.1.1 Sheet cavitation

Sheet cavitation indicates the vapor which remains approximated at the same position. To validate developed code for sheet cavitating flows, cavitating flows around a hemispherical head-form body and modified NACA66 hydrofoil were (Brockett, 1966) simulated.

The cavitating flow around the hemispherical head-form body studied experimentally by Rouse and McNown (1948) was considered. Rouse and McNown (1948) carried out a series of experiments on natural cavitation around axi-symmetric configurations. Each configuration had a cylindrical

after-body with a flow-aligned axis and either hemispherical, conical, ogival or blunt fore-body shapes.

Figure 7 shows the solution domain extent and boundary conditions. The Dirichlet boundary condition, i.e., the specified value of the velocity, was applied on the inlet boundary. On the exit boundary, the reference pressure with extrapolated velocity and volume fraction values was applied. The reference pressure was fixed on the exit boundary with the desired cavitation number. The axi-symmetric condition was applied on the bottom left boundary. A no-slip condition was applied on the hemispherical head-form body surface. The solution domain extended $-30 \leq x/R \leq 50$ and $0 \leq y/R \leq 30$ in the streamwise and vertical directions, respectively. The domain was set large enough to minimize the influence of the inlet boundary. A C-type structured grid consisting of 11,900 cells, i.e., 170 cells on the body and 70 cells in the normal direction, was used (see Figure 8). For the mesh designed for the standard and realizable $k-\varepsilon$ turbulence models with a wall function, the growth ratio of the cell size was 1.05 and the non-dimensionalized cell height, z/D , off the wall was 0.004, which corresponded to y^+ of 50. For the mesh designed for the Spalart-Allmaras turbulence model (1972), the growth ratio of the cell size was the same, while the cell height off the wall was set to 2 in terms of y^+ to fully resolve the viscous sub-layer.

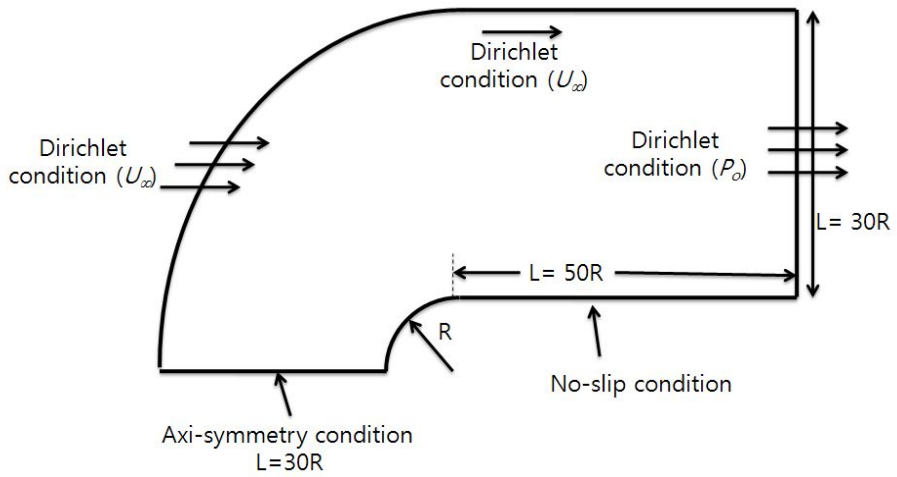


Figure 7. Boundary conditions and domain extent.

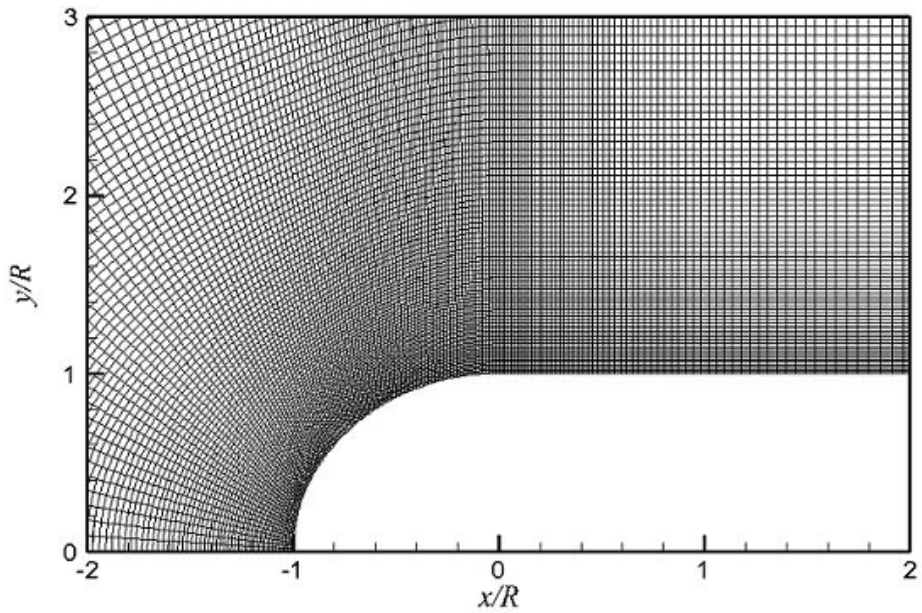


Figure 8. Mesh for hemispherical head-form body.

Unsteady computations were done for the Reynolds number (based on U_∞ value of 0.7 m/s and the diameter of the hemispherical head-form body of 0.2 m) of 1.36×10^5 and cavitation numbers of 0.2, 0.3, 0.4, and 0.5. The cavitation number (σ) was defined as

$$\sigma = \frac{P_o - P_v}{\frac{1}{2} \rho U_\infty^2} \quad (33)$$

where P_v was the vapor pressure and ρ was the density of the fluid. In the cavitating flow, cavitation modeling of the subject flow plays an important role; therefore, the selection of the model can affect the accuracy of the prediction significantly. In pursuit of highly accurate predictions, the barotropic relation and the two-phase mixture flow models were tested systematically.

To tame the computational instability caused by the large difference in the density and the high rate of mass transfer, the cavitating flow was computed with the converged single phase solution at a large cavitation number. The computations were progressed below the Courant number of 0.2 and the computation of each time step was finished when the scaled residuals for all the solution variables had dropped by at least six orders of magnitude.

First, the influence of the cavitation models with the standard $k-\varepsilon$ turbulence model (1972) was studied for the cavitation number of 0.3. Figure

9 shows the pressure coefficient (C_p) distribution on the hemispherical head-form body surface for various cavitation models. The pressure coefficient was defined as

$$C_p = \frac{P - P_o}{\frac{1}{2} \rho U_\infty^2} \quad (34)$$

The horizontal axis indicates the girth length on the surface nondimensionalized by the diameter of the hemisphere. The pressure overshoot at the cavity closure was more prominent in the computational results. Linear interpolation based the barotropic relation model showed the fastest cavity closure, while the cavity closure predicted by the Wallis (1969) barotropic relation model was in good agreement with the experimental results. However, the pressure after the cavity closure with the barotropic relation models was not recovered properly. On the other hand, all two-phase mixture flow models showed the correct pressure recovery after the cavity closure. The pressure behaviors upon the cavity closure predicted by the cavitation models of Merkle et al. (1998), Schnerr and Sauer (2001), and Singhal et al. (2002) were closer to that from the experiment compared to the cavitation model of Kunz et al. (1999). In SNUFOAM-Cavitation, based on this observation, the cavitation model of Singhal et al. (2002), which showed better convergence behavior, was selected.

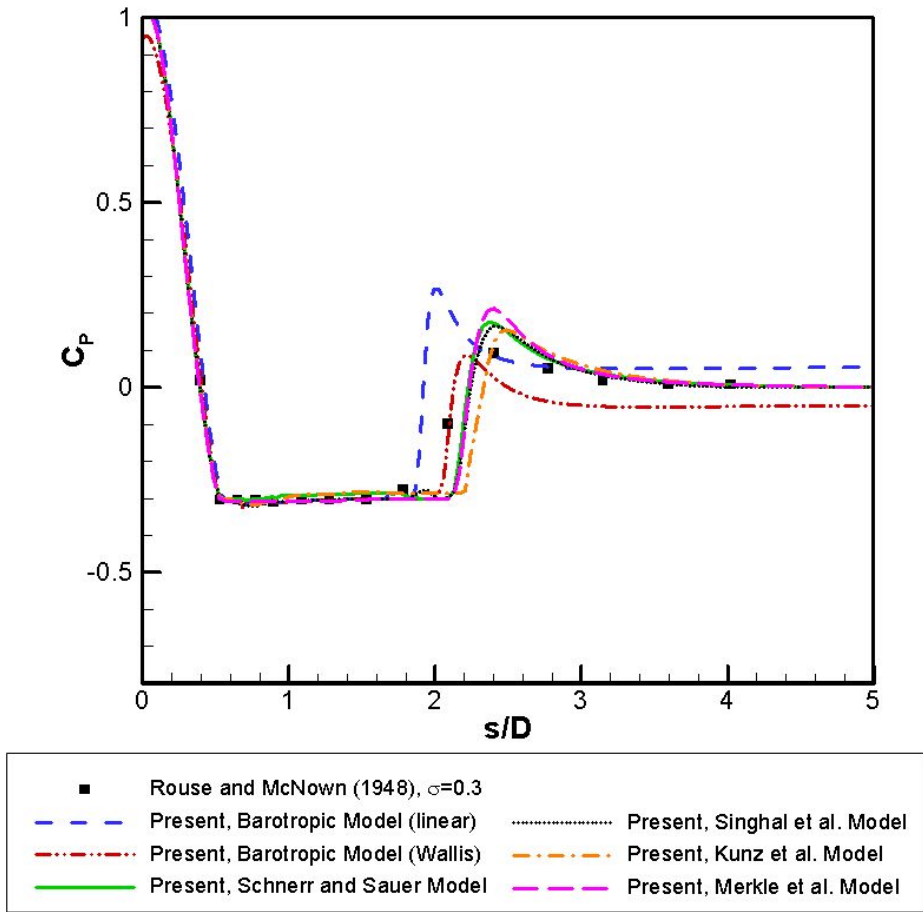


Figure 9. Influence of cavitation model.

The influence of turbulence models, Spalart-Allmaras (1992), standard $k-\varepsilon$ (1972), and realizable $k-\varepsilon$ (1995) models, with the selected cavitation model of Singhal et al. (2002) was investigated at a cavitation number of 0.3. The results are shown in Figure 10 and Figure 11. In Figure 10, the laminar flow results showed delayed cavity closure and a large pressure overshoot at the cavity closure. The results using the standard $k-\varepsilon$ turbulence model (1972), on the other hand, showed fairly good agreement. Figure 11 shows the contours of the right-hand side terms in the cavitation model, which indicate the magnitude of phase change. The magnitude of the right-hand side terms was large at the cavity interface due to the active phase change there. The re-entrant jet could also be identified from the phase change contours. In the results with the Spalart-Allmaras model (1992), the phase change magnitude inside the cavity was quite small compared to that by other turbulence models, the standard $k-\varepsilon$ (1972) and realizable $k-\varepsilon$ (1995) models. Between the standard and realizable $k-\varepsilon$ models, it was observed that the standard $k-\varepsilon$ model better captured the re-entrant jet than the realizable $k-\varepsilon$ model. Therefore, the standard $k-\varepsilon$ model was selected for the turbulence closure in this study.

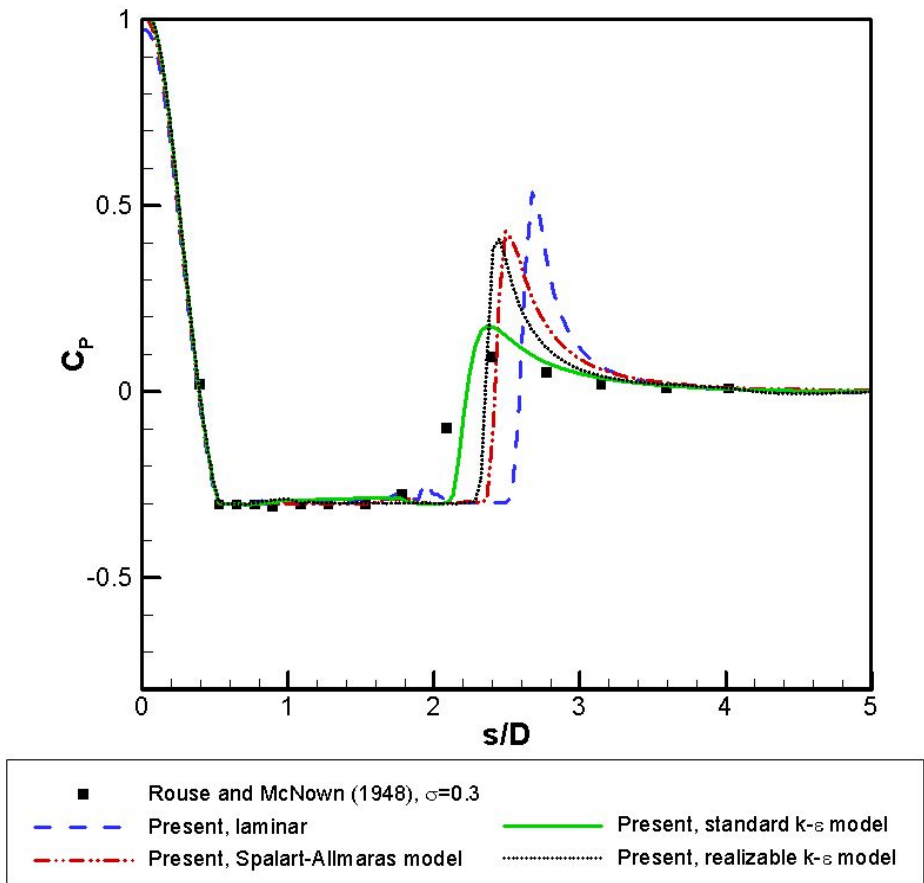
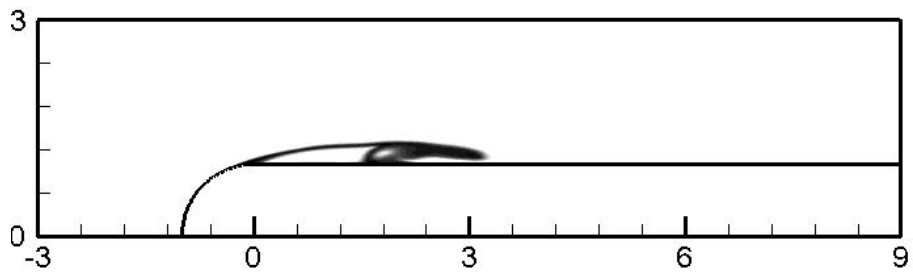
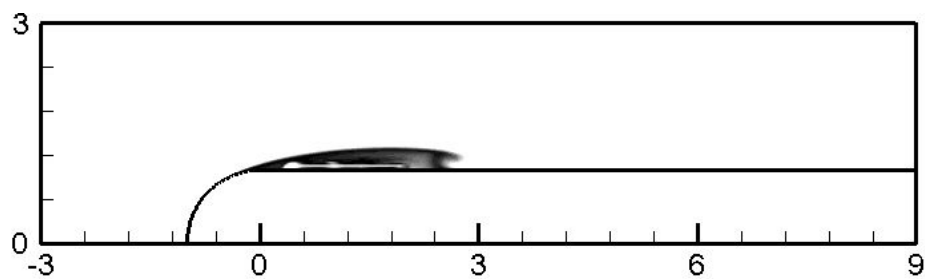


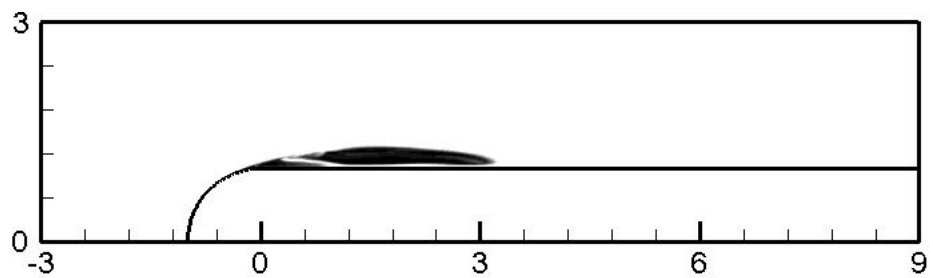
Figure 10. Influence of turbulence model.



(a) Spalart-Allmaras model (1992)



(b) Standard $k-\varepsilon$ (1972)



(c) Realizable $k-\varepsilon$ (1995)

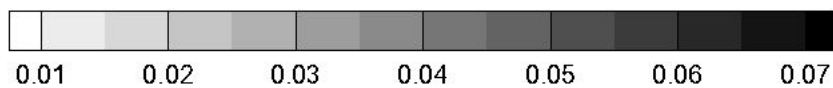


Figure 11. Contours of right-hand side terms in cavitation model (Singhal et al., 2002).

The pressure distribution on the hemispherical head-form body surface for various cavitation numbers was compared to existing experimental data, as shown in Figure 12. A larger pressure overshoot at the cavity closure was observed as the cavitation number decreased. Overall, however, the computed pressure distribution in the non-cavitating and cavitating flows showed quite a close agreement with the existing experimental data.

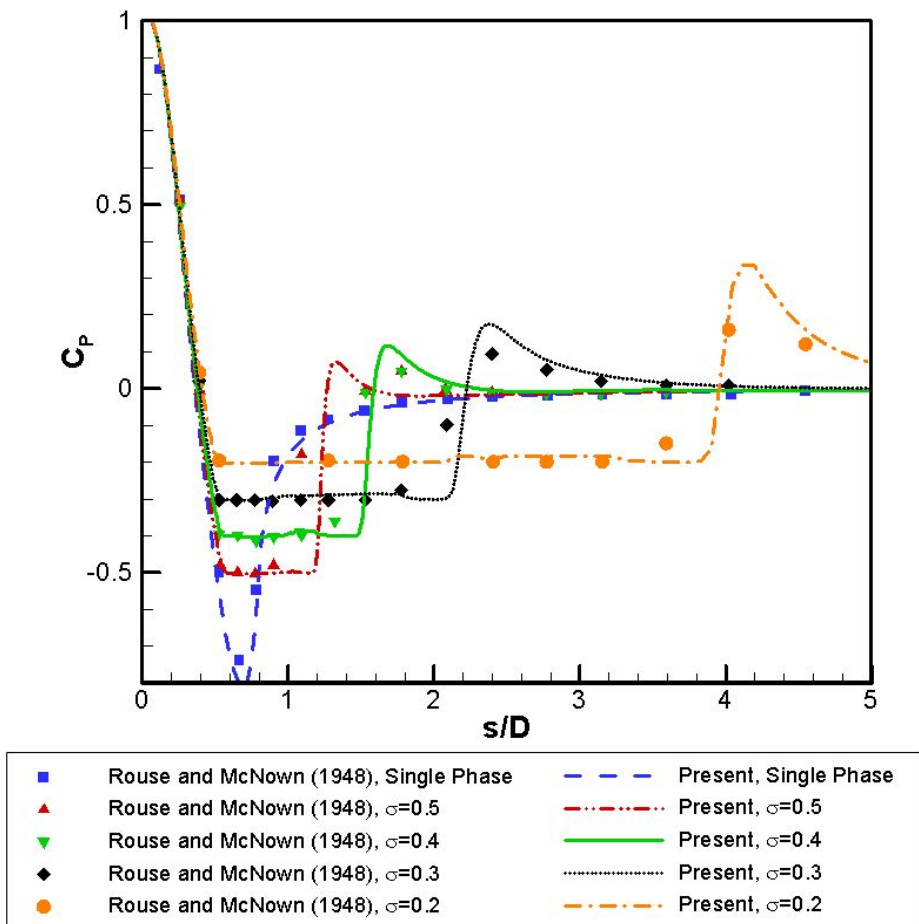
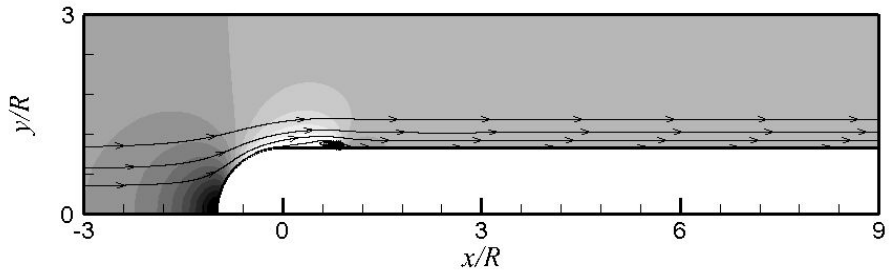


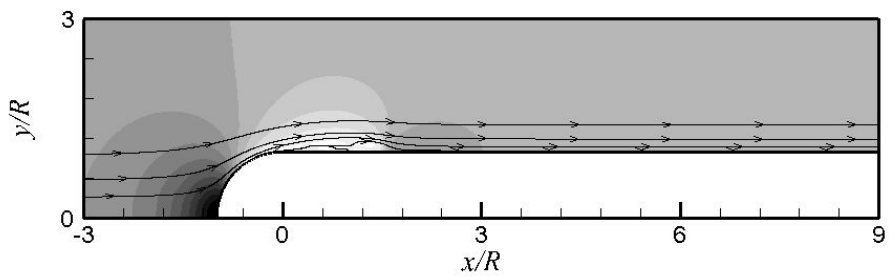
Figure 12. Influence of cavitation number.

The detailed features of the cavitating flow around the hemispherical head-form body are presented in Figure 13 and Figure 14 for various cavitation numbers. Figure 13 shows the pressure coefficient contours and streamlines, while Figure 14 depicts the volume fraction of the liquid phase. A steady partial sheet cavity was observed on the body, and a strong circulation and re-entrant jet was noted near the cavity closure. The pressure level inside the cavity was observed to stay close to the vapor pressure, giving a $-C_p$ value that was approximately equal to σ . Figure 14 also shows the changing partial cavity pattern with the cavitation number. The computed cavity length was noted to increase linearly as the cavitation number was reduced.

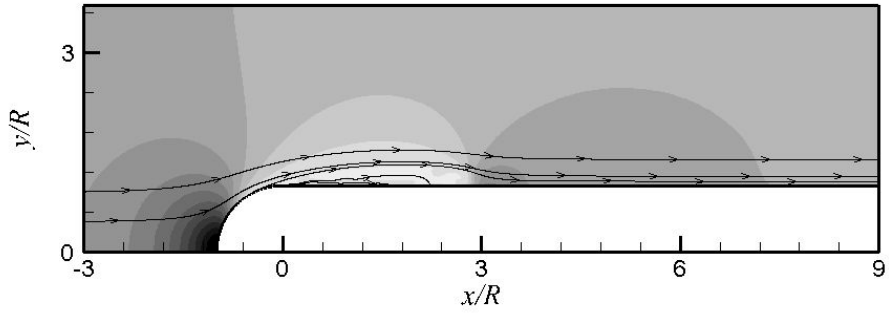
From the computational results for the cavitating flow around the hemispherical head-form body, it was confirmed that the solution domain, mesh, and boundary conditions were appropriately set in SNUFOAM-Cavitation for the given computational conditions with the selected cavitation model of Singhal et al. (2002) and the standard $k-\varepsilon$ turbulence model (1972). The developed code was confirmed to show quite stable behavior for a maximum density ratio, i.e., liquid to vapor, up to 1,000.



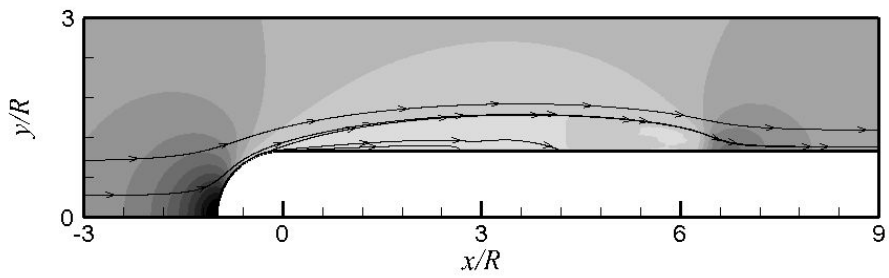
(a) Cavitation number of 0.5



(b) Cavitation number of 0.4



(c) Cavitation number of 0.3



(d) Cavitation number of 0.2

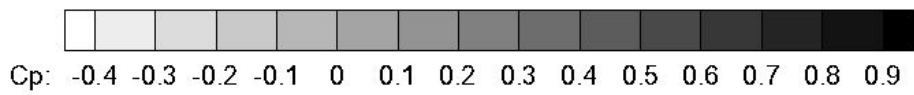
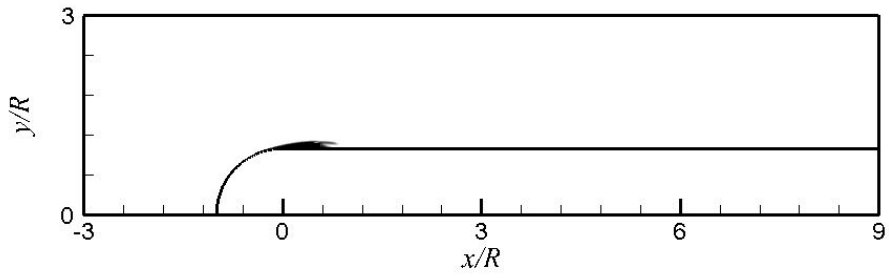
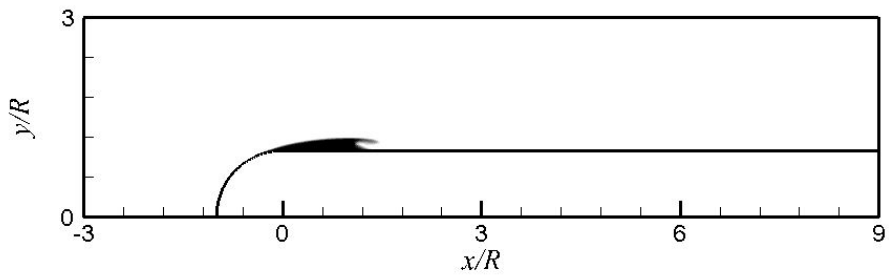


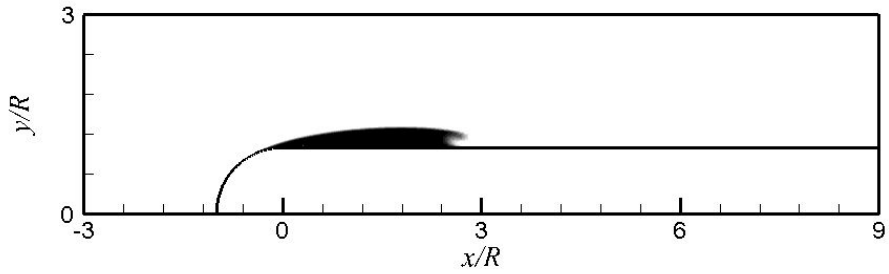
Figure 13. Pressure coefficient contours and streamlines around hemispherical head-form body.



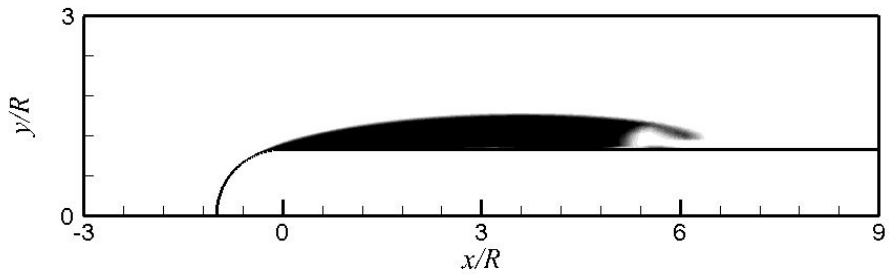
(a) Cavitation number of 0.5



(b) Cavitation number of 0.4



(c) Cavitation number of 0.3



(d) Cavitation number of 0.2

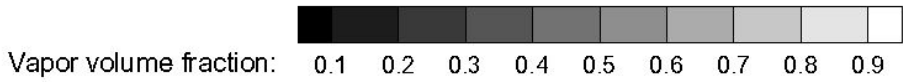


Figure 14. Vapor volume fraction contours around hemispherical head-form body.

Next, the non-cavitating and cavitating flows around the two-dimensional (2D) modified NACA66 hydrofoil, as studied experimentally by Shen and Dimotakis (1985) was considered to select the model constants and validate the developed code. Shen and Dimotakis (1985) measured the pressure on the surface for various angles of attack and cavitation numbers pertaining to natural cavitation. The same verification test was carried out to study the cavitating flow around a marine propeller (Rhee et al., 2005).

On the exit boundary, the reference pressure with the extrapolated velocity and volume fraction was applied. The reference pressure was fixed at the exit boundary with the desired cavitation number. The Dirichlet boundary condition, i.e., the specified value of the velocity, was applied to the inlet boundary. A no-slip condition was applied to the hydrofoil surface. The solution domain extends $-5 \leq x/C \leq 8$ and $-5 \leq y/C \leq 5$ in the streamwise and vertical directions, respectively. Here, C indicates the chord length. An H-type structured grid consisting of 27,000 cells with 170 cells on the surface and 50 cells in the normal direction was used.

The cavity was formed at the leading edge and mid-chord for various angles of attack and cavitation numbers. The test conditions are summarized in Table 3. An angle of attack of 4° indicates the condition of leading edge cavitation, and an angle of attack of 1° indicates the condition of mid-chord cavitation. Unsteady computations were done for a Reynolds number of 10^6 with the standard $k-\varepsilon$ turbulence model.

Table 3. Test conditions of 2D modified NACA66 hydrofoil.

Angle of attack (deg.)	U_∞ (m/s)	P_o (Pa)	P_v (Pa)	Re ($\times 10^6$)	σ	Remark
4	2.01	4114	2420	2	0.84	
4	2.01	4255	2420	2	0.91	Leading edge
4	2.01	4436	2420	2	1.00	cavitation
4	2.01	5969	2420	2	1.76	
1	3.015	3963	2420	3	0.34	
1	3.015	4144	2420	3	0.38	Mid-chord cavitation
1	3.015	4371	2420	3	0.43	

A parametric study was carried out with the angle of attack of 4° and Reynolds number of 10^6 for various evaporation and condensation coefficients. The influence of the evaporation and condensation coefficients was observed in the cavity inception and closure Figure 15. The pressure coefficient and the distribution on the surface at a cavitation number of 0.84 are shown in Figure 16 and Figure 17 for various model constants. The horizontal axis represents the nondimensionalized chordwise length. Figure 16 shows the influence of the evaporation and condensation coefficients upon the closure of the cavity. Cavity closure arrived earlier when increasing the condensation coefficient. The cavity length decreased with an increase in the condensation coefficient due to the stimulated condensation. The condensation coefficient was the dominant factor influencing the closure of the cavity. However, the cavity inception region, $0 \leq x/C \leq 0.05$, is different from the cavity closure region, as shown in Figure 17. The pressure overshoot decreased as the evaporation coefficient increase, i.e., the evaporation coefficient was the dominant factor for cavity inception. Through a comparison with experimental data, the evaporation and condensation coefficients were selected as 0.01 and 0.01, respectively.

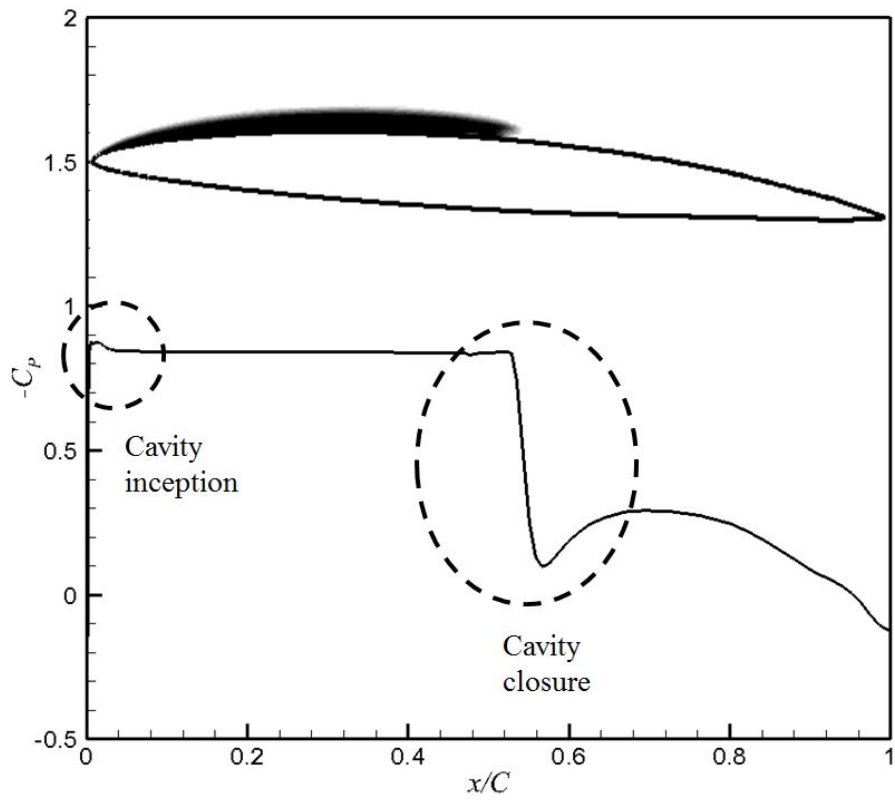


Figure 15. Cavity inception and closure region.

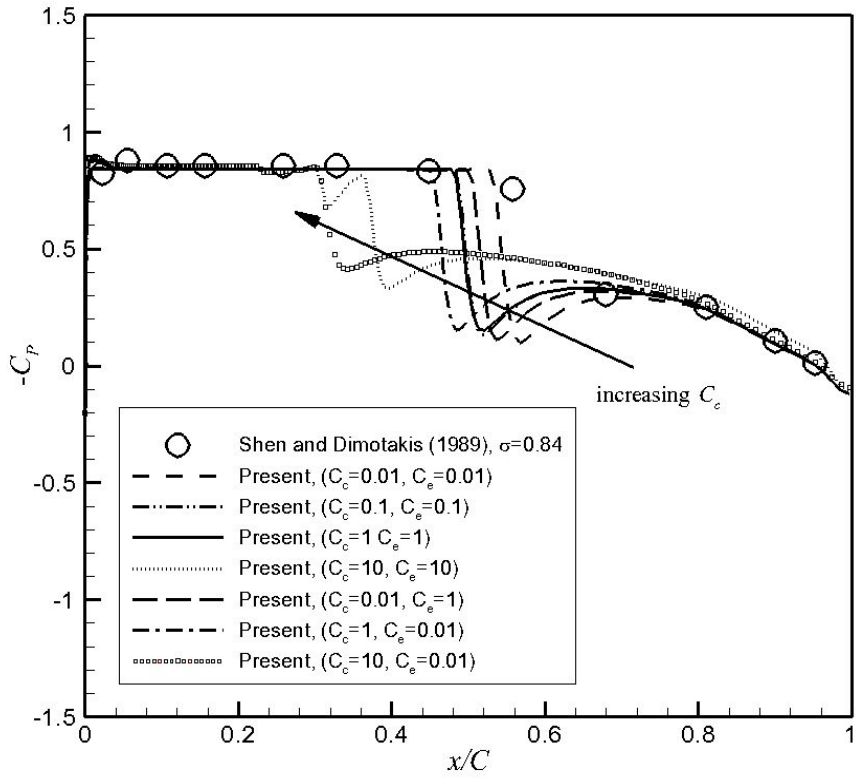


Figure 16. Influence of evaporation and condensation coefficients at cavity closure.

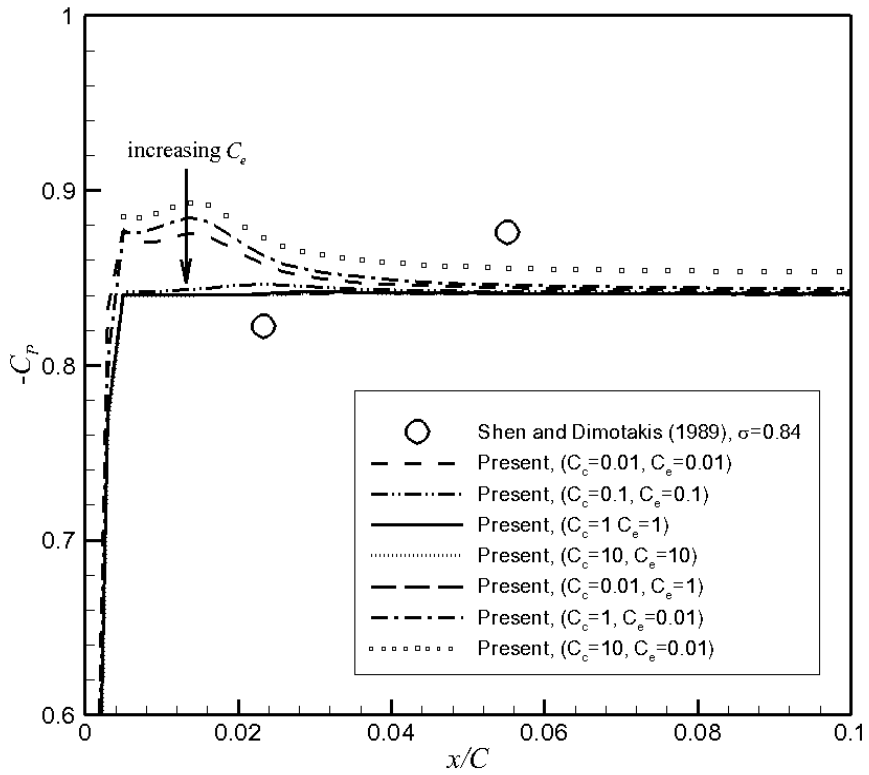
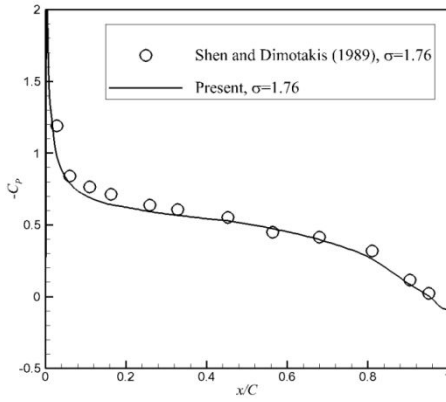


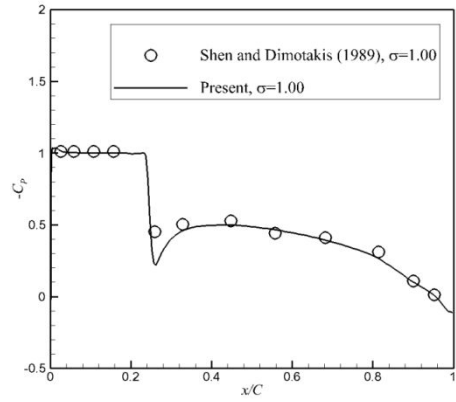
Figure 17. Influence of evaporation and condensation coefficients at cavity inception.

The pressure coefficient distributions on the suction side of the hydrofoil with the leading edge cavitation for various cavitation numbers of 1.76, 1.00, 0.91, and 0.84 are presented in Figure 18. The cavitation number of 1.76 indicated a non-cavitating flow and the cavitation numbers of 1.00, 0.91, and 0.84 indicate cavitating flows. The pressure level inside the cavity was noted to stay close to the vapor pressure. The low cavitation number led to an increasing length of the constant pressure coefficient level, making $-C_p$ nearly identical to the cavitation number. The computed pressure coefficient distributions showed good agreement with the experimental data. Figure 19 displays vapor the volume fraction contours with an angle of attack of 4° and a cavitation number of 0.84, showing the typical leading edge sheet cavitation.

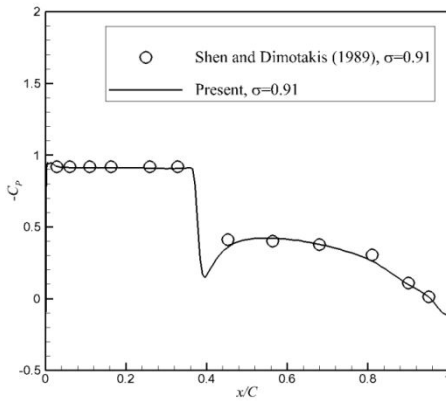
The pressure coefficient distributions on the suction side of the hydrofoil with mid-chord cavitation for various cavitation numbers of 0.43, 0.38 and 0.34 are presented in Figure 20. The cavitation number of 0.43 indicates a non-cavitating flow and the other cavitation numbers indicate cavitating flows. The mid-chord cavitation is slightly prolonged due to the thick boundary layer and the occurrence of possible 2D separation. Figure 21 displays the vapor volume fraction contours with an angle of attack of 1° and a cavitation number of 0.34, showing the reproduced mid-chord cavitation.



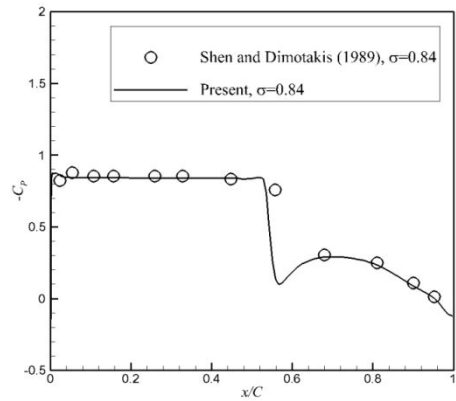
(a) Cavitation number of 1.76



(b) Cavitation number of 1.0

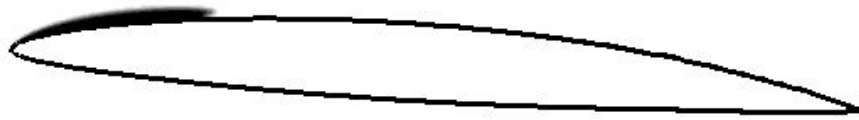


(c) Cavitation number of 0.91

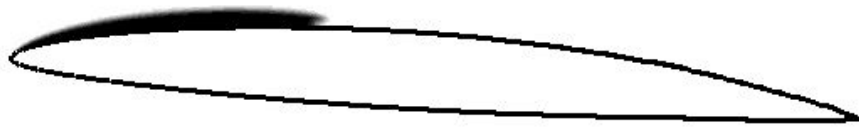


(d) Cavitation number of 0.84

Figure 18. Pressure coefficient distribution on suction side of hydrofoil with leading edge cavitation.



(a) Cavitation number of 1.0



(b) Cavitation number of 0.91



(c) Cavitation number of 0.84

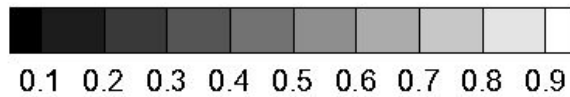
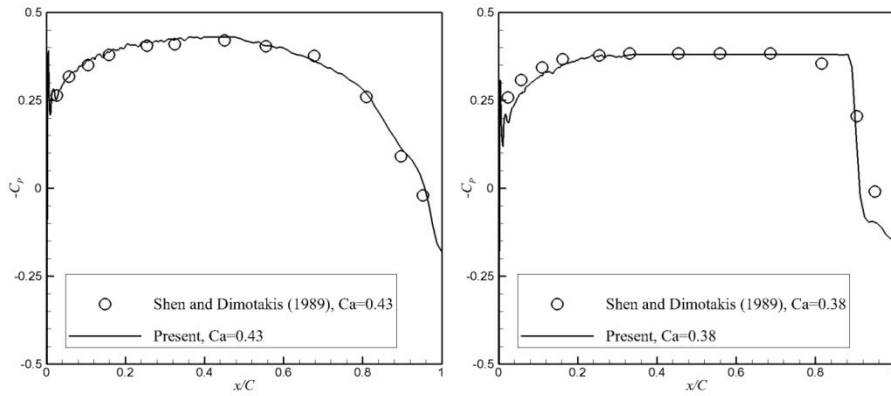
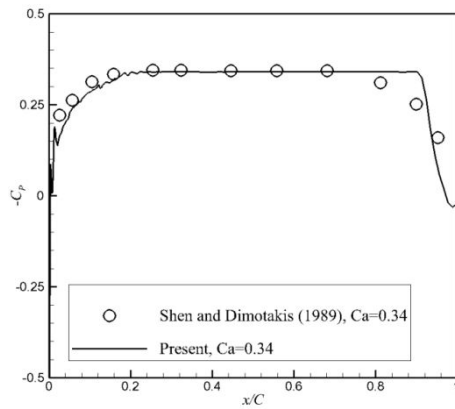


Figure 19. Liquid volume fraction contours with angle of attack of 4 degrees.



(a) Cavitation number of 0.43

(b) Cavitation number of 0.38



(c) Cavitation number of 0.34

Figure 20. Pressure coefficient distributions on suction side of hydrofoil with mid-chord cavitation.

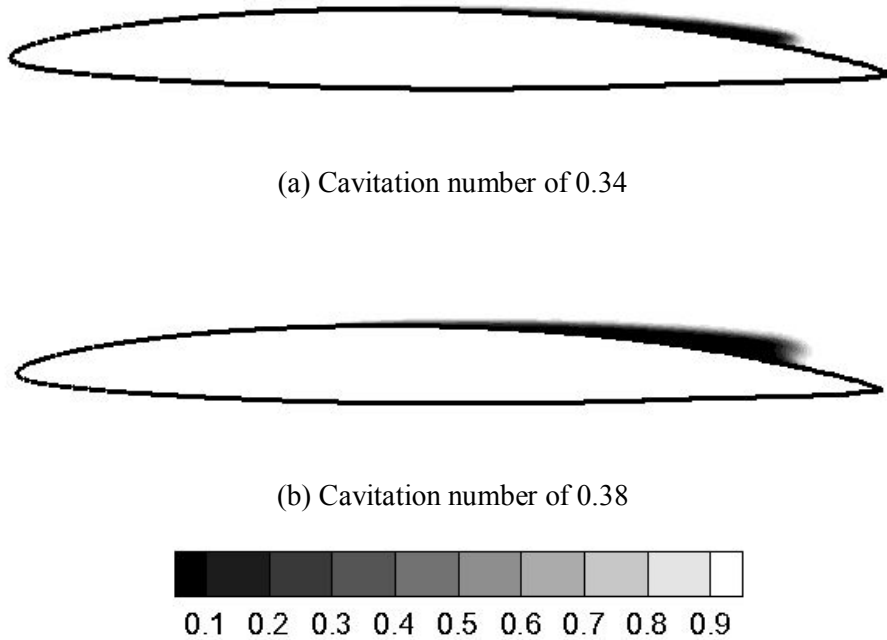


Figure 21. Liquid volume fraction contours with angle of attack of 1 degree.

4.1.2 Super cavitation

Super cavitation indicates that the cavity is enough to encompass an object travelling through the liquid. The cavity length in the flow with cavitation erosion was longer than the characteristic length. Thus, super cavitation was considered.

The 2D wedge geometry for the present study is shown in Figure 22. Two wedge angles, ϕ , of 15° and 45° were considered. The wedge height, $2y_o$,

was determined by the wedge angle, because the wedge length, l_w , was fixed as unity. The Reynolds number (Re), based on the free-stream velocity (U_∞) of 1 m/s and the wedge length of 1 m, was 8.8×10^5 . The cavitation number was in the range of 0.2 to 0.41 based on the free-stream velocity and reference pressure (P_o). The test conditions are summarized in Table 4. Cavitation begins to form in the low-pressure region behind the wedge as in the backward facing step flow and propagates downstream as shown in Figure 22.

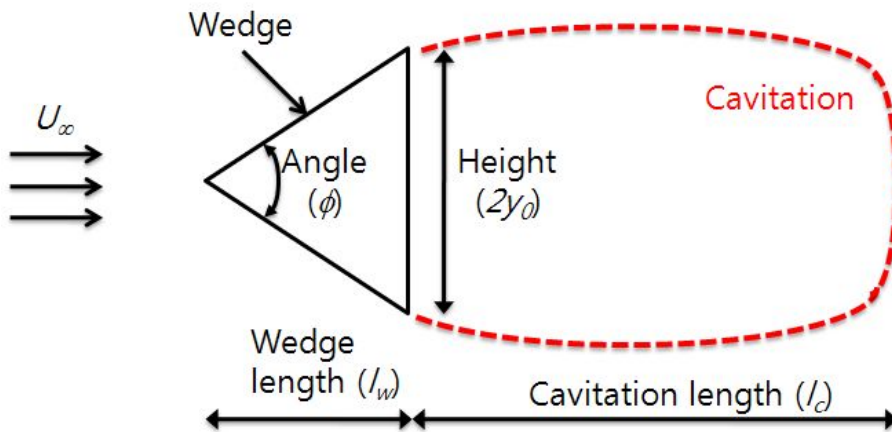


Figure 22. Problem description of wedge-shaped cavitator.

Table 4. Test conditions of wedge-shaped cavitator.

Wedge Angle (<i>degree</i>)	Wedge Height (<i>m</i>)	σ	P_o (<i>Pa</i>)
	0.2632	0.41	2624.63
	0.2632	0.32	2579.71
15	0.2632	0.27	2554.76
	0.2632	0.23	2534.79
	0.2632	0.20	2519.82
45	0.8284	0.35	2594.69

In the Cartesian coordinate system adopted here, the positive x -axis was in the streamwise direction, and the positive y -axis was in the vertical direction. Only half of the wedge-shaped cavitator was modeled due to the y -axis symmetric shape. The solution domain extent shown in Figure 23 was $30 \leq x/l_w \leq 41$ and $0 \leq y/l_w \leq 30 \sim 40$ in the streamwise and vertical directions, respectively. The left and top inlet boundary was specified as the Dirichlet boundary condition, i.e., with a fixed value of the velocity. Note that the top boundary was inclined by 8 degrees for better solution convergence behavior in the case of unbounded flow simulations. Because the main objective of the simulation of the flow around the cavitator was to see how the cavitation develops behind the cavitator, the unbounded flow situation was selected. On

the exit boundary, the reference pressure with the extrapolated velocity and the volume fraction was applied. The reference pressure was taken from the exit boundary. A no-slip condition was applied on the wedge surface, and a symmetric condition was applied on the bottom boundaries.

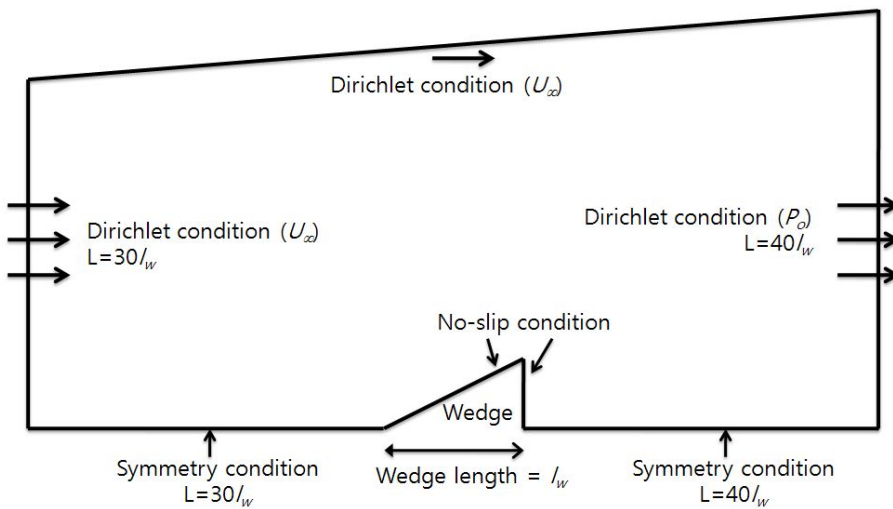


Figure 23. Boundary conditions and domain extent.

A single-block mesh of 26,000 hexahedral cells was used in the computational mesh. On the inclined slope of the wedge, 60 cells were used, while along the back of the wedge, 30 cells were applied (see Figure 24). As for the mesh designed for the standard $k-\varepsilon$ turbulence model in the verification tests, the growth ratio of the cell size was 1.05, and the non-dimensionalized cell height, z/l_w , off the wall was 0.008, which corresponded to $y^+ = 50$.

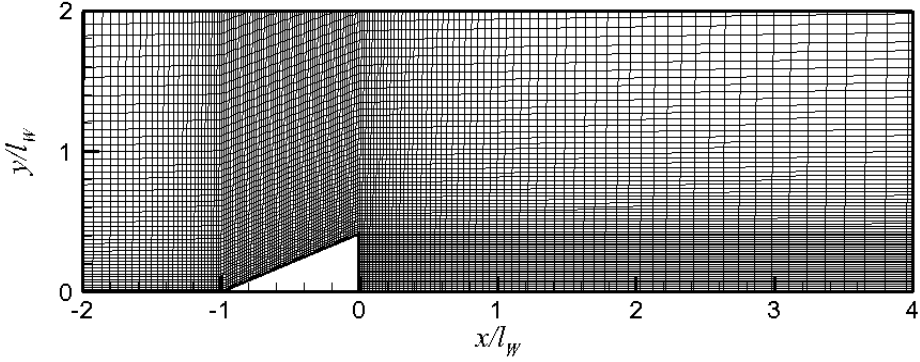


Figure 24. Mesh for wedge-shaped cavitator.

To evaluate the numerical uncertainty in the computational results, the concept of the grid convergence index (GCI) was adopted. Three levels of mesh resolution were considered for the solution convergence of the drag coefficient and the cavity length.

The order of accuracy can be estimated as

$$p = \frac{\ln \left[\frac{(\phi_{medium} - \phi_{coarse})}{(\phi_{fine} - \phi_{medium})} \right]}{\ln(r)} \quad (35)$$

where ϕ_{coarse} , ϕ_{medium} , and ϕ_{fine} are solutions at the coarse, medium, and fine levels, respectively. The Richardson extrapolated value (RE) and the convergence index (CI) were also calculated by Equations (36) and (37), respectively.

$$RE = \phi_{fine} + \frac{(\phi_{fine} - \phi_{medium})}{r^p - 1} \quad (36)$$

$$CI = |\varepsilon| / (r^p - 1) \quad (37)$$

where

$$|\varepsilon| = \left| \frac{\phi_{fine} - \phi_{medium}}{\phi_{fine}} \right| \quad (38)$$

and where r is the effective mesh refinement ratio of

$$\left(\frac{N_{fine}}{N_{medium}} \right)^{1/D} = \left(\frac{N_{medium}}{N_{coarse}} \right)^{1/D} = 1.4, \text{ with the cell count, } N, \text{ and the number of}$$

dimensions, D . Table 5 summarizes the numerical uncertainty assessment

results. Overall, the solutions show good mesh convergence behavior with

errors from the corresponding RE of less than 0.5 %.

Table 5. Numerical uncertainty assessment.

	Coarse	Medium	Fine	p/RE
C_D	0.5585	0.5656	0.5677	1.64/0.5685
ε		0.0125	0.0037	
GCI		0.0052	0.0015	
l_C	9.32	9.42	9.45	1.578/9.4629
ε		0.0106	0.0032	
GCI		0.0045	0.0014	

In order to tame the computational instability caused by the large difference in the density and the high rate of mass transfer, both frequently encountered in an impulsively started flow, the cavitating flow around the wedge-shaped cavitator was computed from the converged single-phase solution under the same condition. Figure 25 and Figure 26 show the contours of the nondimensionalized streamwise velocity component and pressure coefficient for the non-cavitating flow around the 45° angled wedge with the cavitation number of 0.35. The streamwise velocity component increased by 20% at the wedge tip, and a low-pressure region was observed behind the wedge. Note that the location of the maximum streamwise velocity component was slightly different from that of the minimum pressure.

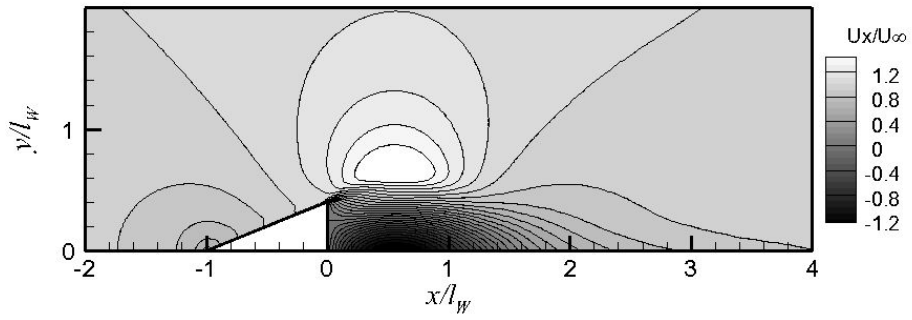


Figure 25. Streamwise velocity component contours without cavitation of wedge angle of 45 degrees.

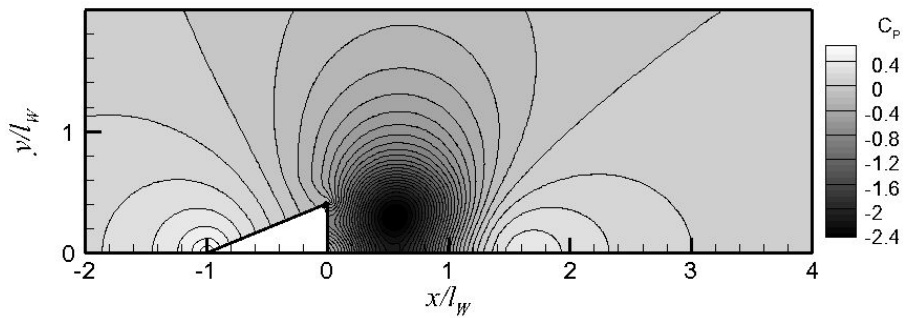


Figure 26. Pressure coefficient contours without cavitation of wedge angle of 45 degrees.

Figure 27 shows the initial shape of the cavity, which takes place at the same location of the low pressure region shown in Figure 26. The fully developed cavity and streamlines are presented in Figure 28. At a cavitation number of 0.35, it was observed that a 45° angled wedge-shaped cavitator could generate a cavity with a length of 9.2 times the wedge length. Note that the fully developed cavity shape was entirely different from that of the low-pressure region shown in Figure 26. Therefore, it can be said that although cavitation inception could be predicted from the non-cavitating flow solution, the fully developed cavity shape cannot be predicted from single-phase flow solutions.

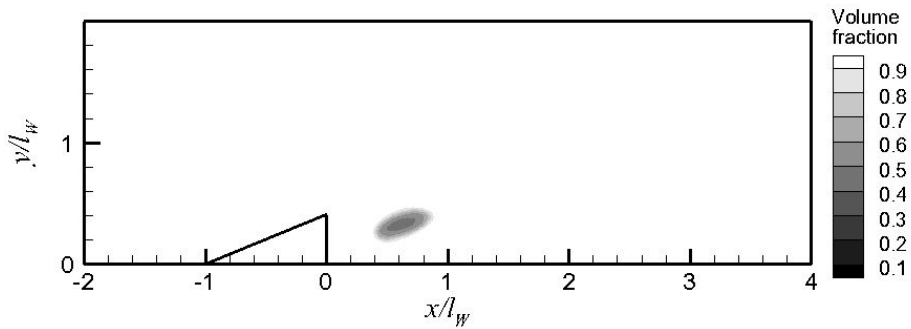


Figure 27. Initial cavity of wedge angle of 45 degrees.

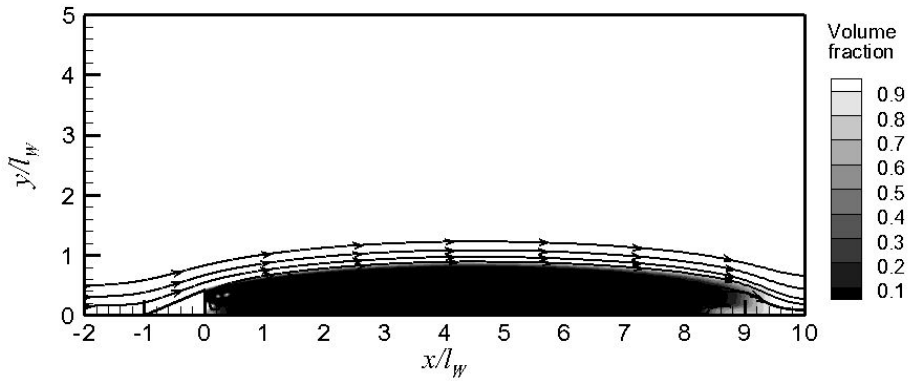


Figure 28. Fully developed cavity of wedge angle of 45 degrees.

Figure 29, Figure 30, and Figure 31 show contours of the nondimensionalized streamwise velocity component, pressure coefficient, and turbulent eddy viscosity of the fully developed cavitating flow around the 45° angled wedge with the cavitation number of 0.35. The turbulent eddy viscosity was nondimensionalized by the kinematic viscosity. The maximum streamwise velocity component was 10% higher than the free-stream velocity but 10% lower than that obtained from the non-cavitating flow. The velocity and pressure fields around the wedge-shaped cavitator were completely changed by the existence of cavitation. The turbulent eddy viscosity was large where the cavity closed, which was caused by the re-entrant jet. Note that there was no difficulty such as artificial cavity closure, which was generally enforced in many potential-flow-based methods.

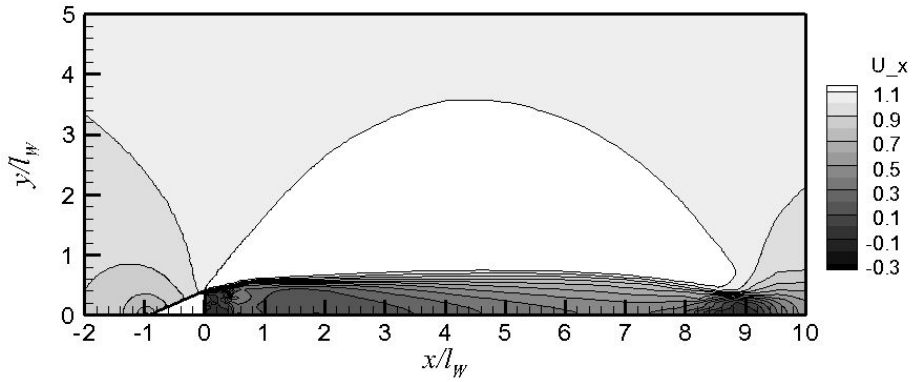


Figure 29. Streamwise velocity component contours in cavitating flow of wedge angle of 45 degrees.

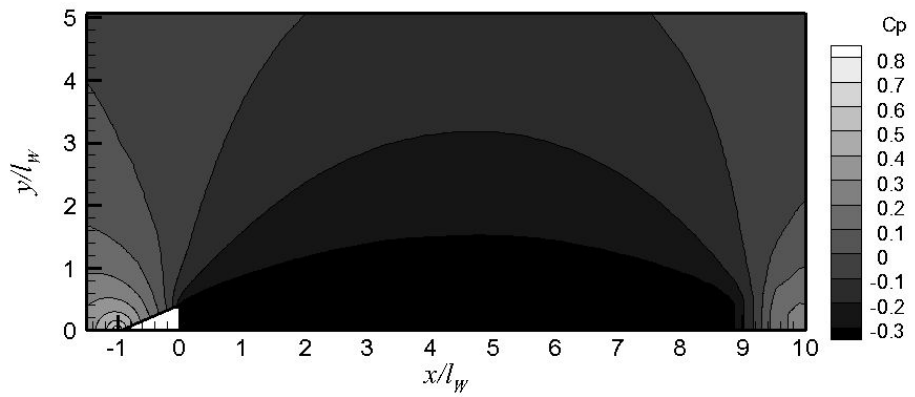


Figure 30. Pressure coefficient contours in cavitating flow of wedge angle of 45 degrees.

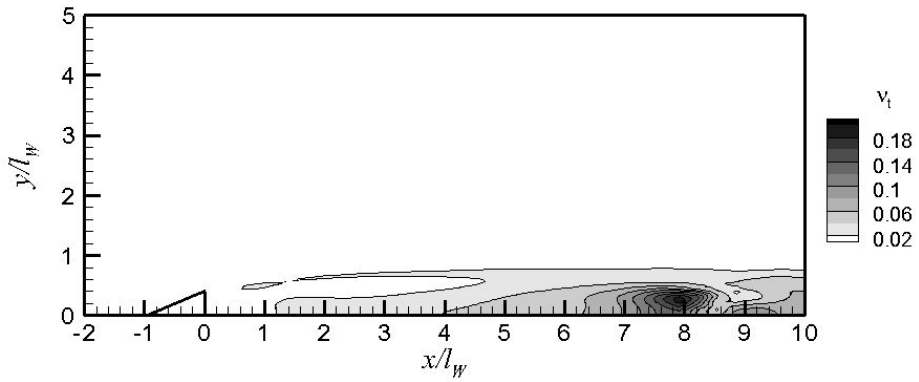


Figure 31. Turbulent eddy viscosity contours in cavitating flow of wedge angle of 45 degrees.

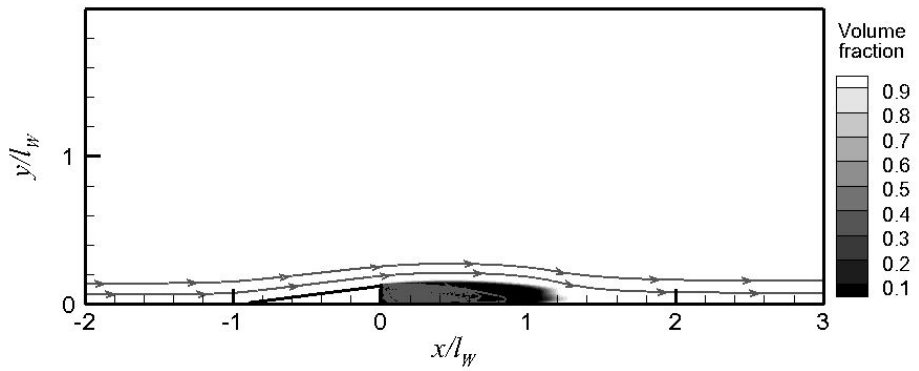


Figure 32. Streamwise velocity component contours in cavitating flow of wedge angle of 15 degrees.

Figure 32 shows the contours of the volume fraction and the streamlines around the 15° wedge with the cavitation number of 0.32. Comparing Figure 28 and Figure 32, although the cavitation numbers are similar, the cavity length of the 45° wedge is much longer than that of the 15° wedge, which suggests that the cavity length is determined by the cavitator geometry as well as the cavitation number.

The computed cavity length was compared with analytic (Newman, 1977) and potential flow solutions (Ahn et al., 2010). Newman (1977) derived the relationship between the cavitation number σ , the cavity length l_c , and the wedge height y_o for 2D symmetric bodies. An example is

$$\frac{\pi}{4} \sigma l_c + \int_0^1 \left(\frac{l_c + 1}{t} \right)^{1/2} y_o'(t) dt = 0 \quad (39)$$

where y_o' is the derivative for an inclined slope.

Ahn et al. (2010) developed a potential flow solver and computed the cavity length of the selected wedge-shaped cavitator. The cavity lengths for various cavitation numbers computed by the present solver, the potential flow solver (2010) and the analytic solutions (1977) are listed together in Table 6 and shown in Figure 33. Cavity lengths were calculated using a vapor volume fraction value of 0.1. The cavity length grew longer as the cavitation number decreased and wedge height increased. The cavity length computed by SNUFOAM-Cavitation was somewhat shorter than that by the potential flow solution, and the cavity length calculated by the analytic solution was

predicted between the potential and viscous flow solutions at high cavitation numbers. This tendency is consistent with the general understanding of the characteristics of each method, i.e., consideration of the viscosity and turbulence. Better agreement is observed for the cavity length with the decreasing cavitation number, indicating that more prominent cavitation leads to easier predictions.

Table 6. Cavity lengths behind wedge-shaped cavitor.

Wedge Angle (degree)	Wedge Height (m)	σ	$\pi\sigma/4\gamma_o$	l_c/l_w		
				Present	Analytic solution	Ahn et al., 2010
	0.2632	0.41	2.46	0.63	0.88	0.97
	0.2632	0.32	1.91	1.21	1.35	1.48
15	0.2632	0.27	1.61	1.65	1.79	1.98
	0.2632	0.23	1.37	2.24	2.40	2.98
	0.2632	0.20	1.19	3.02	3.10	3.50
45	0.8284	0.35	0.66	9.10	9.45	-

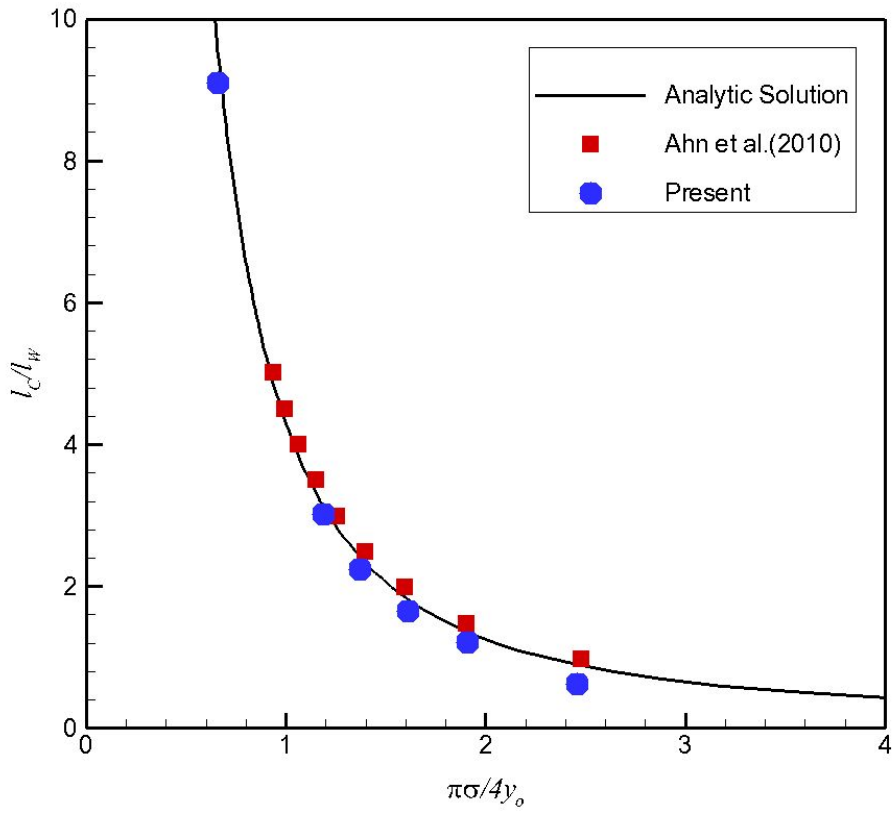


Figure 33. Cavity lengths behind wedge-shaped cavitator.

The dynamic condition on the cavity boundary was derived from the Bernoulli's equation, which could be used to derive the following expression for the total velocity along the cavity interface

$$P_{\infty} + \frac{1}{2} \rho U_{\infty}^2 = P_v + \frac{1}{2} \rho U_v^2$$

$$\frac{P_{\infty} - P_v}{\frac{1}{2} \rho U_{\infty}^2} + \frac{\frac{1}{2} \rho U_{\infty}^2}{\frac{1}{2} \rho U_{\infty}^2} = \frac{\frac{1}{2} \rho U_v^2}{\frac{1}{2} \rho U_{\infty}^2} \quad (40)$$

$$U_v = U_{\infty} \sqrt{1 + \sigma}$$

Table 7. Velocity along cavity interface.

Wedge Angle (degree)	σ	$U_c = U_{\infty} \sqrt{1 + \sigma}$ (m/s)	Present U_c (m/s)	Error (%)
15	0.20	1.095	1.099	0.3
	0.23	1.109	1.152	3.8
	0.27	1.127	1.190	5.6
	0.32	1.149	1.207	5.1
	0.41	1.187	1.243	4.6
45	0.35	1.162	1.219	4.9

The total velocities along the cavity interface are compared in Table 7. For different wedge angles, the total velocity was influenced not by the geometry but by the cavitation number. The present computational solution predicted a result that was quite close to that derived from the Bernoulli's equation, which suggests that the cavity shape and the flow just outside of it are largely inviscid, as many studies have discussed.

With the application of a cavitator to an underwater vehicle in mind, the super-cavitating flow around a body with a wedge-shaped cavitator was simulated. The body with the cavitator geometry and the cavitation tunnel extent are described in Figure 34. A body with a length of 80 mm and a half height of 10 mm, and a cavitator with a wedge angle of 25.6° and a length of 20 mm were designed. The height of the computational domain was set to 60 mm, conforming to the experimental facility (Ahn et al., 2012).

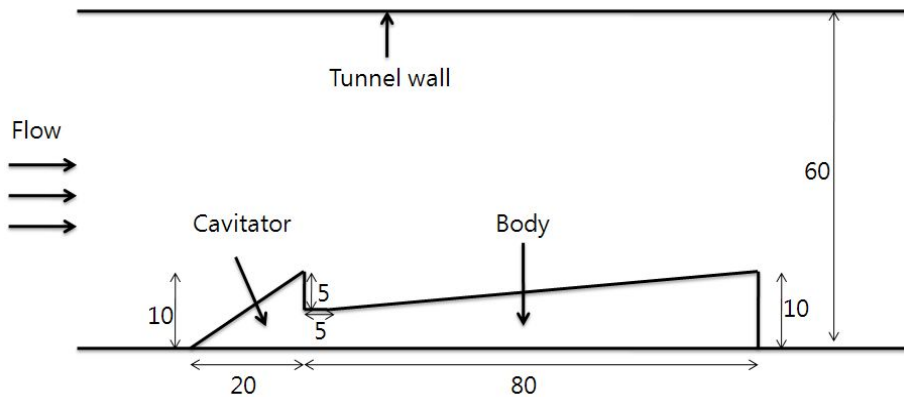


Figure 34. Body with cavitator geometry and cavitation tunnel extent (unit: mm).

The solution domain extent was $-10 \leq x/l_w \leq 20$ and $0 \leq y/l_w \leq 3$ in the streamwise and vertical directions, respectively. With the computation for the wedge-shaped cavitator, it was confirmed that the distance between the inlet and body was more than needed. Thus, the distance was shortened for the case of the body with cavitator. The inlet and exit boundaries were specified as for the computation of the wedge-shaped cavitator. A no-slip condition was applied to the cavitator and body surface, and a symmetric condition was applied to the bottom boundaries. A single-block mesh of 24,000 hexahedral cells was used as shown in Figure 35. On the inclined slope of the wedge, 60 cells were used, while along the back of the wedge, 20 cells were applied.

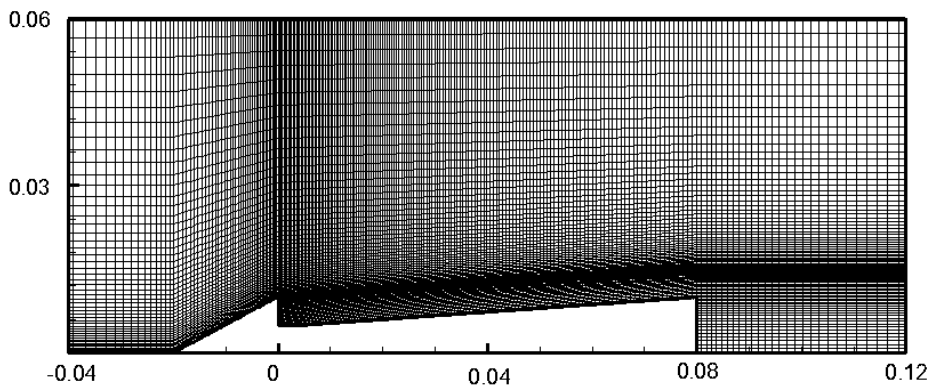
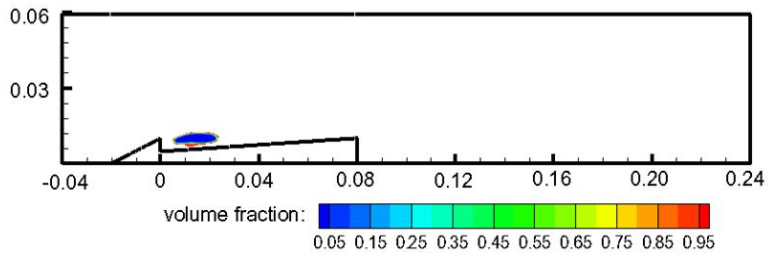
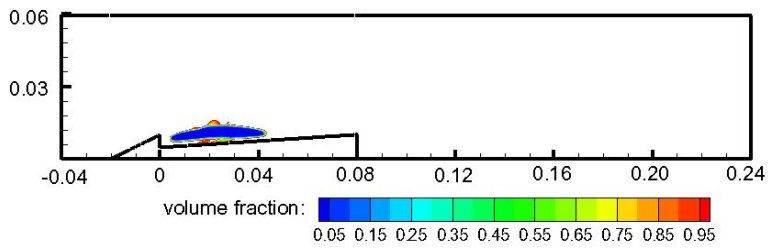


Figure 35. Mesh for body with cavitator.

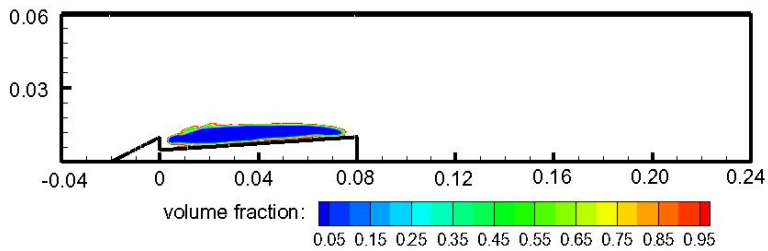
Unsteady computations were done for the cavitation numbers of 1, 1.2, 1.35, and 2.0. The liquid volume fraction contours are shown for cavitation numbers of 1.2, 1.35, and 2.0 in Figure 36. The cavity began on the body and grew as the cavitation number decreased. Once the cavitation number was further lowered to 1.0, another cavity appeared behind the body, as shown in Figure 37 (a), and the two cavities, i.e., one on the body and the other behind the body, started to interact with strong unsteadiness, as shown in Figure 37 (b). Figure 37 (c) shows the time-averaged volume fraction contours around the body. The mean cavity interface is indicated by the dashed line. Noteworthy in Figure 37 (c) is the liquid region immediately behind the body end. Figure 38 shows vapor volume contours and meshes around the liquid region of body with cavitator. More than 3 cells were existed in the horizontal direction. Cells in the horizontal direction were enough to simulate the circulating and translating cavity flows. This appears to be due to the limitation of the cavitation models based on the Eulerian approach and homogeneous mixture flow, as these models cannot handle tiny bubble transport in the re-circulating flow region.



(a) Cavitation number of 2.0

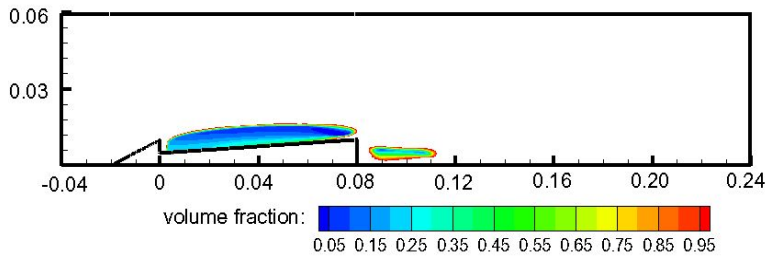


(b) Cavitation number of 1.35

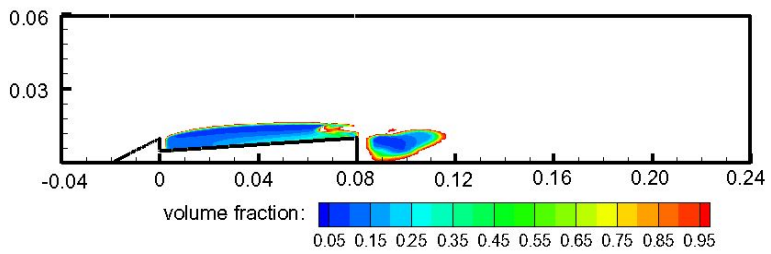


(c) Cavitation number of 1.2

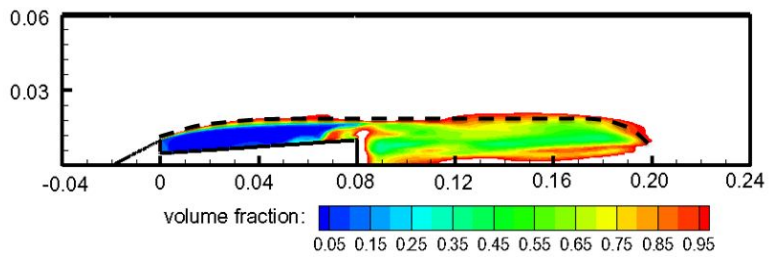
Figure 36. Volume fraction contours of body with cavitator.



(a) Before interaction of cavities



(b) After interaction of cavities



(c) Time averaged contours after cavity fully developed

Figure 37. Volume fraction contours of body with cavitator with cavitation number of 1.

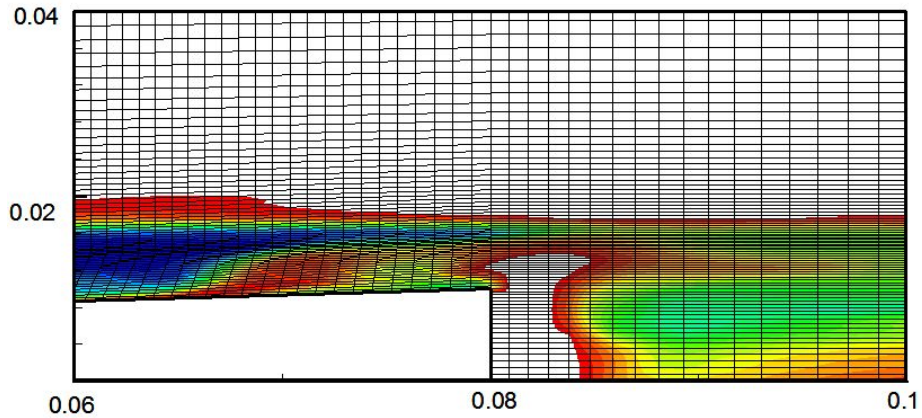


Figure 38. Vapor volume fraction contours and meshes behind body with cavitator with cavitation number of 1.

The findings from the computational results were confirmed by comparisons with the experimental observations in the cavitation tunnel at Chungnam National University (Ahn et al., 2012). Figure 39 is a snapshot of the cavity around the body with the cavitator for the cavitation number of 1.016 and the Reynolds number of 2×10^5 . Figure 40 shows a comparison of the cavity lengths, nondimensionalized by the body length, produced by the present computation and in an experiment (Ahn et al., 2012). Good agreement was observed, and it was confirmed in both the computation and the experiment that super-cavitation started at a cavitation number of 1.0.

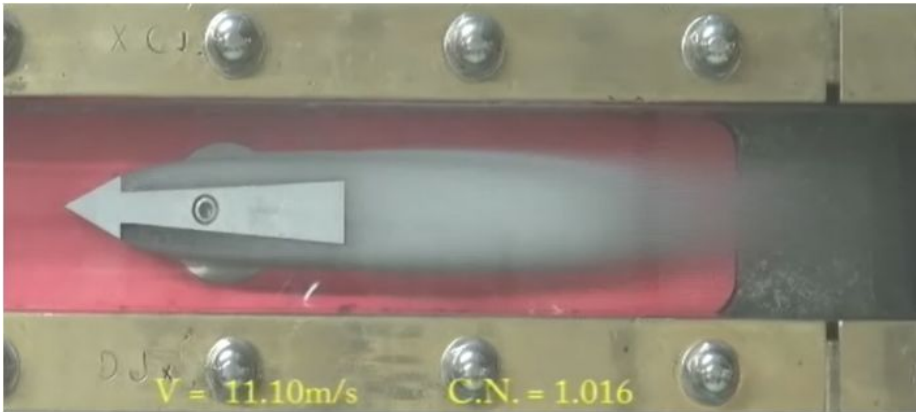


Figure 39. Snap shot of cavity around cavitator with body in experiment.

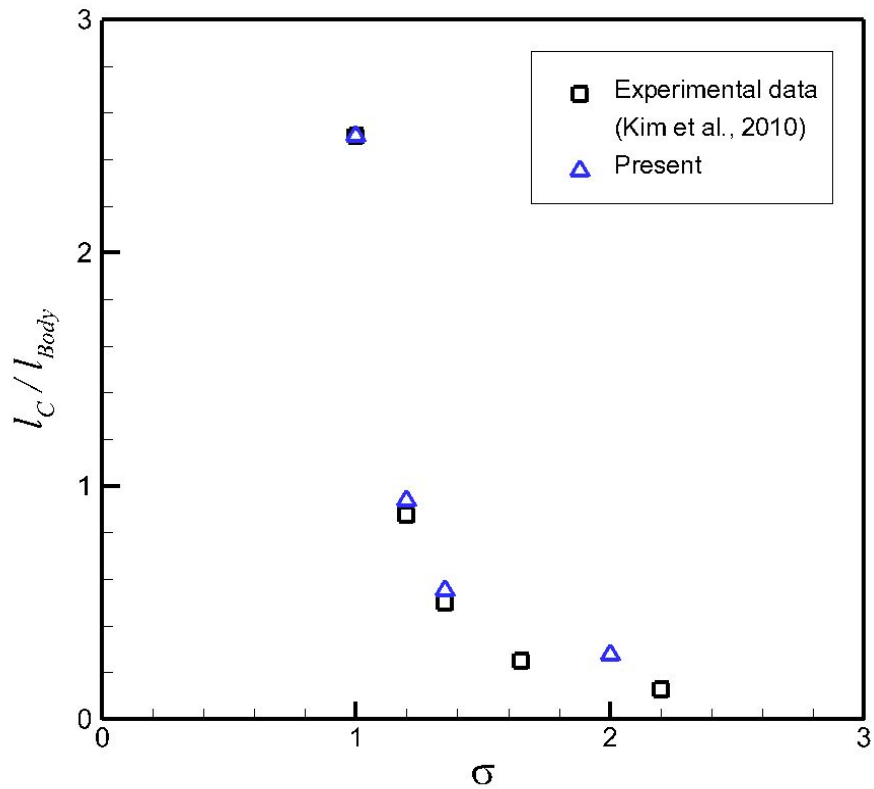


Figure 40. Comparison of cavity lengths for body with cavitator.

4.1.3 Cloud cavitation

Cloud cavitation is the term given to the “cloud-like” structures that are caused by the collapse or condensation of vapor bubbles formed in a liquid in the wake of the body. Cavitation erosions were mainly observed in cloud cavitating flows. Thus, the simulation of a cloud cavitating flow around a three-dimensional (3D) twisted hydrofoil was carried out.

The three-dimensional twisted hydrofoil shown in Figure 41 has a uniform NACA0009 section. It has varying angles of attack in the spanwise direction, as shown in Figure 42. The angle of attack at the each end of the hydrofoil was 0° , while in the middle of the span, it was 11° . The spanwise angle of attack variation of the section is

$$\alpha(y) = \alpha_r \left(2 \left| \frac{y}{0.15} - 1 \right|^3 - 3 \left| \frac{y}{0.15} - 1 \right|^2 + 1 \right) + \beta \quad (41)$$

where α_r is the maximum mid-span angle of attack and β is the angle of attack to the hydrofoil itself. The hydrofoil was designed such that the cavitation began mid-span. The angle of attack was symmetric with respect to the mid-span location. The cavity observation and pressure measurement tests were carried out in the cavitation tunnel of the Delft University of Technology (Foeth et al., 2006; Foeth, 2008; Foeth et al., 2008). The test

section of this tunnel was 0.3 *m* deep and 0.3 *m* wide. The tip vortex at the end of the span was not generated because the span length was same as the tunnel width.

In the right-handed Cartesian coordinate system adopted here, the positive *x*-axis was in the chordwise downstream direction, the positive *y*-axis was in the spanwise direction, and the positive *z*-axis was in the upward direction. The chord length was 0.15 *m* and the span length was 0.3 *m*, which was determined by considering the cavitation tunnel size.

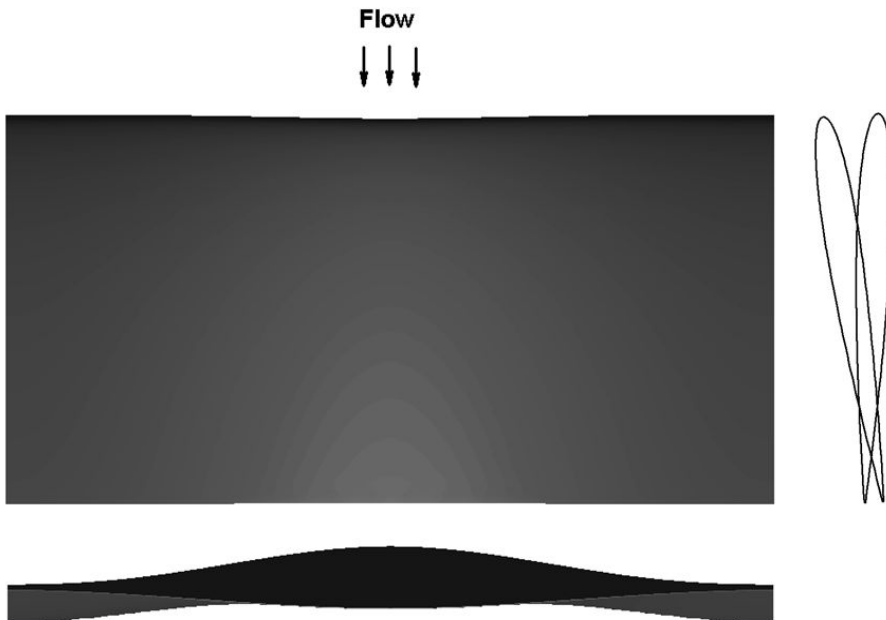


Figure 41. Top, side and front view of 3D twisted hydrofoil.

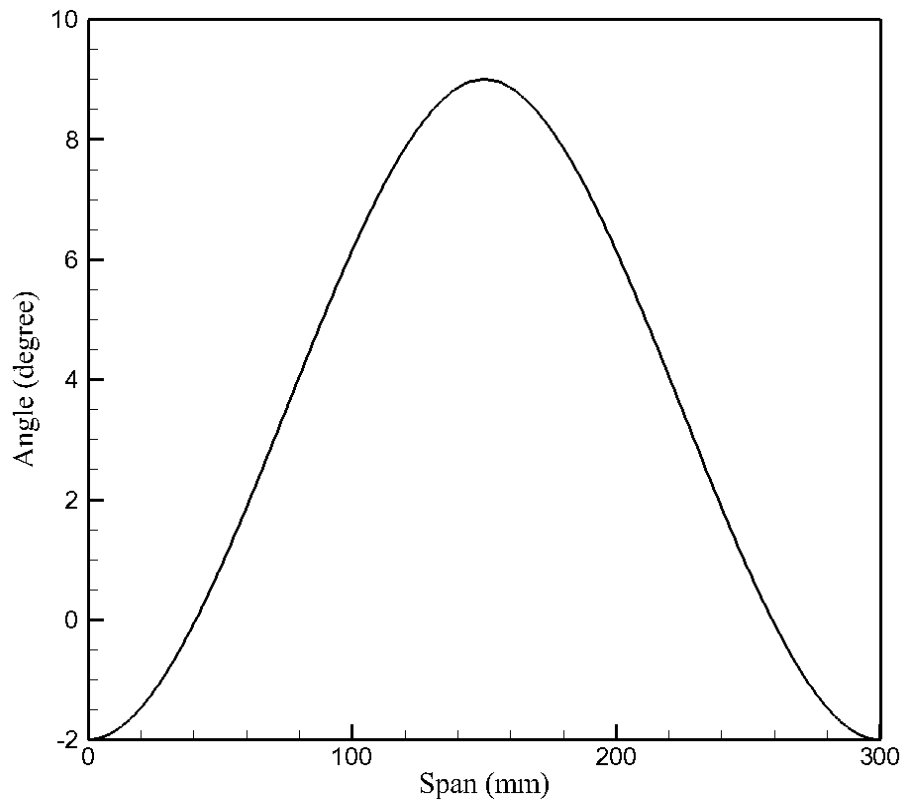


Figure 42. Spanwise distribution of angle of attack.

The test conditions for the non-cavitating and cavitating flows are listed in Table 8. Computations were done with β of -2° which indicated the maximum geometric angle of attack of 9° at mid-span. The Reynolds number (Re), based on a free stream velocity (U_∞) of 6.97 m/s and a chord length of 0.15 m , was 1.04×10^6 , while the cavitation number (σ) was 1.07, based on the free stream velocity and reference pressure (P_o).

Table 8. Test conditions of 3D twisted hydrofoil.

Type	U_∞ (m/s)	P_o (kPa)	P_v (Pa)	Re ($\times 10^5$)	σ
Non-cavitating flow	6.97	97	2970	1.04	-
Cavitating flow	6.97	29	2970	1.04	1.07

The solution domain extent shown in Figure 43 is $-2 \leq x/C \leq 5$, $0 \leq y/C \leq 1$, and $-1 \leq z/C \leq 1$ in the chordwise, spanwise and normal to surface directions, respectively. Only a half span was considered due to the symmetric shape. The left inlet boundary was specified as the Dirichlet boundary condition, i.e., the fixed value of the velocity. On the right exit boundary, the reference pressure with the extrapolated velocity and the volume fraction was applied. The reference pressure was set on the exit boundary. A no-slip condition was applied to the hydrofoil surface, and a free slip condition was applied to the tunnel boundaries. The symmetry condition was applied on the mid-span plane.

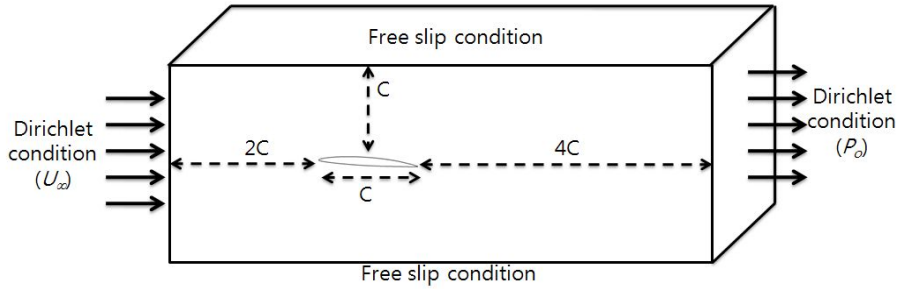
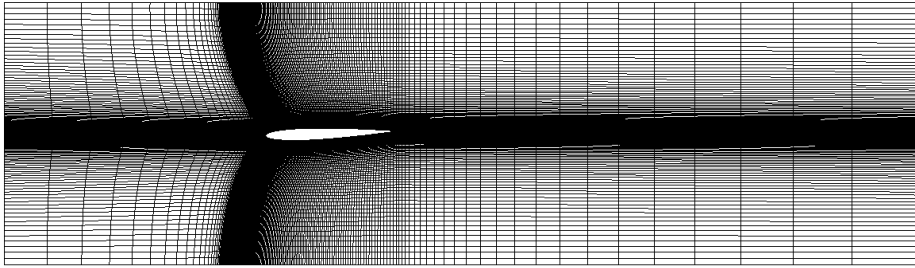


Figure 43. Boundary conditions and domain extent.

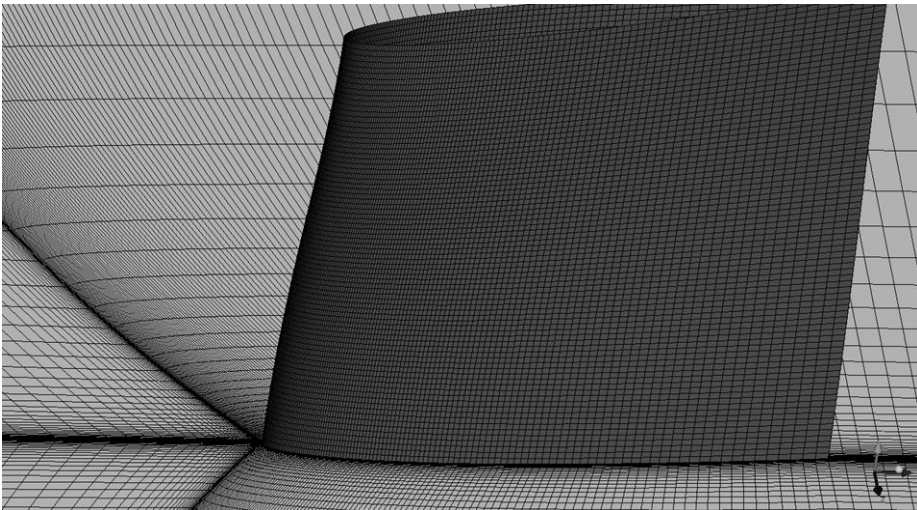
The mesh sensitivity was evaluated with coarse, medium, and fine meshes. The cell counts of the coarse, medium, and fine meshes were respectively $70 \times 50 \times 30$, $99 \times 71 \times 42$, and $140 \times 100 \times 60$ for the chordwise, spanwise and normal directions to the surface, as shown in Table 9. Figure 44 shows a typical mesh of the computational domain.

Table 9. Coarse, medium, and fine meshes for 3D twisted hydrofoil.

	Chordwise (hydrofoil)	Spanwise (hydrofoil)	Normal (hydrofoil)	Total
Coarse	70	50	30	499680
Medium	99	71	42	1413310
Fine	140	100	60	3997448



(a) Mesh on tunnel boundary



(b) Mesh around foil

Figure 44. Mesh for 3D twisted hydrofoil.

Figure 45 shows the pressure coefficient distributions at the mid-span section of the hydrofoil for various mesh counts. The results showed good agreement with the experimental data (Foeth, 2008), implying that the non-cavitating flow was not sensitive to the mesh. Figure 46 shows the pressure coefficient distribution on the pressure and suction sides. The flow direction

is from top to bottom. The maximum and minimum pressure levels were observed around the mid-span area due to the maximum angle of attack. From the pressure distribution of the suction side, it was predicted that the cavity would begin around the mid-span.

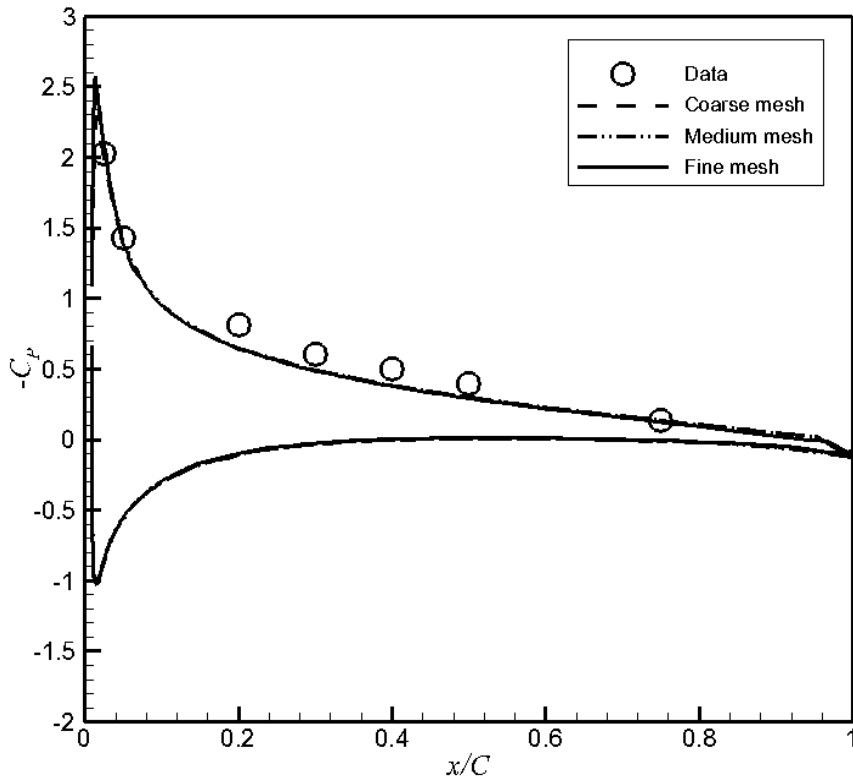
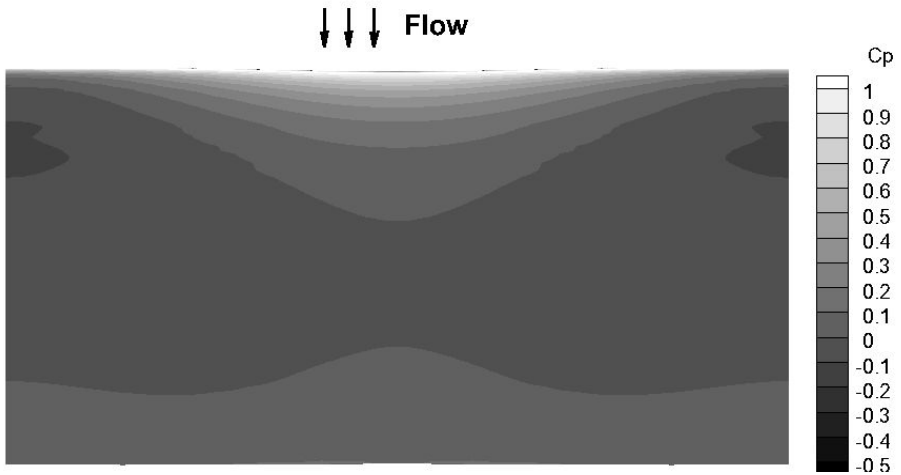
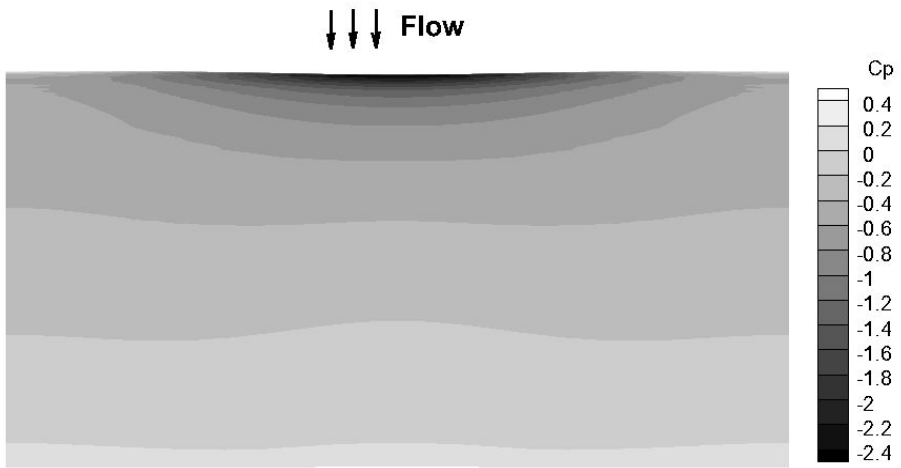


Figure 45. Pressure coefficient distributions at mid-span section of hydrofoil in non-cavitating flow.



(a) Pressure side



(b) Suction side

Figure 46. Pressure coefficient distributions on pressure and suction sides.

To tame the computational instability caused by the large difference in the density and the high rate of mass transfer, the cavitating flow computation was started with the converged single phase solution in the same condition. The computation of each time step was finished when the scaled residuals for all the solution variables had dropped by at least six orders of magnitude.

Figure 47 shows the pressure coefficient distributions at the mid-span section of the hydrofoil with various mesh counts. The computed pressure coefficient distributions plotted the time-averaged result for one cavity shedding cycle. The computed cavity length with the coarse mesh was shorter than that of the experiment, whereas the results with the medium and fine meshes showed good agreement.

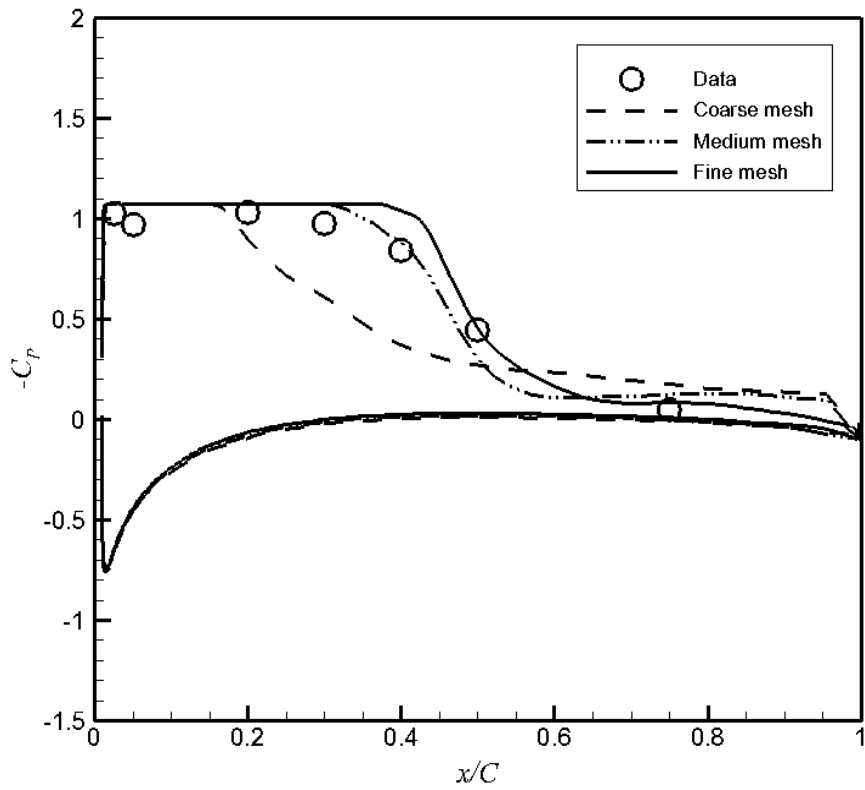
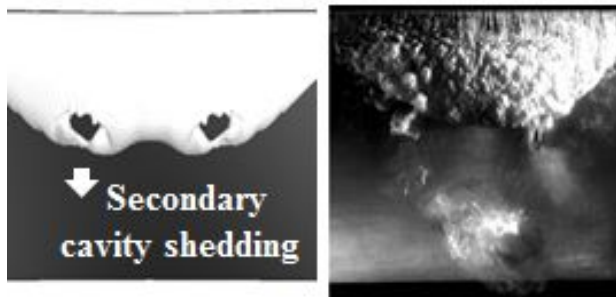


Figure 47. Pressure coefficient distributions at mid-span section of hydrofoil in cavitating flow.

Figure 48 show the cavity shedding cycle as viewed from above. The computed cavity interface was represented by an iso-surface with a vapor volume fraction of 0.1. Note that the typical thickness of the intermediate density region was approximately 0.0003% of the chord length, which corresponds to 5 cells. Also the re-entrant jet was captured in at least four cells on the solid boundary. Figure 48 (a) shows the maximum size of the attached cavity on the surface, where the primary cavity shedding is about to begin. In the experiment, small cavitating vortices were observed at the cavity closure. A re-entrant jet was generated by the positive pressure gradient upon cavity closure and then propagated towards the upstream direction. The difference between the 2D modified NACA66 and the 3D twisted hydrofoils was the side entrant jet due to the varying spanwise loading distribution. The side entrant jet was generated towards the spanwise direction upon the closure of the side cavity, as shown in Figure 49. The vectors on the cavity top interface, where the cavity encountered an external flow, moved towards the downstream direction due to the external flow, as shown in the right side of Figure 49, whereas the vectors on the cavity bottom interface, where the cavity encountered the surface, moved towards the upstream and spanwise directions due to the combination of the re-entrant jet and side entrant jet, as shown on the left side of Figure 49. The velocity magnitude of the re-entrant jet and the side entrant jet was approximately 50% to 90% of the freestream one. Primary cavity shedding started near the leading edge due to the combination of the re-entrant jet and the side entrant jet, which were hitting the cavity interface. The cavity

structure was seen to roll up quickly. The separated cavity was convected downstream and then detached from the hydrofoil, as shown in Figure 48 (b) and Figure 48 (c). The detached cavity was convected downstream and collapsed, as shown in Figure 48 (d) and Figure 48 (e). The remaining attached cavity also grew towards the downstream direction. The computed primary cavity shedding showed a pattern very similar to that of the experimental data. After primary cavity shedding, secondary shedding started at the cavity side, as shown in Figure 48 (a).



(a) Phase 1



(b) Phase 2



(c) Phase 3



(d) Phase 4



(e) Phase 5

Figure 48. Cavity shedding cycle – view from above suction side (left: present, right: data).

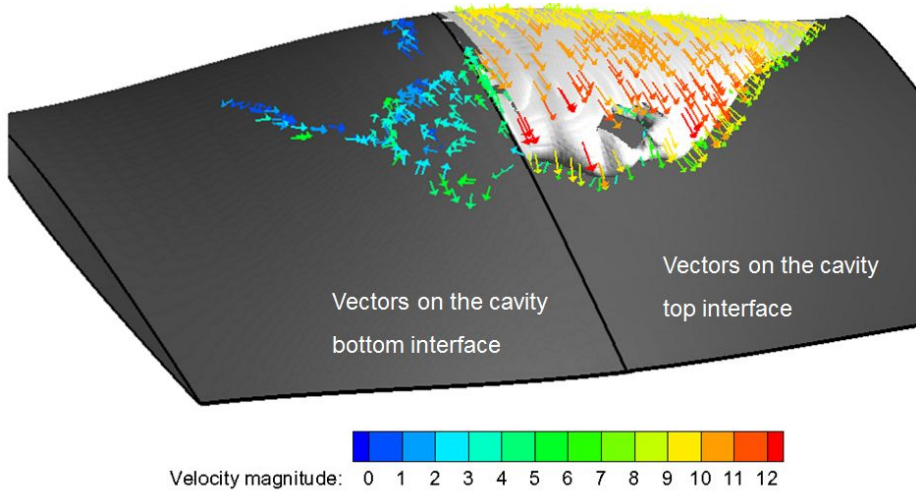


Figure 49. Vectors on cavity interface (left: cavity bottom, right: cavity top).

Figure 50 show the cavity shedding cycle as viewed from the side of the mid-span section. Figure 50 (a) shows the cavity with the maximum length attached to the hydrofoil. The agglomerated cavity around the mid-span plane due to primary cavity shedding was convected downstream, as shown in Figure 50 (b) and Figure 50 (c), and was then detached from the surface, as shown in Figure 50 (d). Figure 50 (e) shows the detached cavity transported downstream. In the cavity shedding cycle, the attached sheet cavity was detached from the surface and transformed to a cloud cavity. The cloud cavity structure was identified as a structure of vortices rather than as a group of bubbles in the experiments.

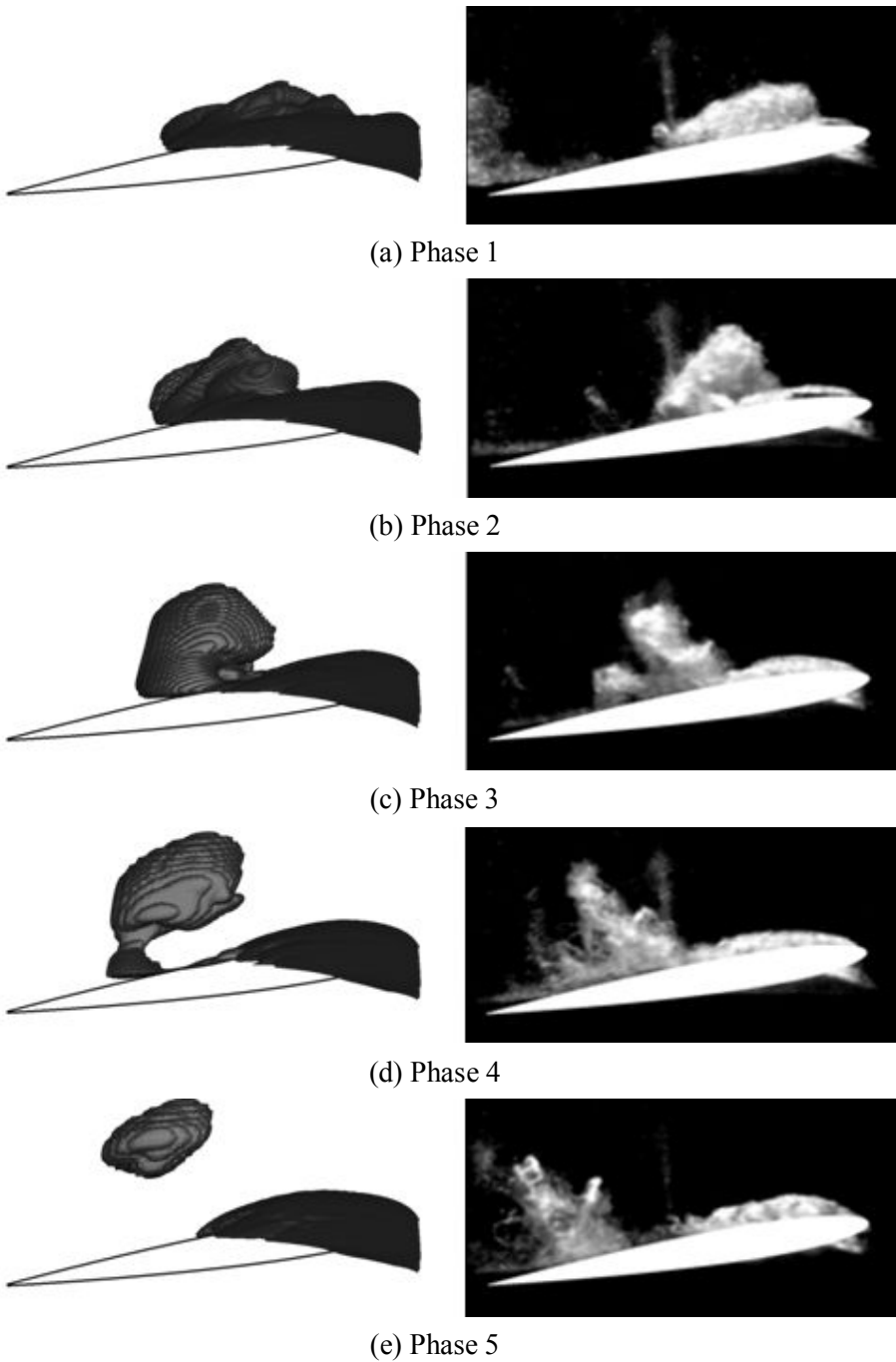
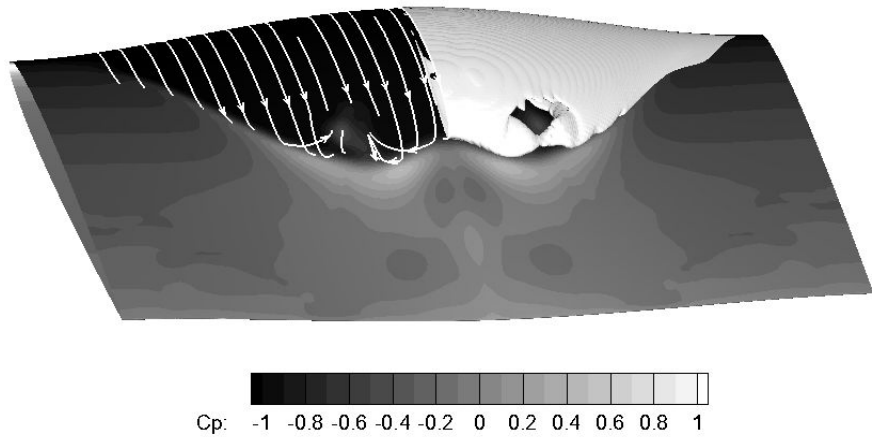
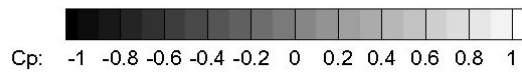


Figure 50. Cavity shedding cycle - view from side of mid-span plane (left: present, right: data).

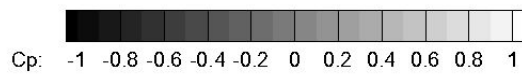
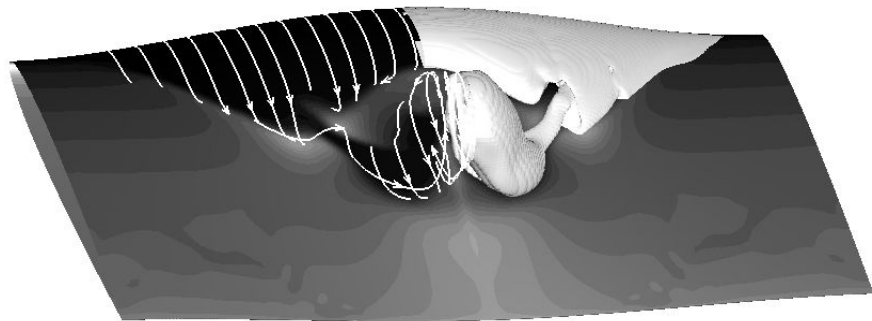
Figure 51 show the pressure coefficient contours on the suction side and the limiting streamlines on the cavity interface for one shedding cycle. Secondary cavity shedding was identified in Figure 48 and Figure 51 (a). The detached cavity was convected downstream and started to roll up, as shown in Figure 51 (b) and Figure 51 (c). The cavity roll up phenomenon was generated by both the upstream re-entrant jet at the cavity bottom interface and the downstream external flow at the cavity top interface, as shown in Figure 52. From the streamline patterns, it was identified that the cloud cavity structure resembled a vortex.



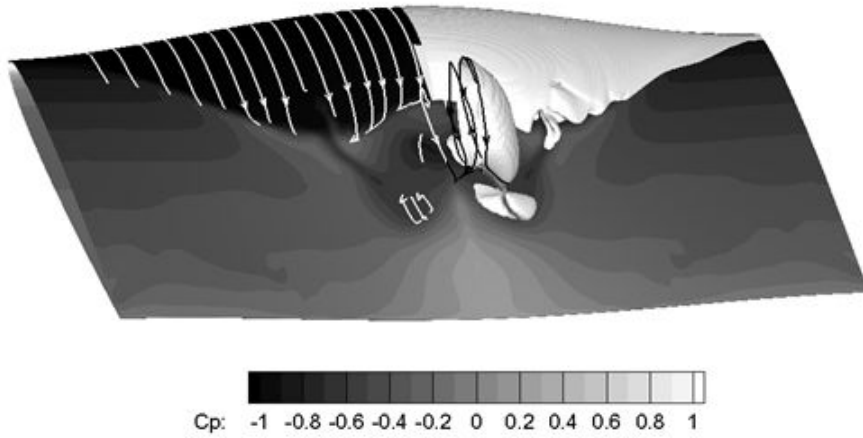
(a) Phase 1



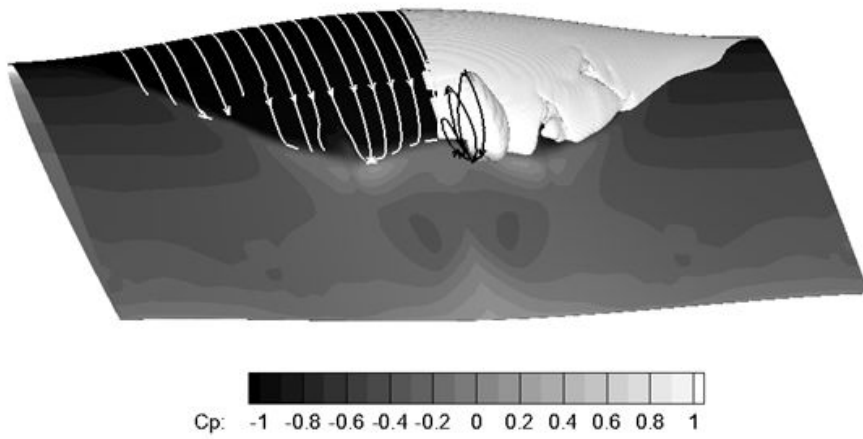
(b) Phase 2



(c) Phase 3



(d) Phase 4



(e) Phase 5

Figure 51. Streamlines on cavity and pressure coefficient distributions on hydrofoil.

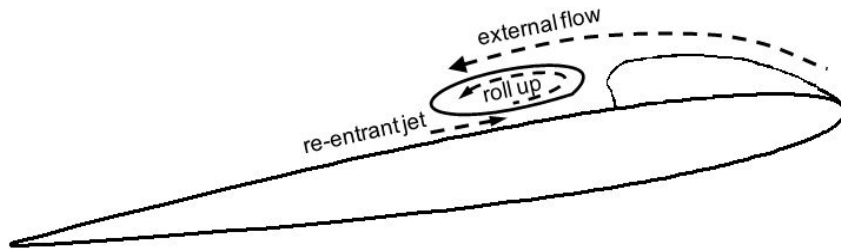


Figure 52. Cavity roll up due to upstream re-entrant jet and external flows.

Figure 53 shows the lift force history of the hydrofoil under a cavitating flow. The lift force coefficient, $C_L = F_z / 0.5 \rho U_\infty^2$, showed periodic variation according to the cavity shedding. The deduced time-averaged lift force coefficient is 0.54, or 4.5% higher than the experimental finding of 0.52. The Strouhal number ($St = f l_c / U_\infty$) based on the shedding frequency, the maximum cavity length l_c , and the free stream velocity was 0.196. The computed St was 4% larger than the measured value of 0.188.

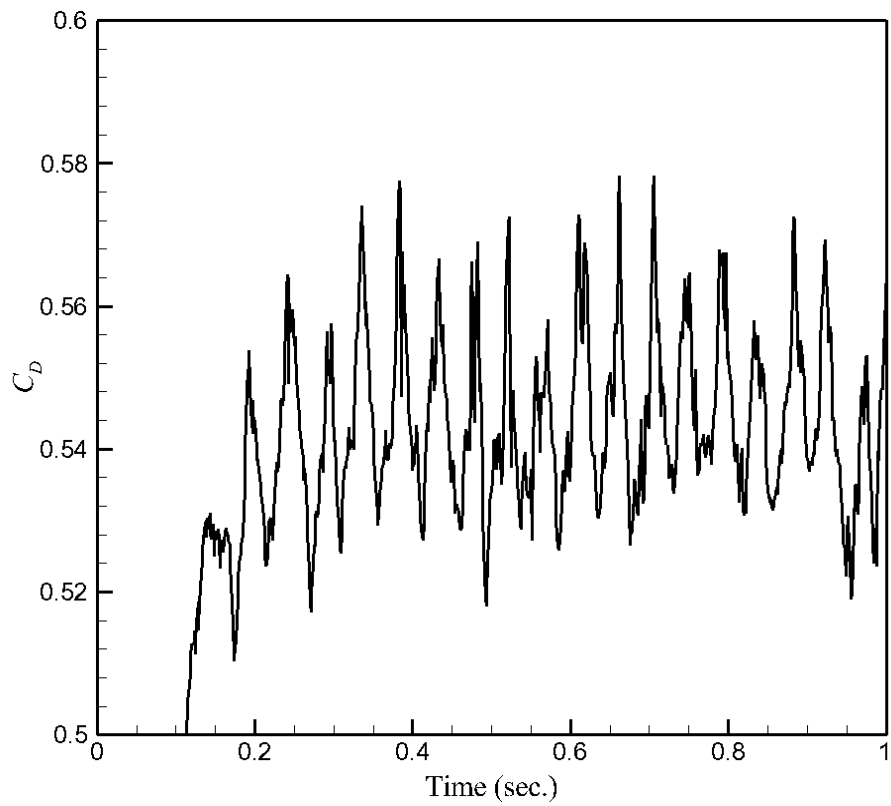


Figure 53. Lift force coefficient history in cavitating flow.

4.2 Isothermal compressible flow

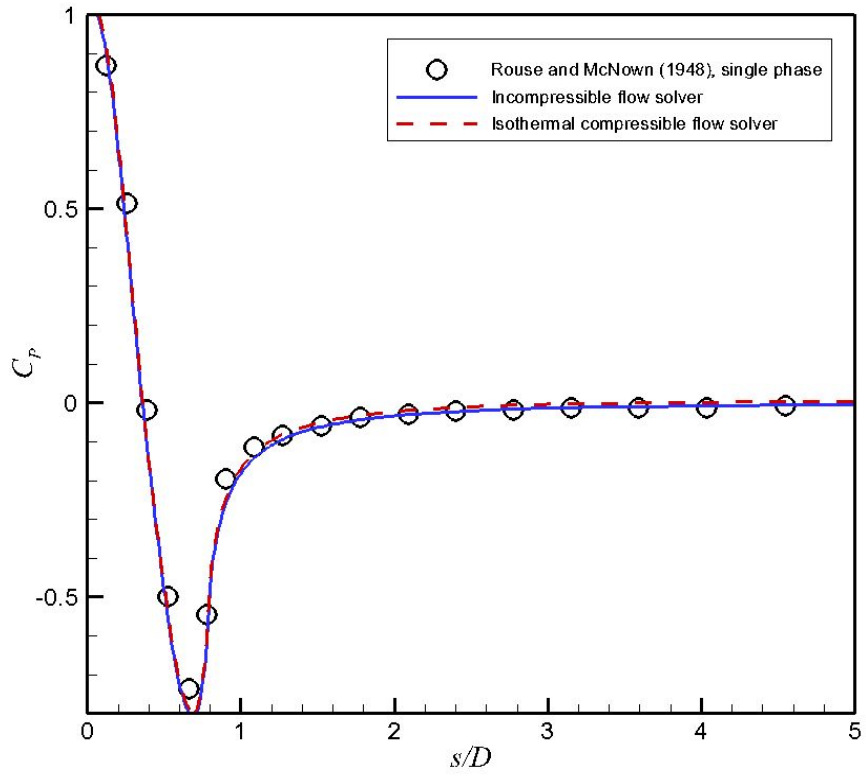
Non-cavitating and cavitating flows around a hemispherical head-form body were simulated by isothermal compressible flow solver, and validated against existing experimental data.

To evaluate the numerical uncertainty in the computational results of the isothermal compressible flow solver, the concept of the grid convergence index (GCI) was adopted. The numerical uncertainty of the incompressible flow solver was evaluated and showed good mesh convergence behavior with errors of less than 0.5 %. Table 10 summarizes the numerical uncertainty assessment results. Overall, the solutions showed good mesh convergence behavior with errors from the corresponding RE of less than 1.0 %.

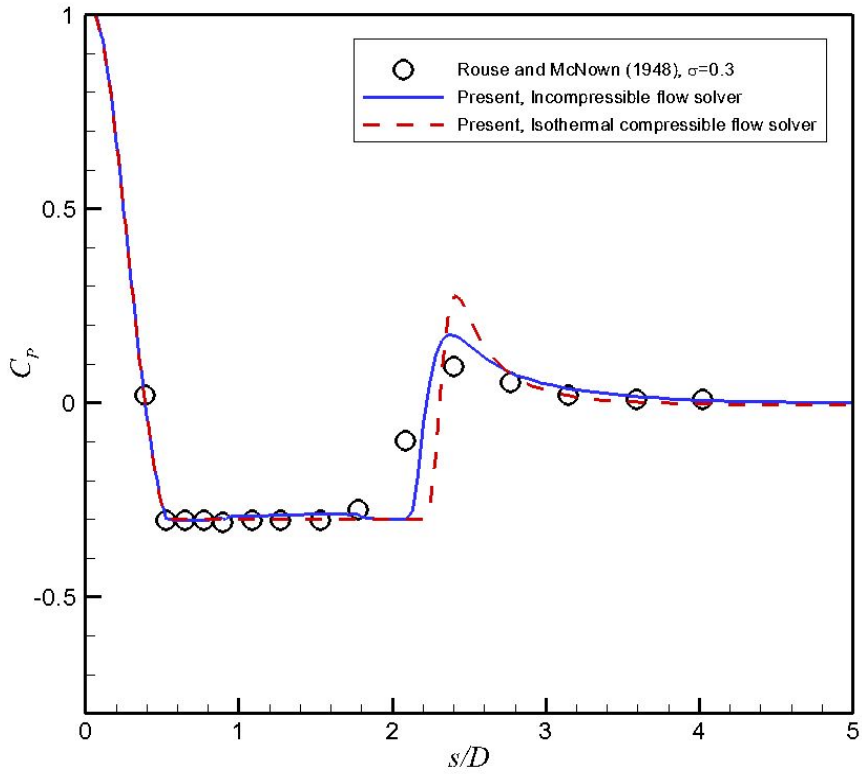
Table 10. Numerical uncertainty assessment of isothermal compressible flow code.

	Coarse	Medium	Fine	p/RE
C_D	0.0886	0.0901	0.0909	1.868/0.0918
ε		0.0166	0.0088	
GCI		0.0190	0.0101	
l_c/R	2.159	2.183	2.196	1.822/2.211
ε		0.0110	0.0059	
GCI		0.0130	0.0070	

The numerical stability in the computational results of the incompressible and isothermal compressible flow solvers was evaluated for various Courant numbers. The incompressible and isothermal compressible flow solvers showed numerically stable results below the Courant number of 10 and 0.5, respectively. Figure 54 shows the pressure coefficient distribution on the hemispherical head-form body surface for the non-cavitating and cavitating flows with the cavitation number of 0.3. In the non-cavitating flow, the isothermal compressible flow solver well predicted the incompressible flow. In the cavitating flow, the computed results of both solvers showed good agreement with the existing experimental data except the cavity closure. The incompressible flow solver showed the earlier cavity closure, while the pressure overshoot at the cavity closure predicted by the isothermal compressible flow solver was more prominent. The compressibility effect was more prominent on the cavity closure than the cavity inception. Note that the compressibility effect was related to a re-entrant jet presented below.



(a) Non-cavitating flow

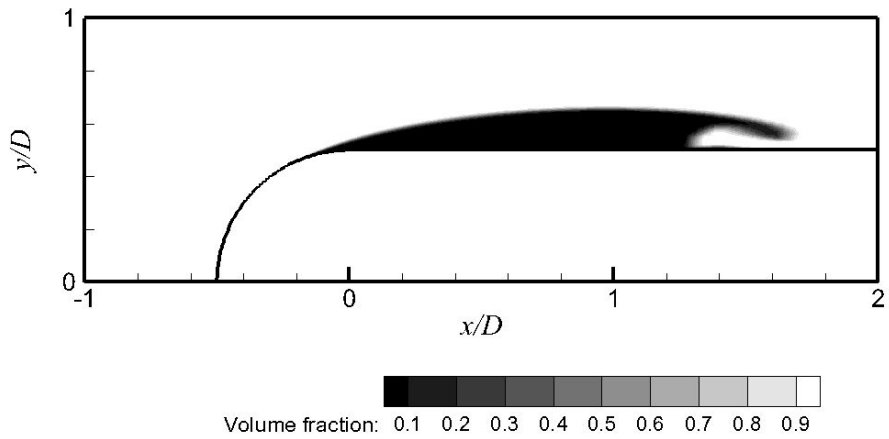


(b) Cavitating flow with cavitation number of 0.3

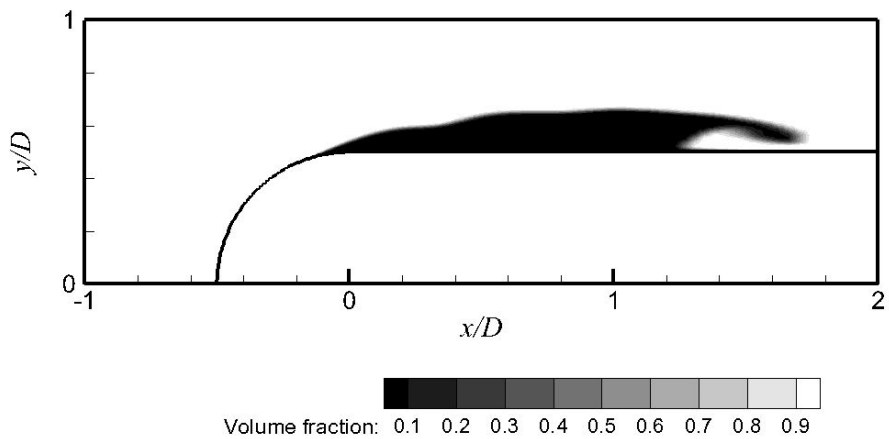
Figure 54. Pressure coefficient distribution influenced by compressibility.

The detailed features of the cavitating flow around the hemispherical head-form body are presented in Figure 55 and Figure 56. Figure 55 shows the volume fraction contours when the cavity was fully developed. Overall cavity behavior was almost similar for both solvers. However, noteworthy in Figure 55 (b) is the undulation of the cavity interface. Unsteady undulation of the cavity interface was not observed in the incompressible flow solver. Variations of the vapor volume fraction due to a re-entrant jet caused the change of the vapor volume, and then the cavity interface showed unsteady undulation. The isothermal compressible flow solver for parabolic type formulation could reproduce the unsteady undulation, while the incompressible flow solver for elliptic type formulation could not. The magnitude of the re-entrant jet was different due to the compressibility effect.

After the cavity was fully developed which is shown in Figure 55, a re-entrant jet was generated at cavity closure and convected to upstream. Figure 56 shows the volume fraction contours when the re-entrant jet was developed to its greatest length. In the incompressible flow solution, the cavity shedding was seen near the cavity closure due to a short re-entrant jet. On the other hand in the isothermal compressible flow solution, the cavity shedding was observed up to the middle of the cavity due to a relatively longer re-entrant jet. The cavity was detached as shown in Figure 56 (b) and then the remaining upstream cavity was grown to downstream again as shown in Figure 55 (b). Unsteady undulation of the cavity interface was observed continuously.

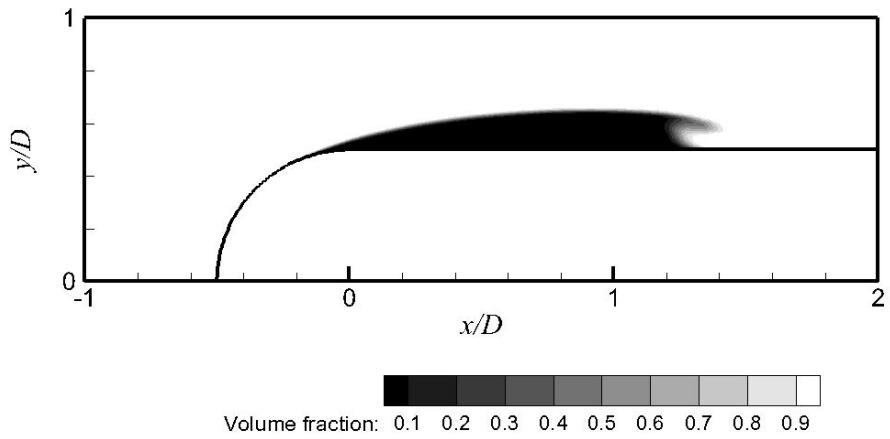


(a) Incompressible flow solver

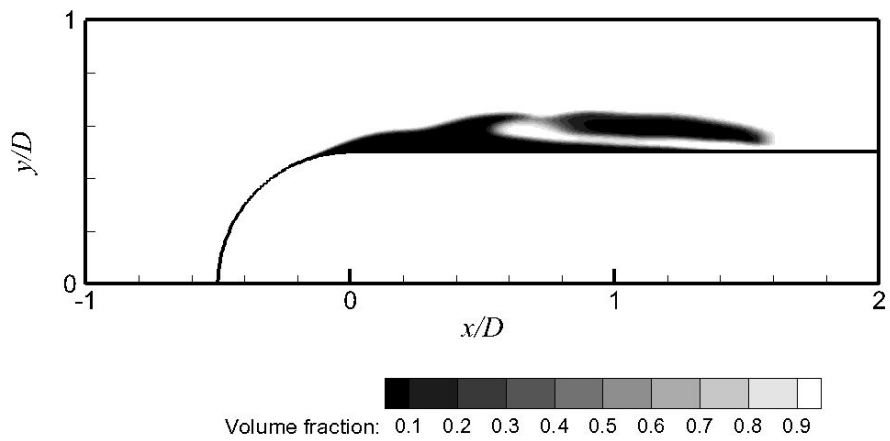


(b) Isothermal compressible flow solver

Figure 55. Volume fraction contours after cavity fully developed.



(a) Incompressible flow solver

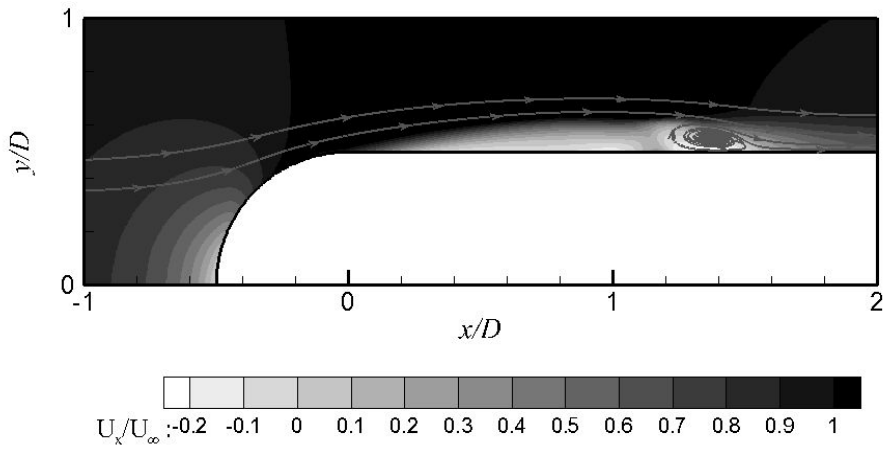


(b) Isothermal compressible flow solver

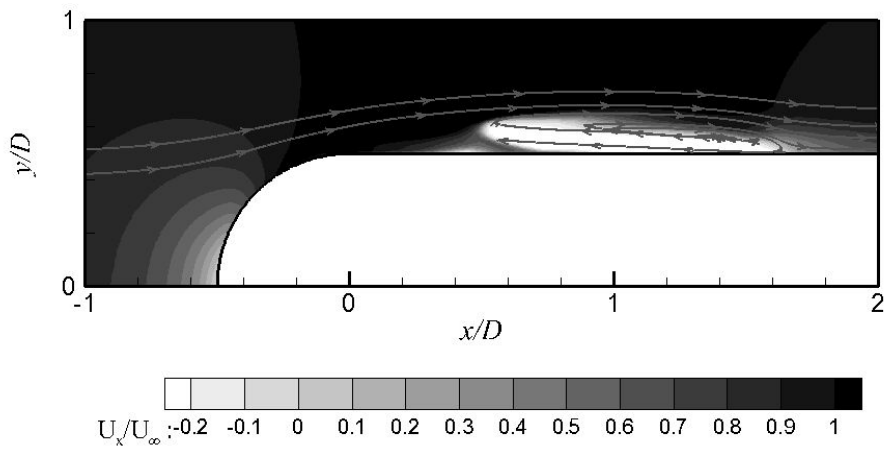
Figure 56. Volume fraction contours with the greatest length of re-entrant jet.

Figure 57 shows non-dimensionalized streamwise velocity contours when the re-entrant jet was fully developed. The relatively strong and long re-entrant jet, which was in the reverse direction to the freestream flow, was observed in the isothermal compressible flow solution. The velocity magnitude of the re-entrant jet and the side entrant jet was approximately 20% of the freestream one. Figure 58 shows the nondimensionalized turbulent eddy viscosity contours when the re-entrant jet was fully developed. In both cases, the turbulent viscosity was large at the cavity closer. The turbulent viscosity in the isothermal compressible flow solution was larger than that in the incompressible flow solution because of the stronger re-entrant jet.

Figure 59 shows the time history of the drag coefficient on the surface of $0 \leq x/D \leq 2$. The drag coefficient of the incompressible flow solution was converged to a certain constant value, while that of the isothermal compressible flow solution showed fluctuation behavior due to the unsteady cavity shedding.

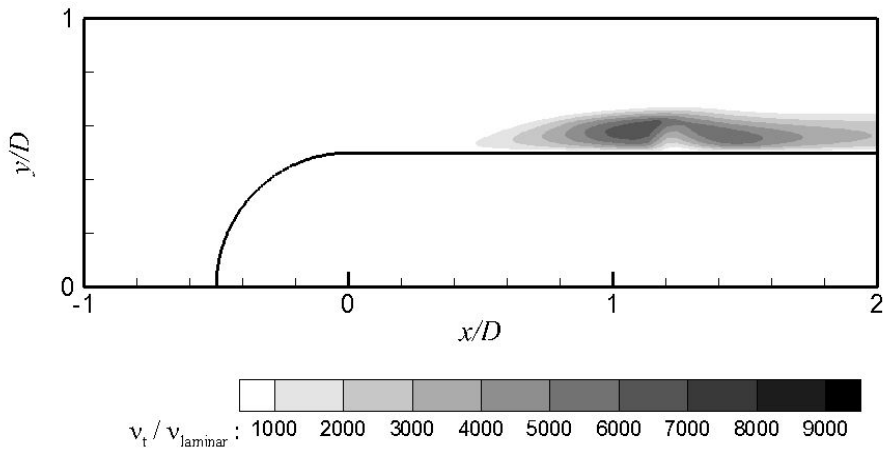


(a) Incompressible flow solver

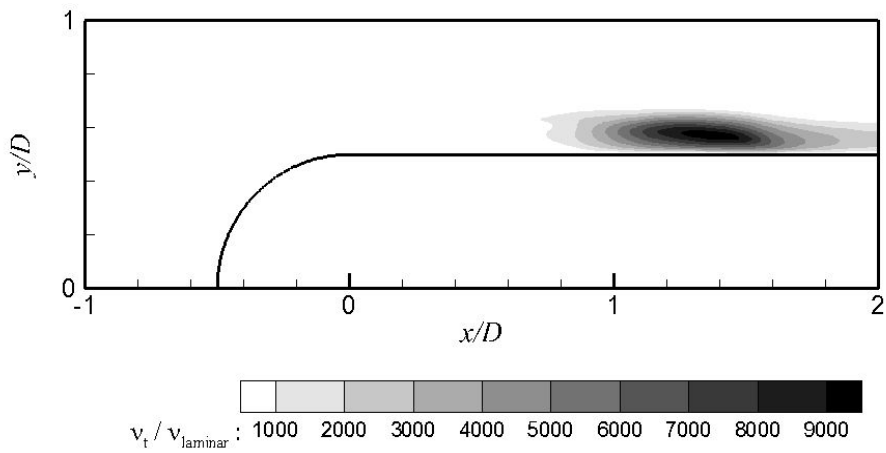


(b) Isothermal compressible flow solver

Figure 57. Streamwise velocity component contours and streamlines with the greatest length of re-entrant jet.



(a) Incompressible flow solver



(b) Isothermal compressible flow solver

Figure 58. Turbulent viscosity contours with the greatest length of re-entrant jet.

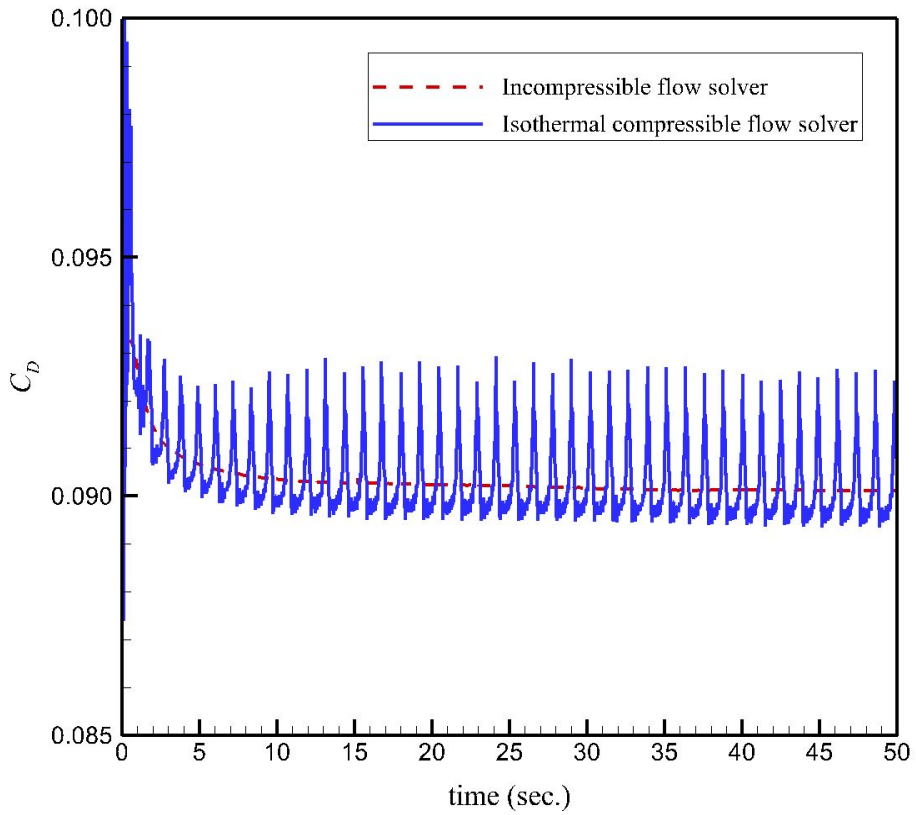


Figure 59. Drag coefficient history in surface of $0 \leq x/D \leq 2$.

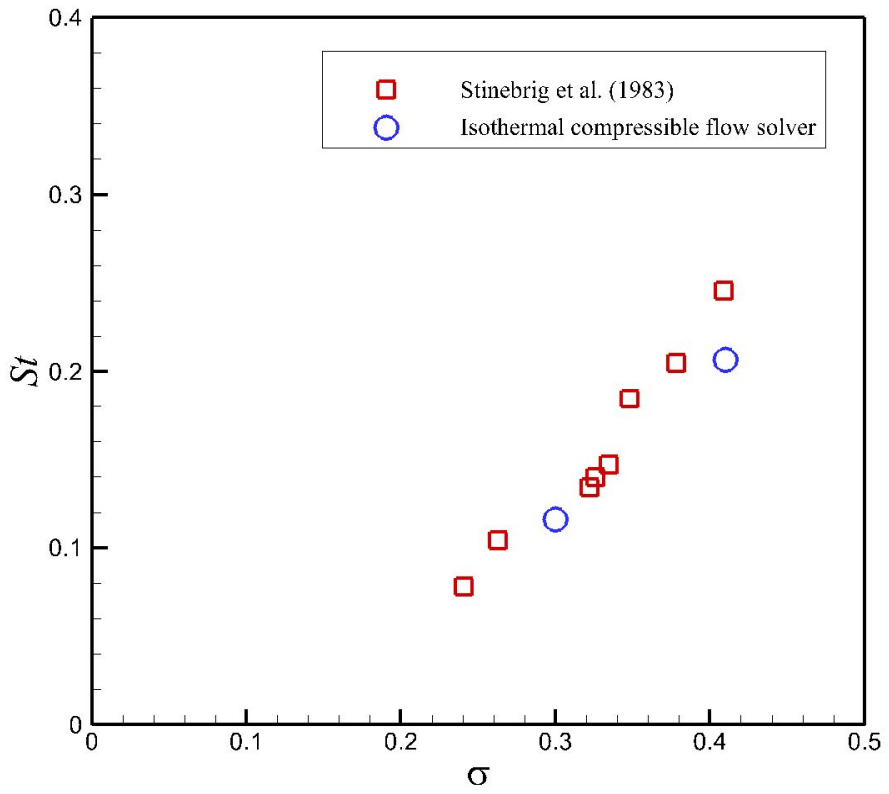


Figure 60. Strouhal number.

The cavity shedding frequency obtained by the drag coefficient's time history was compared with the existing experimental data (Stinebring et al., 1983). Stinebring et al. (1983) carried out a series of experiments on the ventilated and natural cavitation around axi-symmetric configuration with Reynolds number of 0.35×10^5 to 0.55×10^5 . Figure 60 compares the computed and measured cavity shedding frequencies for the hemispherical head-form body. The Strouhal number (St) was calculated using the obtained cavity shedding frequency. The Strouhal number of the cavitating flow predicted by the incompressible flow solver was zero. On the other hand, the overall trend well captured by the isothermal compressible flow solver.

Chapter 5. Cavitation Erosion Coefficient

In the previous chapter, cavitating flows were simulated using the developed incompressible and isothermal compressible flow solvers. The isothermal compressible cavitating flow solver was well predicted the cavity dynamics compare to the incompressible cavitating flow solver. Thus, cavitating flows in a converging-diverging nozzle and around a hydrofoil were simulated to obtain cavitation erosion coefficient using the isothermal compressible cavitating flow solver.

5.1 Converging-diverging nozzle

In the Cartesian coordinate system adopted, the nozzle height, h , is given by

$$h/H = \frac{const.}{e^{(x/3.5H)} + e^{(x/0.45H)}} \quad (42)$$

where x was the horizontal channel location and H was the channel height of 0.05 m. The radius of the curvature at $x/H = 0.3$ was 2.5. A rectangular bump attached the curvature was 1 mm long, 0.5 mm high, as shown in Figure 61. The cavity and cavitation erosion observation tests were carried out in the cavitation tunnel of the Technical University of Darmstadt (Keil et al., 2011). The test section of this tunnel was 0.5 m long, 0.1 m high, and 0.05 m wide.

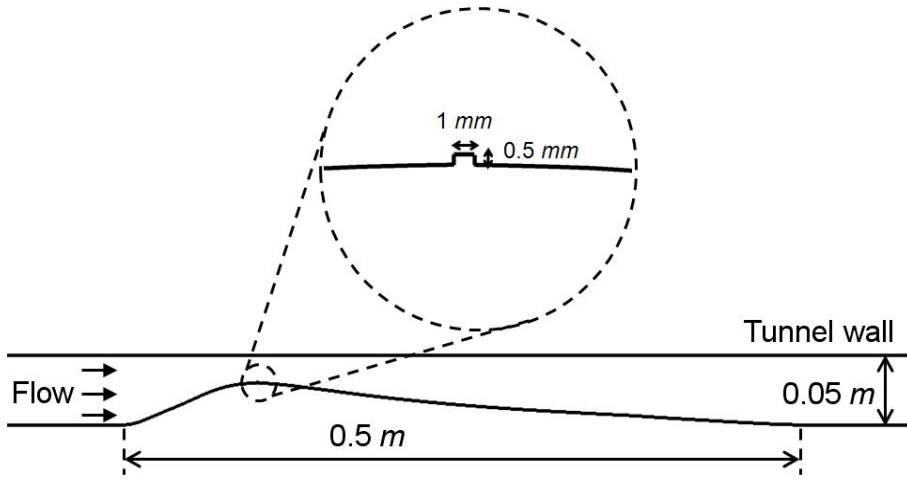


Figure 61. Problem description of converging-diverging nozzle.

The Reynolds number (Re), based on the free stream velocity (U_∞) and channel height, was in the range of 2.75×10^5 to 3.5×10^5 , while the cavitation number was in the range of 5.45 to 6.05. The test conditions are summarized in Table 11. Cavitation begins to form in the low-pressure region behind the rectangular bump as in the backward facing step flow and propagates downstream.

Table 11. Test conditions of converging-diverging nozzle.

$Re (\times 10^5)$	σ	$U (m/s)$	$P_o (Pa)$
2.75	5.45	5.526	85494.7
2.75	5.70	5.526	89305.5
2.75	6.05	5.526	94640.5
3.50	5.45	7.034	136987.3

A two-dimensional solution domain was considered following the test configuration. The solution domain extent shown in Figure 62 was $-10 \leq x/H \leq 20$, and $0 \leq y/H \leq 1$. The left inlet boundary was specified as the Dirichlet boundary condition, i.e., the fixed value of the velocity. On the right exit boundary, the reference pressure with the extrapolated velocity and the volume fraction was applied. The reference pressure was taken from the exit boundary. A no-slip condition was applied to the nozzle surface, and a free slip condition was applied to the tunnel boundaries. A structured grid consisting of 14,000 cells with 450 cells on the x -axis and 30 cells in the y -axis was used as shown in Figure 63.

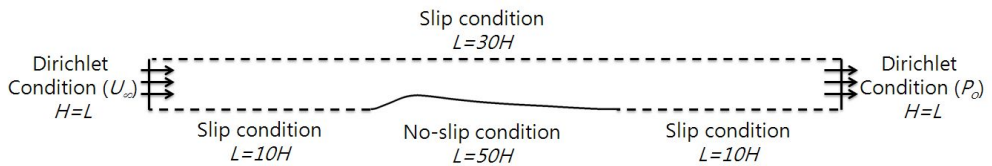


Figure 62. Boundary conditions and domain extent of converging-diverging nozzle.

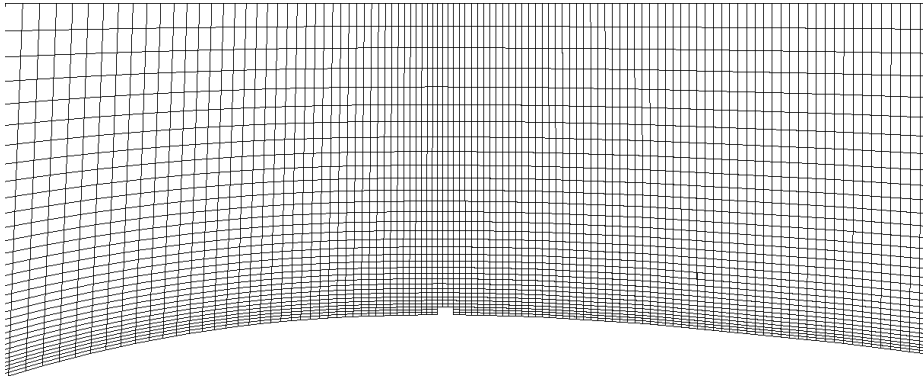


Figure 63. Mesh for converging-diverging nozzle.

To tame the computational instability caused by the large difference in the density and the high rate of mass transfer, the cavitating flow was computed with the converged single phase solution at a large cavitation number. The non-dimensional time step, tU_∞/H , was 0.00011 and the computation of each time step was finished when the scaled residuals for all the solution variables had dropped by at least six orders of magnitude.

Figure 64 shows the non-dimensionalized sheet cavity length, l_c/H , for various Reynolds and cavitation numbers, and compared with the experimental data (Keil et al., 2010). In the computations with the Reynolds numbers of 2.35×10^5 and 3.5×10^5 , and the cavitation number of 6, the computed cavity length was slightly longer than that of the experiment. In the overall computations, the results showed quite a close agreement.

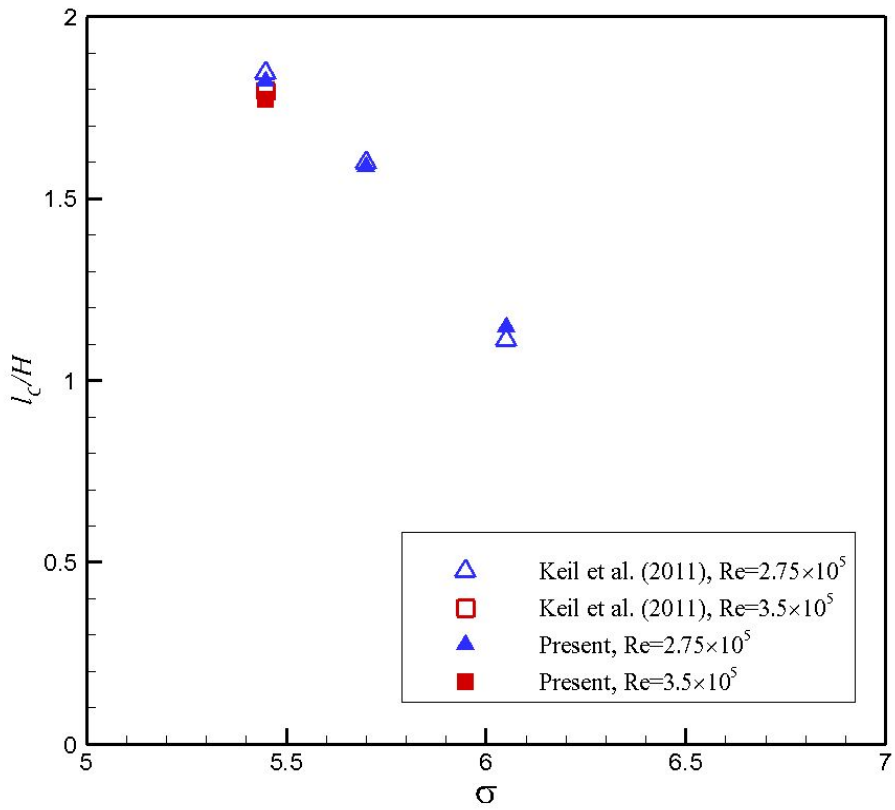
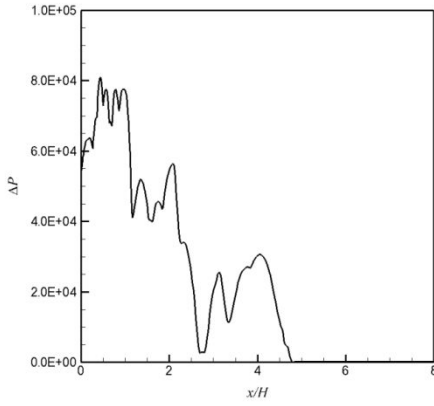
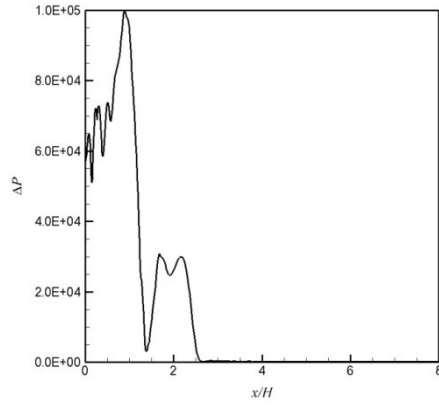


Figure 64. Sheet cavity length of converging-diverging nozzle.

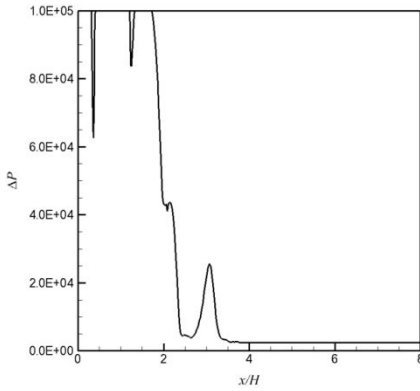
Figure 65 shows the pressure difference, which including the mean and fluctuating pressure differences, on the nozzle surface behind the rectangular bump. The large pressure difference were observed in a strongly fluctuated cavitating flow. The cavity dynamics were seen in a more wide range than the sheet cavity length. Keil et al. (2011) measure the damaged extent, as shown in Figure 66. With the assumption that the computational results simulated the experimental results well, the pressure difference could be calculated from the damaged extent, as shown in Figure 65. Thus, cavitation erosion coefficients could be calculated for various Reynolds numbers and cavitation numbers. Table 12 summarizes cavitation erosion coefficients. The cavitation number was the dominant factor influencing the damage extent by cavitation erosion. In the experiments (Keil et al, 2011), observed cavitation erosion extent depended on the cavitation number not the Reynolds number.



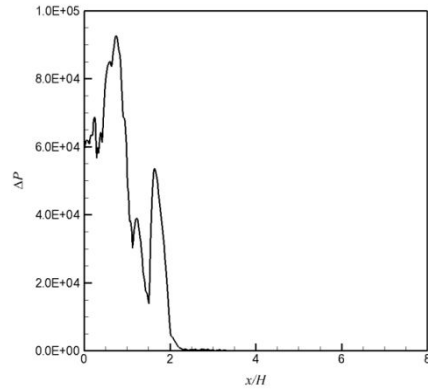
(a) Cavitation number of 5.45
and Reynolds number of 2.75×10^5



(b) Cavitation number of 5.70
and Reynolds number of 2.75×10^5



(c) Cavitation number of 6.05
and Reynolds number of 2.75×10^5



(d) Cavitation number of 5.45
and Reynolds number of 3.5×10^5

Figure 65. Pressure difference of converging-diverging nozzle.

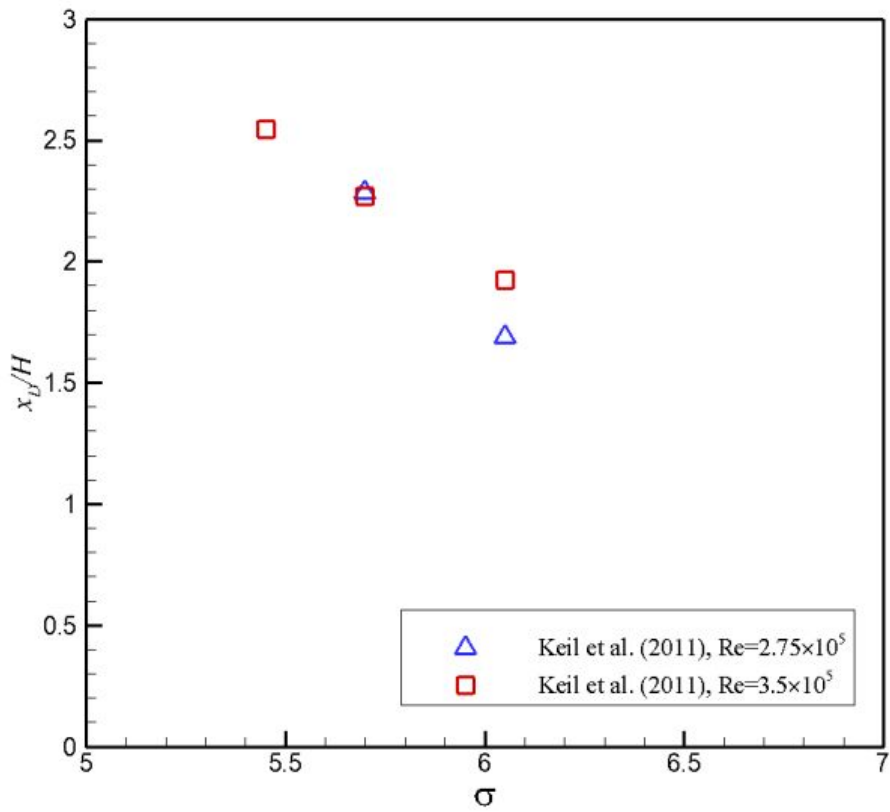


Figure 66. Damage extent by cavitation erosion of converging-diverging nozzle (Keil et al., 2011).

Table 12. Cavitation erosion coefficient of converging-diverging nozzle.

$Re (\times 10^5)$	σ	C_{ce}
2.75	5.45	71.81
2.75	5.70	75.18
2.75	6.05	81.04
3.50	5.45	71.81

5.2 Hydrofoil

The hydrofoil had a circular leading edge and constant thickness of 0.0016 mm , having a wedge shape near the trailing edge, and was symmetric with respect to the span, as shown in Figure 67. The chord length was 0.1079 m and the span length was 0.05 m , both of which being determined by considering the cavitation tunnel size. In the Cartesian coordinate system adopted here, the positive x-axis was in the chordwise direction, and the positive y-axis was in the spanwise direction, and the positive z-axis was in the normal direction of the surface. The cavity and cavitation erosion observation tests were carried out in the cavitation tunnel of the Technical University of Darmstadt (Dular and Coutier-Delgosha, 2009). The test section of this tunnel was 0.5 m long, 0.1 m high, 0.05 m wide. A developed cavitating flow was observed at 5° incidence angle.

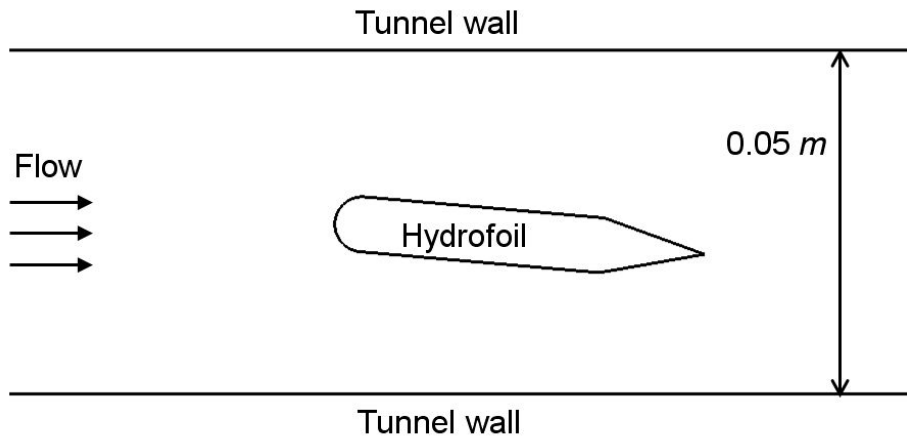


Figure 67. Problem description of hydrofoil.

The Reynolds number (Re), based on the free stream velocity (U_∞) of 13.0 m/s and chord length of 0.1079 m , was 1.04×10^6 , while the cavitation number (σ) was 2.0 .

The two-dimensional solution domain was considered conforming to the test setup. The solution domain extent was $-10 \leq x/C \leq 10$, and $-0.5 \leq y/C \leq 0.5$ (see Figure 68). The left inlet boundary was specified as the Dirichlet boundary condition, i.e., the fixed value of the velocity. On the right exit boundary, the reference pressure with the extrapolated velocity and the volume fraction was applied. The reference pressure was taken from the exit boundary. A no-slip condition was applied to the hydrofoil surface, and a free slip condition was applied to the tunnel boundaries. A H-type structured grid consisting of 12,000 cells with 250 cells on the surface and 60 cells in the normal direction was used as shown in Figure 69.

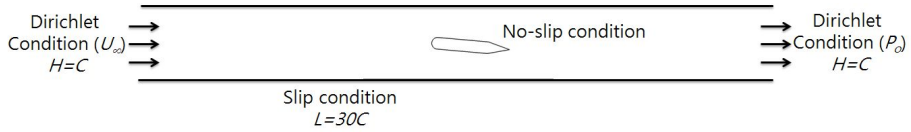


Figure 68. Boundary conditions and domain extent of hydrofoil.

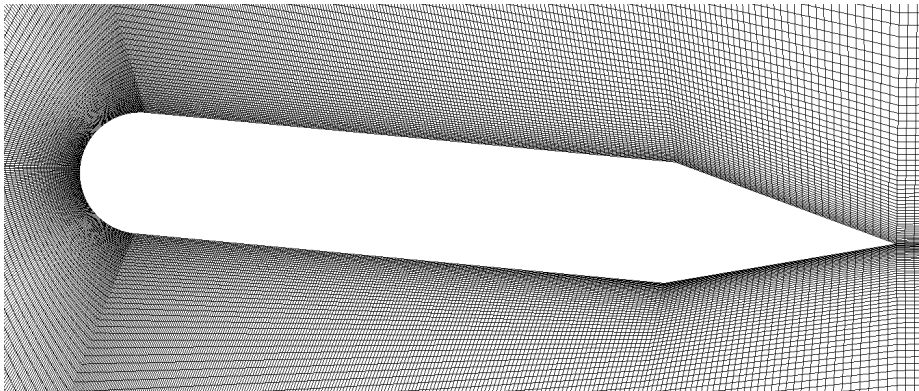


Figure 69. Mesh for Hydrofoil.

To tame the computational instability, the cavitating flow was computed with the converged single phase solution at a large cavitation number. The cavity was formed at the leading edge and transported to downstream. Figure 70 shows the pressure difference (ΔP), which including the mean and fluctuating pressure differences, on the hydrofoil surface. Cavitation erosion coefficient could be calculated by the same procedure for the converging-diverging nozzle. The damage extent with the Reynolds number of 1.38×10^6 and cavitation number of 2 was $x/C = 0.78$ (Dular and Coutier-Delgosha, 2009), and cavitation erosion coefficient was calculated to be 28.72.

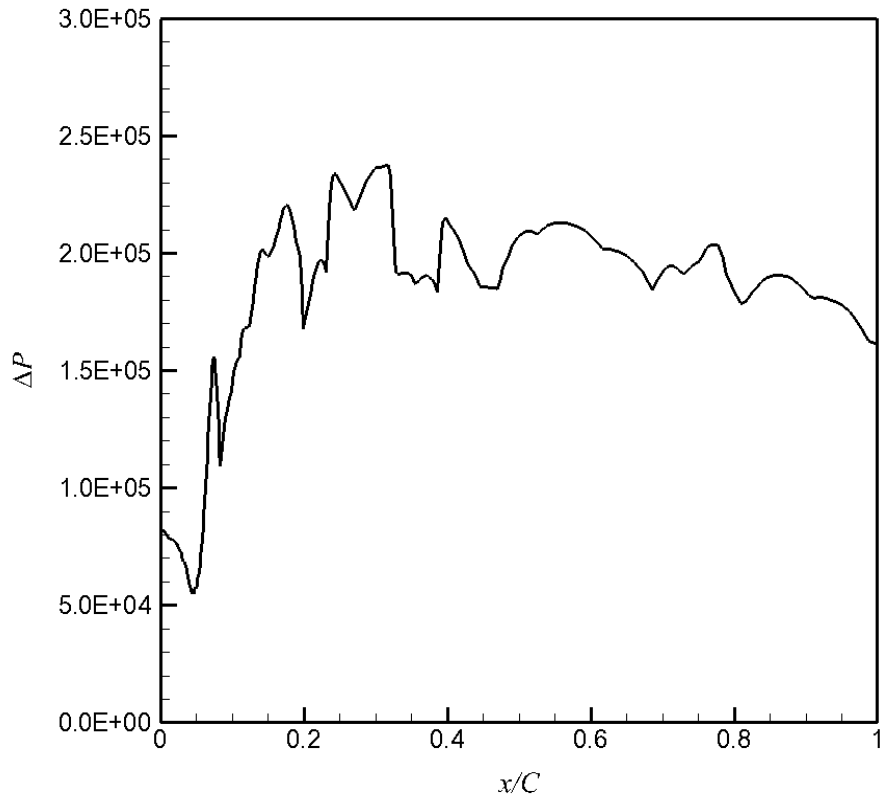


Figure 70. Pressure difference on hydrofoil surface.

5.3 Determination of cavitation erosion coefficient

In chapter 2, the cavitation erosion coefficient, C_{ce} , was expressed as a function of the cavitation, Reynolds, and Strouhal numbers. In the reference experimental studies (Dular and Coutier-Delgosha, 2009; Keil et al., 2011), the incubation time of cavitation erosion was not measured. Also, the consideration of the time was required the consideration of the space. Thus, in this paper, the function of the Strouhal number was treated as a constant, and then included in the cavitation erosion coefficient.

$$\begin{aligned} C_{ce} &= f_1(\sigma) \times f_2(Re) \times f_3(St) \\ &= f_1(\sigma) \times f_2(Re) \end{aligned} \quad (43)$$

In the function of the Reynolds number, the characteristic length could be selected as the cavity or geometry length. The cavity length was more reasonable in the small scale cavity flow. However, in this paper, the geometry based characteristic length was selected to develop the general practical method.

To develop the practical method for the prediction of cavitation erosion, metamodeling and curve fitting methods were used in this paper. A metamodeling method was used in the design engineering for the optimization.

5.3.1 Kriging metamodeling method

To develop the practical method for the prediction of cavitation erosion, a metamodeling method was considered. Metamodels have been developed with a variety of design optimization techniques in the structural and fluid engineering fields over the last decade because they are efficient, show excellent prediction performance, and provide easy interconnections into design frameworks. Response surface methodology (RSM) and kriging metamodels were widely used. A RSM metamodel was based on the optimization method that built linear or quadratic local approximations. While, a kriging metamodel was more flexible than polynomial models in fitting arbitrary smooth response functions, and seem to be less sensitive than radial basis functions in the experiment design (Meckesheimer et al., 2002). Also, a kriging metamodel showed the accuracy in the highly nonlinear problems. Thus, in this paper, a kriging metamodel was selected. A kriging metamodel was postulated a combination of a global model plus departures (Simpson et al., 1998; Sacks et al., 1989; Jin et al., 2001).

$$y(x) = f(x) + z(x) \tag{44}$$

where $y(x)$ was the unknown function of interest, $f(x)$ was a known (usually polynomial) function of x , and $z(x)$ was the realization of a stochastic process

with mean zero, variance σ^2 , and non-zero covariance. The $f(x)$ was similar to the polynomial model in a response surface and provided a “global” model of the design space. In many cases $f(x)$ was simply taken to be a constant term (Sacks et al., 1989). While $f(x)$ was “globally” approximated the design space, $z(x)$ created “localized” deviations so that the kriging model interpolated the n_s sampled data points. The covariance matrix of $z(x)$ was given by

$$Cov[z(x^i), z(x^j)] = \sigma^2 R([R(x^i, x^j)]) \quad (45)$$

Here, R was the correlation matrix, and $R(x_i, x_j)$ was the correlation function between any two of the n_s sampled data points x_i and x_j . R was a $(n_s \times n_s)$ symmetric matrix with ones along the diagonal. The correlation function $R(x_i, x_j)$ was defined as many functions (Sack et al., 1989). In this work, a Gaussian correlation function of the following form was selected.

$$R(x^i, x^j) = \exp\left[-\sum_{k=1}^{n_{dv}} \theta_k |x_k^i - x_k^j|\right] \quad (46)$$

where n_{dv} was the number of design variables, θ_k were the unknown correlation parameters used to fit the model, and the x_k^i and x_k^j were the k_{th} components of sample points x_i and x_j . In some cases using a single correlation parameter gave sufficiently good results (Welch et al., 1990).

Predicted estimates, $\hat{y}(x)$, of the response $y(x)$ at untried values of x were given by

$$\hat{y} = \hat{\beta} + r^T(x)R^{-1}(y - f\hat{\beta}) \quad (47)$$

where y was the column vector of length n_s which contained the sample values of the response, and f was a column vector of length n_s which was filled with ones when $f(x)$ was taken as a constant. $r^T(x)$ was the correlation vector of length n_s between an untried x and the sampled data points $\{x^1, \dots, x^{n_s}\}$.

$$r^T(x) = [R(x, x^1), R(x, x^1), \dots, R(x, x^{n_s})]^T \quad (48)$$

$\hat{\beta}$ was estimated as

$$\hat{\beta} = (f^T R^{-1} f)^{-1} f^T R^{-1} y \quad (49)$$

The estimate of the variance, $\hat{\sigma}^2$, between the underlying global model $\hat{\beta}$ and y , was estimated as

$$\hat{\sigma}^2 = \frac{(y - f\hat{\beta})^T R^{-1} (y - f\hat{\beta})}{n_s} \quad (50)$$

where $f(x)$ was assumed to be the constant $\hat{\beta}$. The maximum likelihood was estimated (i.e., “best guesses”) for the θ_k used to fit the model were found by maximizing following equation over $\theta_k > 0$ (Booker et al., 1995).

$$-\frac{[n_s \ln(\hat{\sigma}^2) + \ln|R|]}{2} \quad (51)$$

Both $\hat{\sigma}^2$ and $|R|$ were functions of θ_k .

Figure 71 show the predicted cavitation erosion coefficient by the kriging metamodel. The predicted cavitation erosion coefficient was available at the cavitation number range of 2 to 6.05 and Reynolds number range of 2.75×10^5 to 13.8×10^5 . In Figure 71, the predicted cavitation erosion coefficient included some error beyond the design points due to small number of the design points, which indicated selected cavitation and Reynolds numbers for the converging-diverging nozzle and hydrofoil. Also, beyond the cavitation and Reynolds numbers range, the predicted cavitation erosion coefficients included the some error due to the extrapolation. The cavitation erosion coefficients for the cavitation number range of 2 to 6.05 and Reynolds number range of 2.75×10^5 to 13.8×10^5 was listed in Appendix.

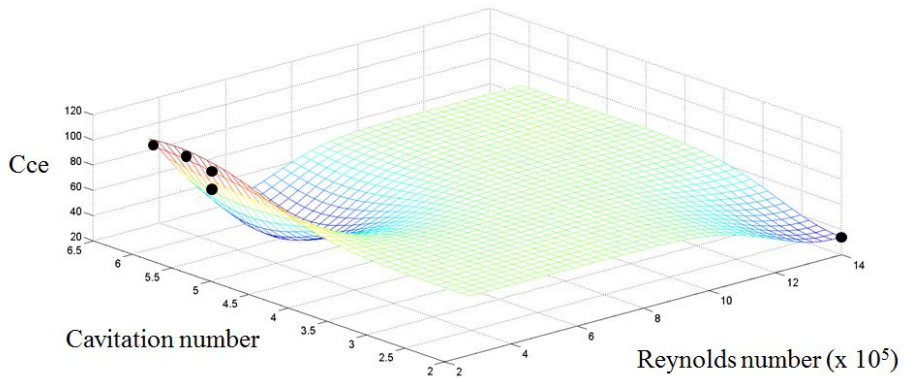


Figure 71. Predicted cavitation erosion coefficient by kriging metamodel
(circle symbol: design points).

5.3.2 Curve fitting method

The practical method for the prediction of cavitation erosion was developed using a curve fitting method. The pressure difference from the converging-diverging nozzle and hydrofoil for various cavitation and Reynolds numbers are shown in Figure 72 and Figure 73, respectively. The pressure difference for cavitation numbers decreased as an exponential function, while the pressure difference for Reynolds numbers increased as an

exponential function. An exponential function was selected to formulate the influence of the cavitation number. In the experiments by Keil et al. (2011), the influence of the Reynolds number was not large. Thus, in the present study, the influence of the Reynolds number was not large because the computations were based on the experimental data. A log function was selected instead of an exponential function due to the small influence at the Reynolds number. When cavitation erosion was predicted at a high Reynolds number, the error due to the Reynolds number would be decreased. The function of the cavitation number was induced first, and the remaining value of cavitation erosion coefficient was induced by the function of the Reynolds number in serial because the influence of the cavitation number was more dominant than the Reynolds number. Cavitation erosion coefficients were formulated as

$$\begin{aligned}
 C_{ee} &= f_1(\sigma) \times f_1(Re) \\
 &= (5.63 e^{-0.52\sigma} - 10) \times (2.65 \ln(Re) - 10.57) \quad (52)
 \end{aligned}$$

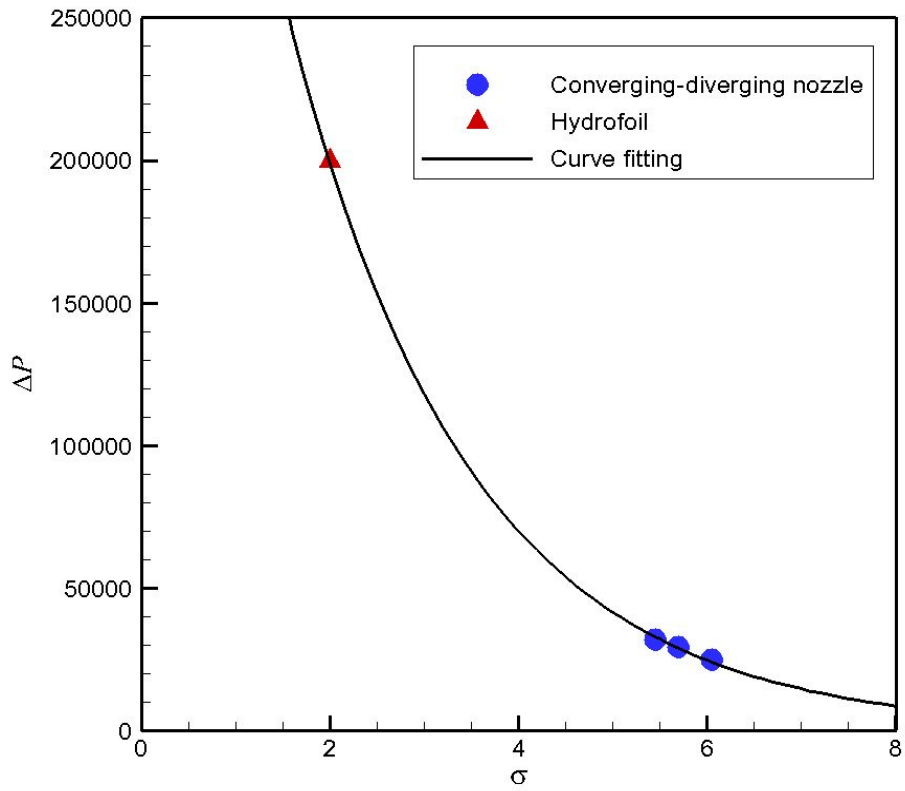


Figure 72. Pressure difference for cavitation number.

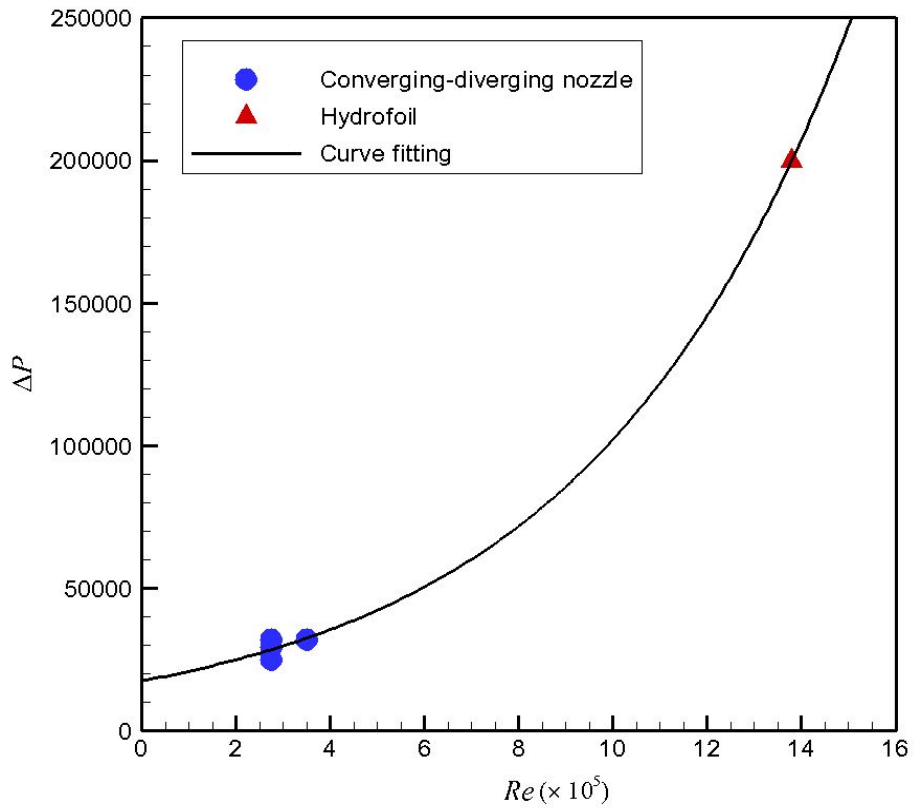


Figure 73. Pressure difference for Reynolds number.

The deviation, R^2 , of the curve fitting equation was 0.96. The deviation was defined as

$$R^2 = 1 - \frac{\sum (Y_i - Y_m)^2}{(\sum Y_i^2) - (\sum Y_i)^2/n} \quad (53)$$

where Y_m was the averaged value and n was the number of Y_i .

Chapter 6. Validation and Application

The developed practical method for the prediction of cavitation erosion was validated by applying it to an axisymmetric nozzle followed by radial divergence, and applied it to a marine propeller. The practical method was developed in the two-dimensional flows. The expansion to the three-dimensional flows of the developed practical method was reasonable because the fluid properties, turbulence, and cavitation were solved with an assumption of a homogeneous flow.

6.1 Validation

A cavitating flow in an axisymmetric nozzle followed by radial divergence was simulated to validate the developed practical method. The test section was axisymmetric and made of a nozzle of 16 mm in diameter followed by a radial divergent of 2.5 mm in thickness, as shown in Figure 74. The setup of the experimental facility and cavitation erosion observation tests were conducted in a cavitation tunnel (Franc, 2009).

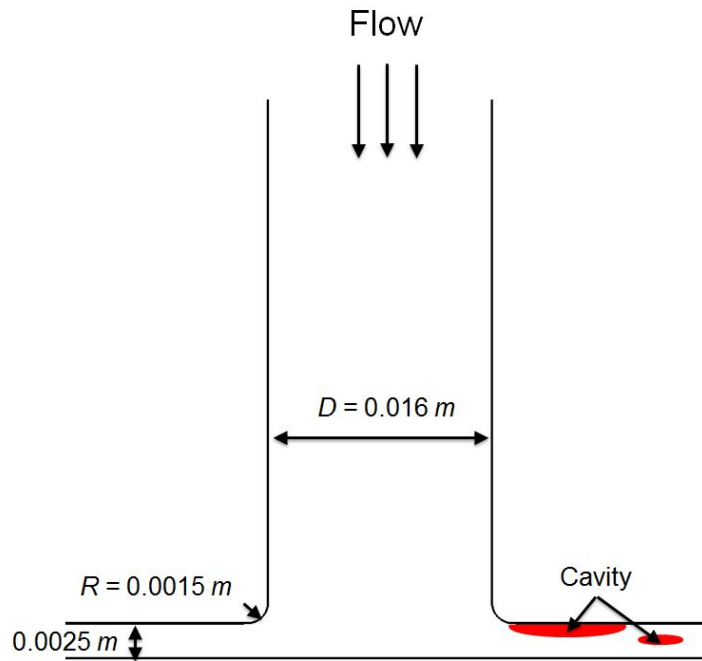


Figure 74. Problem description of axisymmetric nozzle followed by radial divergence.

The Reynolds number (Re), based on the free stream velocity (U_∞) of 31 m/s and a radial divergent nozzle height of 0.0025 m , was 7.75×10^5 , while the cavitation number (σ) was 2.1. A cavity was attached to the nozzle exit.

The developed cavitation erosion coefficient was validated and confirmed by the simulation of the cavitating flow in a nozzle followed by a radial divergence. Cavitation erosion extent was predicted using the developed prediction method, and then compared with the existing experimental data.

The axisymmetric solution domain was considered, as shown in Figure 75. The solution domain extent was $0 \leq x/H \leq 40$, and $0 \leq y/H \leq 40$. Here, H was 0.0025 m. The top boundary was specified as the Dirichlet boundary condition, i.e., the fixed value of the velocity. On the right exit boundary, the reference pressure with the extrapolated velocity and the volume fraction was applied. The reference pressure was taken from the exit boundary. A no-slip condition was applied to the nozzle surface, and an axisymmetric condition was applied to the left axisymmetric boundary. A H-type structured grid consisting of 10,000 cells with 100 cells on the horizontal nozzle surface and 200 cells in the vertical nozzle surface was used.

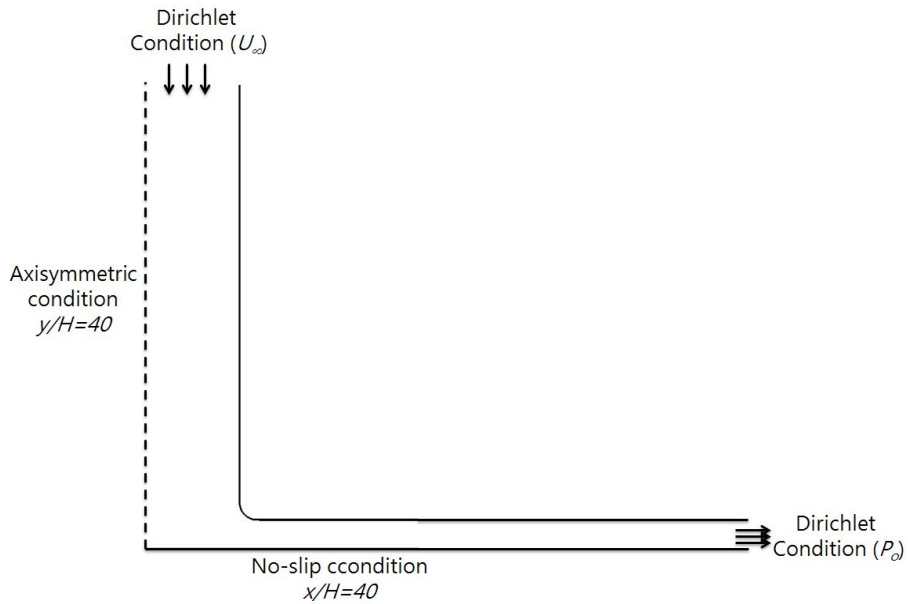


Figure 75. Boundary conditions and domain extent of axisymmetric nozzle followed by radial divergence.

To tame the computational instability, the cavitating flow was computed with the converged single phase solution at a large cavitation number. Figure 76 and Figure 77 show the pressure coefficient and vapor volume fraction contours, respectively. The stagnation pressure coefficient of 1 was observed at the center of lower disk. The cavity formed a curved surface, and showed a shedding dynamics.



Figure 76. Pressure coefficient contours of axisymmetric nozzle followed by radial divergence.

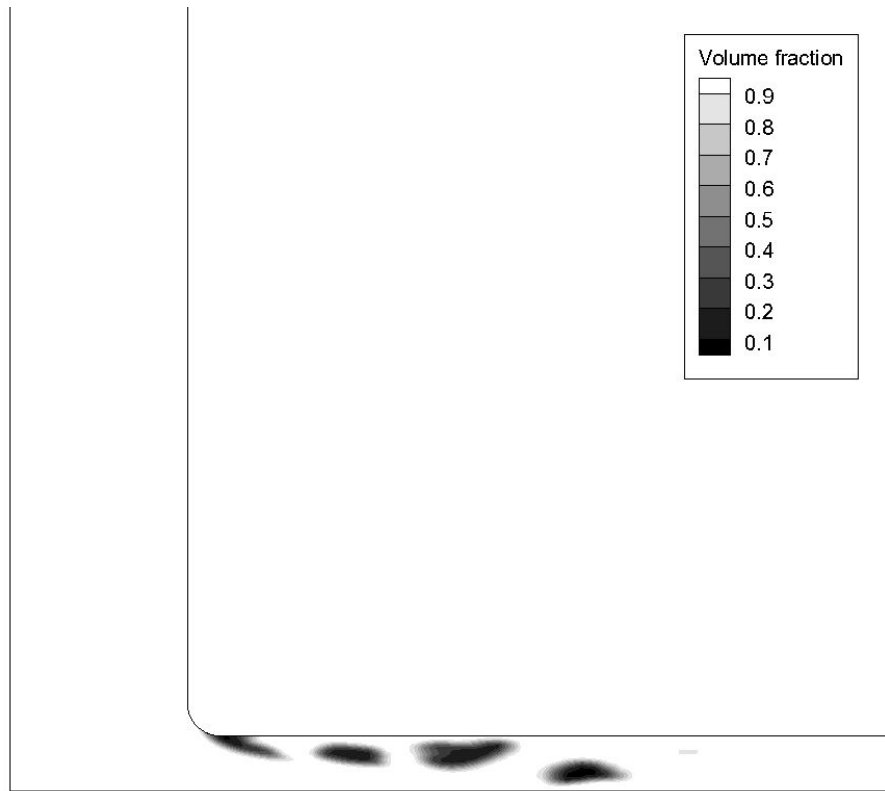


Figure 77. Vapor volume fraction contours of axisymmetric nozzle followed by radial divergence.

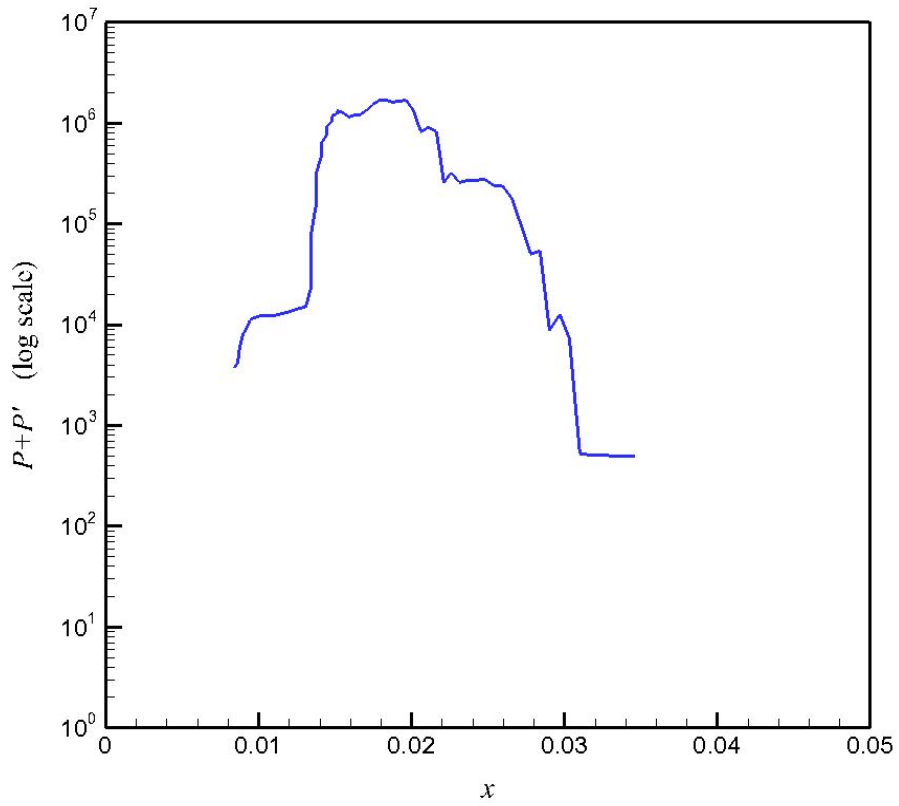


Figure 78. Pressure difference of axisymmetric nozzle followed by radial divergence.

Figure 78 shows the pressure difference, which including the mean and fluctuating pressure differences, on the radially diverged top surface. The impact and critical velocities could be calculated using the developed cavitation erosion coefficient. Calculated damage extent was 0.030 *m*. In the experiment, the damage extent was seen to 0.032 *m* (Franc, 2009). Predicted damage extent showed nearly good agreement with the experimental data.

6.2 Application

Developed and validated practical method for the prediction of cavitation erosion was applied to a marine propeller. In a marine engineering, cavitation erosion on a propeller surface has been issued and is a critical problem.

KP505, which was designed for a propeller of a 3,600 TEU container carrier, was selected as the object propeller. The principal particulars are described in Figure 79. A five-bladed propeller with a diameter of 0.25 *m* was selected. The blade consisted of the NACA66 foil section, which is a popular blade section geometry for marine propellers.

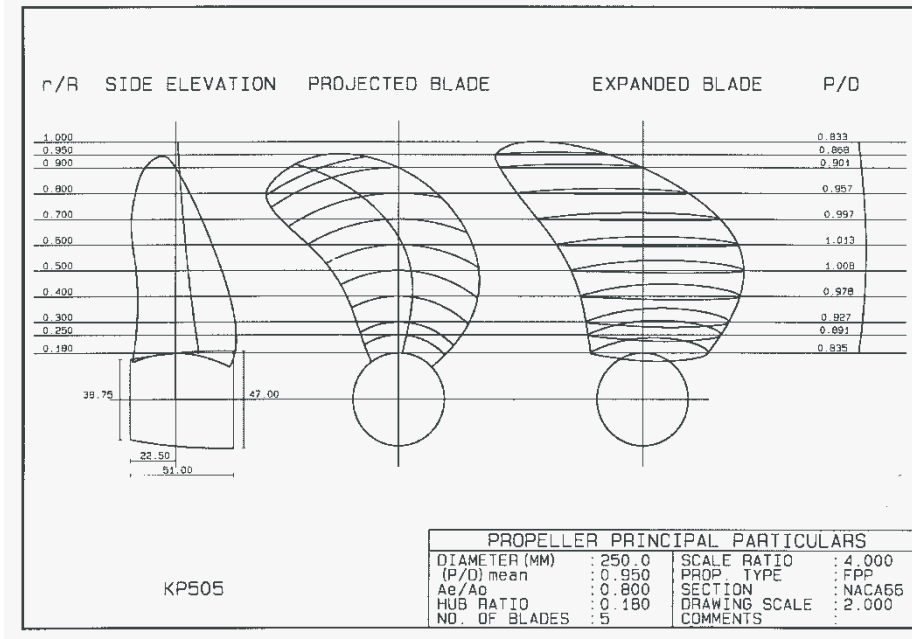


Figure 79. Principal particulars of KP505.

The advance ratio (J), based on the free stream velocity (U_∞) of 3.125 m/s , the diameter of the propeller of 0.025 m , and the revolution rate of 25 rps , was 0.3. The Reynolds number (Re) was 7.22×10^5 , while the cavitation number (σ) was 1.5.

In the present study, a rotating reference frame was used to accommodate the propeller revolution in the open water condition. With the rotating reference frame, only one blade needed to be modeled with periodic

boundaries on the sides. The computational domain's extent was a length of $12D$ and a radius of $3D$, where D represents the turbine diameter. The inlet and outlet boundaries were located at $4D$ upstream and $8D$ downstream, respectively.

The inlet boundary was specified as the Dirichlet boundary condition, i.e., the fixed value of the velocity. On the exit boundary, the reference pressure with the extrapolated velocity and the volume fraction was applied. The reference pressure was taken from the exit boundary. A no-slip condition was applied to the blade surface, and a periodic condition was applied to the side boundary.

Hybrid meshing was used. The whole domain was divided into two sub-domains, the one with the blade was filled with tetrahedral cells and the others with simple geometry were filled with hexahedral cells for a high quality solution. By this approach, it was possible to get rid of the difficulty of mesh generation around complex geometries. A total cell count of about 0.4 million was used for the structured mesh. On each blade surface, 100 and 400 cells were put in the chordwise and spanwise directions. As for the hybrid mesh, finer cells were used near the blade tip, the leading and trailing edges as shown in Figure 80.

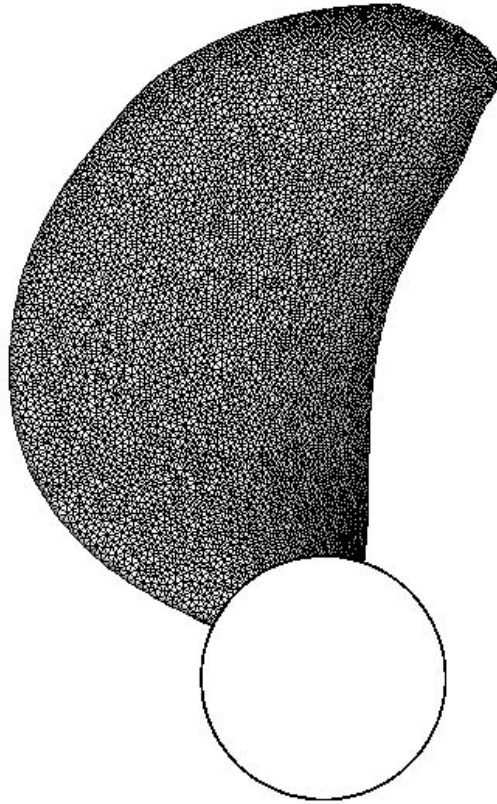


Figure 80. Mesh for KP505 propeller blade.

To tame the computational instability caused by the large difference in the density and the high rate of mass transfer, the cavitating flow was computed with the converged single phase solution at a large cavitation number. Figure 81 and Figure 82 show the pressure coefficient contours on the pressure and suction blades in the non-cavitating flow, respectively. High and low pressure coefficient peaks were observed at $r/R=0.7$ on the pressure and suction blades, respectively.

Figure 83 shows generated cavity on the suction blade. The cavity interface was captured with the volume fraction of 0.5. The cavity was generated at the leading edge of $r/R=0.7$ and propagated to the blade tip.

Figure 84 shows predicted cavitation erosion extent. Cavitation erosion extent was predicted near the cavity closure at $r/R = 0.8$. Figure 85 shows a snap shot for cavitation erosion of a propeller blade. The predicted cavitation erosion extent was similar with the measured one.

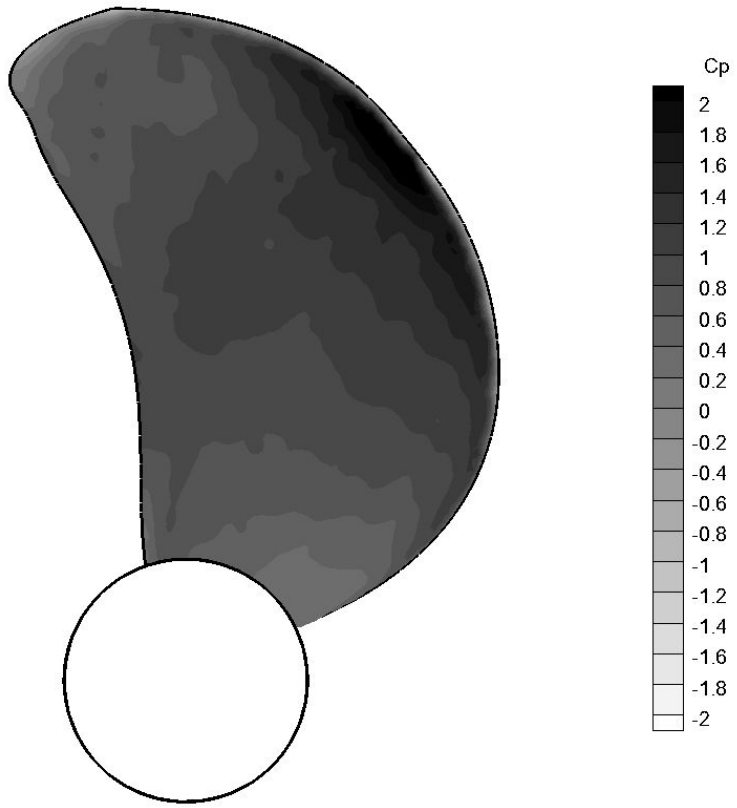


Figure 81. Pressure coefficient contours on pressure blade.

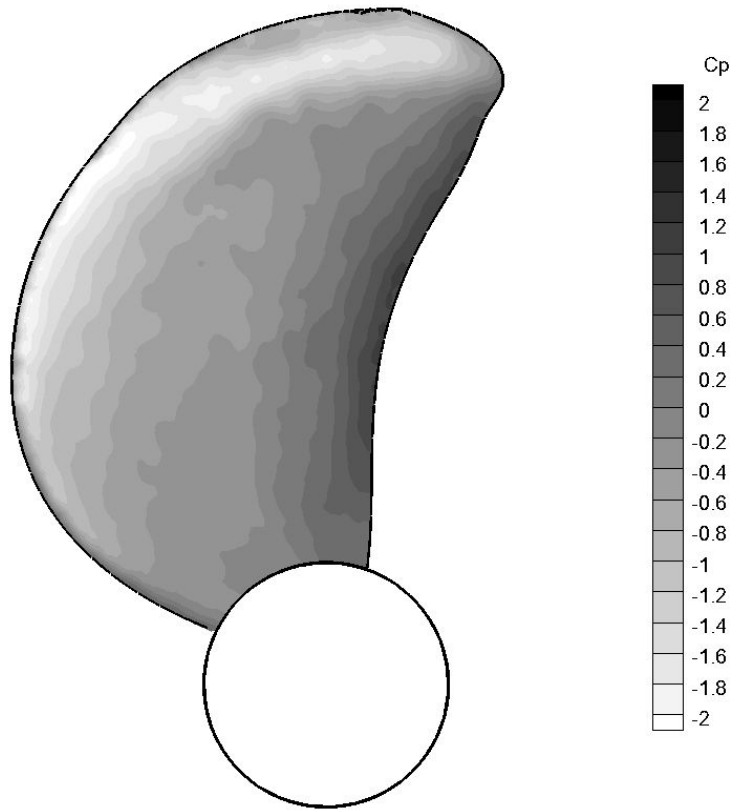


Figure 82. Pressure coefficient contours on suction blade.

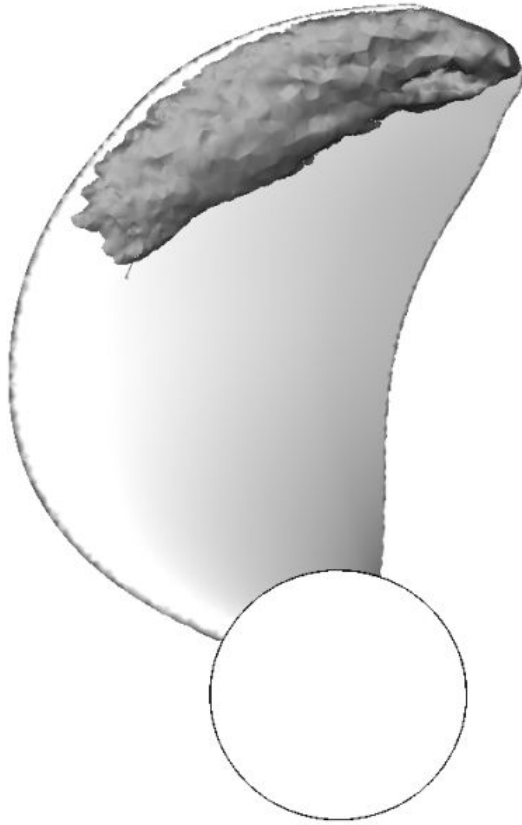


Figure 83. Cavitation on KP505 propeller blade.

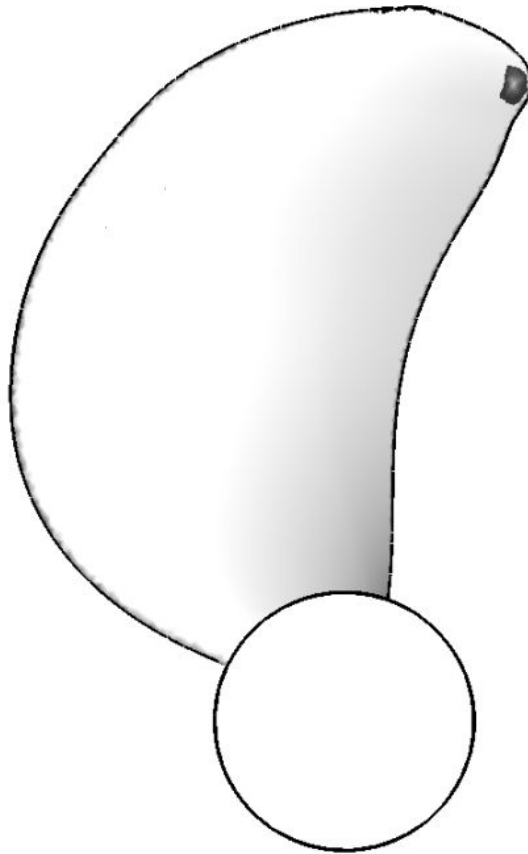


Figure 84. Predicted cavitation erosion extent on KP505 propeller blade.



Figure 85. Cavitation erosion on propeller blade.

Chapter 7. Conclusions

In this paper, a practical method for the prediction of cavitation erosion was developed. When an impact velocity was larger than a critical velocity, it was predicted that cavitation erosion could be observed. To define cavitation erosion, impact and critical velocities were introduced. To close the practical method, CFD analyses for cavitating flows were carried out.

To simulate cavitating flows, an in-house CFD code, termed SNUFOAM-Cavitation, was developed using OpenFOAM libraries. Incompressible and isothermal cavitating flow solvers were developed, respectively. To validate the developed solvers, sheet, super, and cloud cavitating flows were simulated and validated against existing experimental data. To simulate the cavity dynamics in the flow with cavitation erosion, the isothermal compressible flow solver was selected.

To close the practical method, cavitating flows with the erosion in a converging-diverging nozzle (Keil et al., 2011) and around a hydrofoil (Dular and Coutier-Delgosha, 2009) were simulated, and the cavitation erosion coefficient was derived by metamodeling and curve fitting methods. In the metamodeling method, a kiring metamodel was used. In the curve fitting method, the cavitation erosion coefficient was formulated as a function of Reynolds and cavitation numbers independently.

The developed practical method was validated by applying it to a cavitating flow in an axisymmetric nozzle followed by radial divergence. By

comparing the predicted cavitation erosion extent with the measured one, the developed practical method was practicable. Finally, cavitation erosion on a propeller blade was predicted. Predicted damage extent showed similar with damaged full scale propeller blade. The developed practical method helps predict cavitation erosion observed on the blades of pumps, turbines, and marine propellers.

Chapter 8. Future Works

In this paper, sheet, super, and cloud cavitations were studied. A bubble cavitation, which also caused a critical effect on cavitation erosion, was not considered in the cavitation erosion prediction method. The development of the cavitation erosion prediction method including the bubble cavitation is needed.

In the coefficient of cavitation erosion, the time was not included. To develop a very accurate prediction method for cavitation erosion, the Strouhal number, which means the cavity shedding, is considered in the cavitation erosion coefficient. To predict the cavitation erosion of the full scale propeller blade, the prediction method including a high Reynolds number is need. Also, the critical velocity including the fatigue, which caused cavitation erosion, is considered.

References

- Abouel-Kasem, A., Ahmed, S.M., 2008, "Cavitation erosion mechanism based on analysis of erosion particles," *Journal of Tribology*, 130, pp. 031601-6.
- Ahn, B.K., Lee, C.S., Kim, H.T., 2010, "Experimental and numerical studies on super-cavitating flow of axisymmetric cavitators," *International Journal of Naval Architecture and Ocean Engineering*, 2, pp. 39-44.
- Ahn, B.K., Lee, T.K., Kim, H.T., Lee, C.S., 2012, "Experimental investigation of supercavitating flows," *International Journal of Naval Architecture and Ocean Engineering*, 3, pp. 123-131.
- Ahuja, V., Hosangadi, A., Arunajatesan, S., 2001, "Simulations of cavitating flows using hybrid unstructured meshes," *Journal of Fluids Engineering*, 253, pp. 3685-3692.
- Booker, A.J., Conn, A.R., Dennis, J.E., Frank, P.D., Trosset, M., Torczon, V., 1995, "Global Modeling for Optimization: Boeing/IBM/Rice Collaborative Project," ISSTECH-95-032, Seattle, WA.
- Bark, G., Grekula, M., Bensow, R.E., Berchiche, N., 2009, "On some physical to consider in numerical simulation of erosive cavitation," 7th International Symposium on Cavitation, Ann Arbor, USA.
- Berchiche, N., Franc, J.P., Michel, J.M., 2002, "A cavitation erosion model for ductile materials," *Journal of Fluids Engineering*, 124, pp. 601-606.
- Bilanceri, M., Beux, F., Salvetti, M.V., "An implicit low-diffusive HLL scheme with complete time linearization: Application to cavitating

- barotropic flows,” *Computers & Fluids*, 39, pp. 1990-2006.
- Brennen, C.E., 1995, “Cavitation and bubble dynamics,” 1st ed, Oxford University Press, Oxford, UK.
- Brockett, T., 1966, “Minimum pressure envelopes for modified NACA-66 Section with NACA $a = 0.8$ camber and buships type I and type II sections,” Report 1780, David Taylor Model Basin.
- Chahine, G.L., 2004, “Nuclei effects on cavitation inception and noise,” 25th Symposium on Naval Hydrodynamic, St. John’s, Newfoundland and Labrador, Canada; 8-13 August.
- Chen, Y., Heister, S.D., 1994, “A numerical treatment for attached cavitation,” *Journal of Fluids Engineering*, 190, pp. 299-307.
- Choi, J.Y., Ruzzene, M., 2006, “Stability analysis of supercavitating underwater vehicles with adaptive cavitator,” *International Journal of Mechanical Sciences*, 48, pp. 1360-1370.
- Delannoy, Y., Kueny, J.L., 1990, “Two phase flow approach in unsteady cavitation modeling,” *ASME Cavitation and Multiphase Flow Forum*, Toronto, Canada; 4-7 June.
- Dular, M., Stoffel, B., Sirok, B., 2007, “Development of a cavitation erosion model,” *WEAR*, 261, pp. 642-655.
- Dular M., Coutier-Delgosha, O., 2009, “Numerical modeling of cavitation Erosion,” *International Journal for Numerical Methods in Fluid*, 61, pp. 1388-1410.
- Edwards, J.R., Franklin, R.K., Liou, M.S., 2000, “Low-diffusion flux-splitting methods for real fluid flows with phase transitions,” *AIAA Journal*, 38(9),

pp. 1624-1633.

- Foeth, E.J., 2008, "The Structure of Three-dimensional Sheet Cavitation," Ph.D thesis, Delft University of Technology, Netherlands.
- Foeth, E.J., van Doorne, C.W.H., van Terwisga, B.W., 2006, "Time Resolved PIV and Flow Visualization of 3D Sheet Cavitation," *Experiments in Fluids*, 30(4), pp. 503-513.
- Foeth, E.J., van Terwisga, T., van Doorne, C., 2008, "On the collapse structure of an attached cavity on a three-dimensional hydrofoil," *Journal of Fluids Engineering*, 30, pp. 071303.1-9.
- Fortes-Patella, R., Challier, G., Rebound, J.L., 2001, "Cavitation erosion mechanism: numerical simulations of the interaction between pressure waves and solid boundaries," 4th International Symposium on Cavitation, Pasadena, California, USA, 20-23 June.
- Franc, J.P., 2009, "Incubation time and Cavitation erosion rate of work-hardening materials," *Journal of Fluids Engineering*, 131, pp. 021303.1-14.
- Grant, M.M., Lush, P.A., 1987, "Liquid impact on a bilinear elastic-plastic solid and its role in cavitation erosion," *Journal of Fluid Mechanics*, 176, pp. 237-252.
- Hattori, S., Nakao, E., 2002, "Cavitation erosion mechanisms and quantitative evaluation based on erosion particles," *WEAR*, 249, pp. 839-845.
- Hattori, S., Kishimoto, M., 2008, "Prediction of cavitation erosion on stainless steel components in centrifugal pumps," *WEAR*, 265, pp. 1870-1874.
- Hinze, J. O., 1975, "Turbulence," 2nd Ed. McGraw Hill, New York.
- Howe, M.S., Colgan, A.M., Brungart, T.A., 2009, "On self-noise at the nose

- of a supercavitating vehicle,” *Journal of Sound and Vibration*, 322, pp. 772-784.
- Hrubes, J.D., 2001, “High-speed imaging of supercavitating underwater projectiles,” *Experimental in Fluids*, 30, pp. 57-64.
- Hu, Z.M., Dou, H.S., Khoo, B.C., 2009, “On the modified dispersion-controlled dissipative (DCD) scheme for computation of flow supercavitation,” *Computers & Fluids*, 40, pp. 315-323.
- Issa, R. I., 1985, “Solution of Implicitly Discretized Fluid Flow Equations by Operator Splitting,” *Journal of Computational Physics*, 62, pp. 40–65.
- Jin, R., Chen, W., Simpson, T.W., 2001, “Comparative studies of metamodelling techniques under multiple modeling criteria,” *Structural and Multidisciplinary Optimization*, 23, pp. 1-13.
- Karimi, A., Avellan, F., 1986, “Comparison of erosion mechanisms in different types of cavitation,” *WEAR*, 113, pp. 305-322.
- Kato, H., Konno, A., Maeda, M., Yamaguchi, H., 1996, “Possibility of quantitative prediction of cavitation erosion without model test,” *Journal of Fluids Engineering*, 118, pp. 582-588.
- Keil, T. Pelz, P.F., Cordes, U., Ludwig, G., 2011, “Cloud cavitation and cavitation erosion in convergent divergent nozzle,” *WIMRC 3rd International Cavitation Forum*, University of Warwick, UK, 4-6 July.
- Kissling, K., Springer, J., Jasak, H., Schutz, S., Urban, K., Piesche, M., 2010, “A coupled pressure based solution algorithm based on the volume-of-fluid approach for two or more immiscible fluids,” *5th European Conference on Computational Fluid Dynamics*, Lisbon, Portugal, 14-17

June.

- Krella, A., Steller, J., 2011, "On fractional approach in modeling cavitation erosion processes," Experimental and Numerical Techniques for Cavitation Erosion Prediction, Grenoble, France, 1-2 March.
- Kubota, A., Kato, H., Yamaguchi, H., 1992, "A new modelling of cavitating flows: a numerical study of unsteady cavitation on a hydrofoil section," Journal of Fluid Mechanics, 240, pp. 59-96.
- Kunz, R.F., Boger, D.A., Stinebring, D.R., Chyczewski, T.S., Lindau, J.W., Gibeling, H.J., Venkateswaran, S., Govindan, T.R., 2000, "A preconditioned Navier-Stokes method for two-phase flows with application to cavitation prediction," Computer & Fluids, 29, pp. 849-875.
- Kunz, R.F., Stinebring, D.R., Chyczewski, T.S., Boger, D.A., Gibeling, H.J., 1999, "Multi-phase CFD analysis of natural and ventilated cavitation about submerged bodies," 3rd ASME/JSME Joint Fluid Engineering Conference, ASME Paper FEDSM 99-7364, San Francisco, California, 18-23 July.
- Lauder, B. E., and Spalding, D. B., 1972, Lectures in Mathematical Models of Turbulence, Academic Press, London, UK.
- van Leer, B., 1979, "Towards the Ultimate Conservative Difference Scheme," Journal of Computational Physics, 32(1), pp. 101-136.
- Li, X., Wang, G., Zhang, M., Shyy, W., 2008, "Structures of supercavitating multiphase flows," Journal of Thermal Sciences, 47, pp. 1263-1275.
- Lin, G., Balachandran, B., Abed, E.H., 2008, "Dynamics and control of supercavitating vehicles," Journal of Dynamics System, Measurement, and

- Control, 130, pp. 021003.1-11.
- Lindau, J.W., Kunz, R.F., Mulherin, J.M., Dreyer, J.J., Stinebring, D.R., 2003, "Fully coupled, 6-DOF to URANS, modeling of cavitating flows around a supercavitating vehicles," 5th International Symposium on Cavitation, Osaka, Japan, 1-4 November.
- Lush, P.A., 1983, "Impact of a liquid mass on a perfectly plastic solid," Journal of Fluid Mechanics, 135, pp. 373-387.
- Meckesheimer, M., Booker, A.J., Barton, R.R., Simpson, T.W., 2002, "Computationally inexpensive metamodel assessment strategies," AIAA Journal, 40, pp. 2053-2060.
- Merkle, C.L., Feng, J., Buelow, P.E.O., 1998, "Computational modeling of the dynamics of sheet cavitation," 3rd International Symposium on Cavitation, Grenoble, France; 7-10 April.
- Newman, J.N., 1977, "Marine hydrodynamics," 1st ed. The MIT Press, Massachusetts.
- Nouri, N.M., Eslamdoost, A., 2009, "An iterative scheme for two-dimensional supercavitating flow," Ocean Engineering, 36, pp. 708-715.
- Ochiai, N., Iga, Y., Nohmi, M., Ikohagi, T., 2009, "Numerical prediction of cavitation erosion in cavitating flow," 7th International Symposium on Cavitation, Ann Arbor, Michigan, USA, 17-22 August.
- Okada, T., Iwai, Y., Awazu, K., 1989, "A study of cavitation bubble collapse pressures and erosion. part 1: a method for measurement of collapse pressures," WEAR, 133, pp. 219-232.
- Park, S., Heo, J., Yu, B., 2010, "Numerical study on the gap flow of a semi-

- spade rudder to reduce gap cavitation,” *Journal of Marine Science and Technology*, 15, pp. 78-86.
- Park, S., Rhee, S.H., 2010, “Investigation for the characteristics of cavitation modeling for computational fluid dynamics,” *Journal of the Society of Naval Architecture of Korea*, 47(5), pp. 657-669 (in Korean).
- Park, S., Rhee, S.H., 2012, “Computational analysis of turbulent super-cavitating flow around a two-dimensional wedge-shaped cavitator geometry,” *Computers & Fluids*, 70, pp. 73-85.
- Park, S., Rhee, S.H., Shin, B.R., 2012, “Pressure-based solver for incompressible and isothermal compressible flows with cavitation,” 8th International Symposium on Cavitation, Singapore, 13-16 August.
- Park, S., Rhee, S.H., 2013, “Numerical analysis of the three-dimensional cloud cavitating flow around a twisted hydrofoil,” *Fluid Dynamics Research*, 45(1), pp. 015502.1-015502.20.
- Plesset, M.S., Chapman, R.B., 1971, “Collapse of an initially spherical vapor cavity in the neighborhood of a solid boundary,” *Journal of Fluid Mechanics*, 47, pp. 283-290.
- Rhee, S.H., Kawamura, T., Li, H., 2005, “Propeller Cavitation Study Using an Unstructured Grid Based Navier-Stokes Solver,” *Journal of Fluids Engineering*, 127, pp. 986-994.
- Richman, R.H., McNaughton, W.P., 1990, “Correlation of cavitation erosion behavior with mechanical properties of metals,” *WEAR*, 140, pp. 63-82.
- Rouse, H., McNown, J.S., 1948, “Cavitation and pressure distribution in engineering,” *Bulletin 32, State University of Iowa*.

- Sacks, J., Welch, W.J., Mitchell, T.J. and Wynn, H.P., 1989, "Design and Analysis of Computer Experiments," *Statistical Science*, 4(4), pp. 409-435.
- Saurel, R., Lemetayer, OI, 2001, "A multiphase model for compressible flows with interfaces, shocks, detonation waves and cavitation," *Journal of Fluid Mechanics*, 431, pp. 239-271.
- Savchenko, Y.N., 2001, "Supercavitation - problems and perspectives," 4th International Symposium on Cavitation, California, USA, 20-23 June.
- Schnerr, G.H., Sezal, I.H., Schmidt, S.J., 2008, "Numerical investigation of three-dimensional cloud cavitation with special emphasis on collapse induced shock dynamics," *Physics of Fluids*, 20, pp. 040703.1-9.
- Senocak I., Shyy, W., 2002, "A pressure-based method for turbulent cavitating flow computations," *Journal of Computational Physics*, 176, pp. 363-383.
- Sedlar, M., Zima, P., Muller, M., 2009, "CFD analysis of cavitation erosion potential in hydraulic machinery," 3rd IAHR International Meeting of the Workgroup on Cavitation and Dynamic Problems in Hydraulic Machinery and System, Brno, Czech Republic, 14-16 October.
- Serebryakov, V.V., 2001, "Some models of prediction of supercavitating flows based on slender body approximation," 4th International Symposium on Cavitation, California, USA, 20-23 June.
- Shafaghat R, Hosseinalipour SM, Nouri NM, Lashgari I. Shape optimization of two-dimensional cavitators in supercavitating flows using NSGA II algorithm. *Appl Ocean Res* 2009; 30: 305-310.
- Shen, Y.T., Dimotakis, P.E., 1989, "The Influence of Surface Cavitation on Hydrodynamic Forces," 22nd American Towing Tank Conference, St.

John's, Canada.

- Shih, T.H., Liou, W.W., Shabbir, A., Yang, Z., Zhu, Z., 1995, "A new $k-\epsilon$ eddy-viscosity model for high Reynolds number turbulent flows - model development and validation," *Computers & Fluids*, 24(3), pp. 227–238.
- Shin, B.R., 2011, "A high resolution numerical scheme for a high speed gas-liquid two-phase flow," *Journal of Mechanical Science and Technology*, 25(2), pp. 1373-1379.
- Simpson, T.W., Mauery, T.M., Korte, J.J., Mistree, F., 1998, "Comparison of response surface and kriging models for multidisciplinary design optimization," AIAA-98-4755, 7th AIAA/USAF/NASA/ISSMO Symposium on Multidisciplinary Analysis & Optimization, St. Louis, MO.
- Singhal, A.K., Athavale, M.M., Li, H., Jiang, Y., 2002, "Mathematical basis and validation of the full cavitation model," *Journal of Fluids Engineering*, 124, pp. 617-624.
- Singhal, A.K., Athavale, M.M., Li, H., and Jiang, Y., 2002, "Mathematical Basis and Validation of the Full Cavitation Model," *Journal of Fluids Engineering*, 124, pp. 617-624.
- Soyama, H., Futakawa, M., 2004, "Estimation of incubation time of cavitation erosion for various cavitating conditions," *Tribology Letters*, 17(1), pp. 27-30.
- Soyama, H., Kumano, H., Saka, M., 2001, "A new parameter to predict cavitation erosion," 4th International Symposium on Cavitation, Pasadena, California, USA, 20-23 June.
- Spalart, P.R., Allmaras, S.R., 1992, "A one equation turbulence model for

- aerodynamic flows,” 30th AIAA Aerospace Science Meeting & Exhibition, AIAA Paper 92-439, Reno, NV, 6-9 January.
- Stephanis, C.G. Hatiris, J.G. Mourmouras, D.E., 1997, “The process (mechanism) of erosion of soluble brittle materials caused by cavitation,” *Ultrasonics Sonochemistry*, 4, pp. 269-271.
- Szkodo, M., 2008, “Mathematical description and evaluation of cavitation erosion resistance of materials,” *Journal of Materials Processing Technology*, 164-165, pp. 1631-1636.
- van Terwisga, T.J.C., Fitzsimmons, P.A., Ziru, L., Foeth, E.J., 2009, “Cavitation erosion – a review of physical mechanisms and erosion risk models,” 7th International Symposium on Cavitation. Ahn Arbor, Michigan, USA, 17-22 August.
- Varghese, A.N., Uhlman, J.S., Kirschner, I.N., 2005, “Numerical analysis of high-speed bodies in partially cavitating axisymmetric flow,” *Journal of Fluids Engineering*, 127, pp.41-54.
- Venkateswaran, S., Lindau, J.W., Kunz, R.F., Merkle, C.L., 2002, “Computation of multiphase mixture flows with compressibility effects,” *Journal of Computational Physics*, 180, pp. 54-77.
- Wallis, G.B., 1969, “One dimensional two-phase flow,” McGraw-Hill, New York.
- Welch, W.J., Yu, T.-K., Kang, S.M. and Sacks, J., 1990, “Computer Experiments for Quality Control by Parameter Design,” *Journal of Quality Technology*, 22(1), pp. 15-22.
- Wu, X., Chahine, G.L., 2007, “Characterization of the content of the cavity

behind a high-speed supercavitating body,” *Journal of Fluids Engineering*,
129, pp.136-145.

Appendix

Cavitation erosion coefficient by kriging metamodel

<i>Re</i>	σ	C_{ce}	<i>Re</i>	σ	C_{ce}
2.7500	2.0000	66.8200	3.3421	2.0000	66.8169
2.7500	2.2158	66.8336	3.3421	2.2158	66.8242
2.7500	2.4316	66.8691	3.3421	2.4316	66.8426
2.7500	2.6474	66.9546	3.3421	2.6474	66.8855
2.7500	2.8632	67.1446	3.3421	2.8632	66.9767
2.7500	3.0789	67.5336	3.3421	3.0789	67.1541
2.7500	3.2947	68.2663	3.3421	3.2947	67.4678
2.7500	3.5105	69.5343	3.3421	3.5105	67.9698
2.7500	3.7263	71.5464	3.3421	3.7263	68.6922
2.7500	3.9421	74.4677	3.3421	3.9421	69.6188
2.7500	4.1579	78.3390	3.3421	4.1579	70.6673
2.7500	4.3737	83.0101	3.3421	4.3737	71.7039
2.7500	4.5895	88.1273	3.3421	4.5895	72.6037
2.7500	4.8053	93.2021	3.3421	4.8053	73.3394
2.7500	5.0211	97.7389	3.3421	5.0211	74.0472
2.7500	5.2368	101.3600	3.3421	5.2368	75.0063
2.7500	5.4526	103.8581	3.3421	5.4526	76.5058
2.7500	5.6684	105.1537	3.3421	5.6684	78.6495
2.7500	5.8842	105.2046	3.3421	5.8842	81.2094
2.7500	6.1000	103.9511	3.3421	6.1000	83.6372

Re	σ	C_{ce}	Re	σ	C_{ce}
3.9342	2.0000	66.8136	4.5263	2.0000	66.8110
3.9342	2.2158	66.8143	4.5263	2.2158	66.8067
3.9342	2.4316	66.8152	4.5263	2.4316	66.7944
3.9342	2.6474	66.8145	4.5263	2.6474	66.7610
3.9342	2.8632	66.8056	4.5263	2.8632	66.6778
3.9342	3.0789	66.7701	4.5263	3.0789	66.4860
3.9342	3.2947	66.6657	4.5263	3.2947	66.0782
3.9342	3.5105	66.4104	4.5263	3.5105	65.2799
3.9342	3.7263	65.8693	4.5263	3.7263	63.8450
3.9342	3.9421	64.8601	4.5263	3.9421	61.4845
3.9342	4.1579	63.1939	4.5263	4.1579	57.9495
3.9342	4.3737	60.7655	4.5263	4.3737	53.1662
3.9342	4.5895	57.6733	4.5263	4.5895	47.3914
3.9342	4.8053	54.3200	4.5263	4.8053	41.3092
3.9342	5.0211	51.4139	4.5263	5.0211	35.9855
3.9342	5.2368	49.8159	4.5263	5.2368	32.6300
3.9342	5.4526	50.2475	4.5263	5.4526	32.2149
3.9342	5.6684	52.9720	4.5263	5.6684	35.0966
3.9342	5.8842	57.6113	4.5263	5.8842	40.8230
3.9342	6.1000	63.2168	4.5263	6.1000	48.2419

Re	σ	C_{ce}	Re	σ	C_{ce}
5.1184	2.0000	66.8093	5.7105	2.0000	66.8077
5.1184	2.2158	66.8026	5.7105	2.2158	66.8008
5.1184	2.4316	66.7837	5.7105	2.4316	66.7818
5.1184	2.6474	66.7346	5.7105	2.6474	66.7329
5.1184	2.8632	66.6165	5.7105	2.8632	66.6162
5.1184	3.0789	66.3533	5.7105	3.0789	66.3592
5.1184	3.2947	65.8113	5.7105	3.2947	65.8360
5.1184	3.5105	64.7814	5.7105	3.5105	64.8533
5.1184	3.7263	62.9801	5.7105	3.7263	63.1533
5.1184	3.9421	60.0897	5.7105	3.9421	60.4540
5.1184	4.1579	55.8550	5.7105	4.1579	56.5375
5.1184	4.3737	50.2313	5.7105	4.3737	51.3800
5.1184	4.5895	43.5394	5.7105	4.5895	45.2840
5.1184	4.8053	36.5504	5.7105	4.8053	38.9424
5.1184	5.0211	30.4151	5.7105	5.0211	33.3678
5.1184	5.2368	26.4056	5.7105	5.2368	29.6636
5.1184	5.4526	25.5260	5.7105	5.4526	28.6923
5.1184	5.6684	28.1452	5.7105	5.6684	30.7709
5.1184	5.8842	33.8220	5.7105	5.8842	35.5330
5.1184	6.1000	41.4236	5.7105	6.1000	42.0330

<i>Re</i>	σ	C_{ce}	<i>Re</i>	σ	C_{ce}
6.3026	2.0000	66.8027	6.8947	2.0000	66.7844
6.3026	2.2158	66.7973	6.8947	2.2158	66.7814
6.3026	2.4316	66.7825	6.8947	2.4316	66.7734
6.3026	2.6474	66.7440	6.8947	2.6474	66.7503
6.3026	2.8632	66.6517	6.8947	2.8632	66.6911
6.3026	3.0789	66.4485	6.8947	3.0789	66.5572
6.3026	3.2947	66.0362	6.8947	3.2947	66.2827
6.3026	3.5105	65.2658	6.8947	3.5105	65.7684
6.3026	3.7263	63.9406	6.8947	3.7263	64.8849
6.3026	3.9421	61.8482	6.8947	3.9421	63.4936
6.3026	4.1579	58.8283	6.8947	4.1579	61.4914
6.3026	4.3737	54.8703	6.8947	4.3737	58.8750
6.3026	4.5895	50.2101	6.8947	4.5895	55.8017
6.3026	4.8053	45.3731	6.8947	4.8053	52.6165
6.3026	5.0211	41.1178	6.8947	5.0211	49.8128
6.3026	5.2368	38.2632	6.8947	5.2368	47.9205
6.3026	5.4526	37.4457	6.8947	5.4526	47.3495
6.3026	5.6684	38.8995	6.8947	5.6684	48.2506
6.3026	5.8842	42.3598	6.8947	5.8842	50.4561
6.3026	6.1000	47.1418	6.8947	6.1000	53.5302

<i>Re</i>	σ	C_{ce}	<i>Re</i>	σ	C_{ce}
7.4868	2.0000	66.7261	8.0789	2.0000	66.5643
7.4868	2.2158	66.7268	8.0789	2.2158	66.5718
7.4868	2.4316	66.7289	8.0789	2.4316	66.5928
7.4868	2.6474	66.7252	8.0789	2.6474	66.6198
7.4868	2.8632	66.7017	8.0789	2.8632	66.6403
7.4868	3.0789	66.6340	8.0789	3.0789	66.6371
7.4868	3.2947	66.4827	8.0789	3.2947	66.5864
7.4868	3.5105	66.1897	8.0789	3.5105	66.4570
7.4868	3.7263	65.6805	8.0789	3.7263	66.2107
7.4868	3.9421	64.8758	8.0789	3.9421	65.8086
7.4868	4.1579	63.7178	8.0789	4.1579	65.2228
7.4868	4.3737	62.2063	8.0789	4.3737	64.4552
7.4868	4.5895	60.4332	8.0789	4.5895	63.5537
7.4868	4.8053	58.5970	8.0789	4.8053	62.6201
7.4868	5.0211	56.9802	8.0789	5.0211	61.7974
7.4868	5.2368	55.8843	8.0789	5.2368	61.2380
7.4868	5.4526	55.5420	8.0789	5.4526	61.0590
7.4868	5.6684	56.0390	8.0789	5.6684	61.3035
7.4868	5.8842	57.2810	8.0789	5.8842	61.9247
7.4868	6.1000	59.0233	8.0789	6.1000	62.8001

Re	σ	C_{ce}	Re	σ	C_{ce}
8.6711	2.0000	66.1659	9.2632	2.0000	65.2942
8.6711	2.2158	66.1881	9.2632	2.2158	65.3472
8.6711	2.4316	66.2499	9.2632	2.4316	65.4954
8.6711	2.6474	66.3378	9.2632	2.6474	65.7090
8.6711	2.8632	66.4327	9.2632	2.8632	65.9489
8.6711	3.0789	66.5141	9.2632	3.0789	66.1769
8.6711	3.2947	66.5620	9.2632	3.2947	66.3635
8.6711	3.5105	66.5581	9.2632	3.5105	66.4911
8.6711	3.7263	66.4848	9.2632	3.7263	66.5522
8.6711	3.9421	66.3273	9.2632	3.9421	66.5470
8.6711	4.1579	66.0767	9.2632	4.1579	66.4805
8.6711	4.3737	65.7376	9.2632	4.3737	66.3627
8.6711	4.5895	65.3343	9.2632	4.5895	66.2099
8.6711	4.8053	64.9147	9.2632	4.8053	66.0456
8.6711	5.0211	64.5439	9.2632	5.0211	65.8984
8.6711	5.2368	64.2911	9.2632	5.2368	65.7973
8.6711	5.4526	64.2087	9.2632	5.4526	65.7639
8.6711	5.6684	64.3163	9.2632	5.6684	65.8064
8.6711	5.8842	64.5930	9.2632	5.8842	65.9165
8.6711	6.1000	64.9844	9.2632	6.1000	66.0727

Re	σ	C_{ce}	Re	σ	C_{ce}
9.8553	2.0000	63.6010	10.4474	2.0000	60.6944
9.8553	2.2158	63.7135	10.4474	2.2158	60.9089
9.8553	2.4316	64.0279	10.4474	2.4316	61.5082
9.8553	2.6474	64.4824	10.4474	2.6474	62.3748
9.8553	2.8632	64.9961	10.4474	2.8632	63.3553
9.8553	3.0789	65.4918	10.4474	3.0789	64.3040
9.8553	3.2947	65.9135	10.4474	3.2947	65.1162
9.8553	3.5105	66.2332	10.4474	3.5105	65.7414
9.8553	3.7263	66.4475	10.4474	3.7263	66.1772
9.8553	3.9421	66.5691	10.4474	3.9421	66.4520
9.8553	4.1579	66.6182	10.4474	4.1579	66.6069
9.8553	4.3737	66.6155	10.4474	4.3737	66.6817
9.8553	4.5895	66.5806	10.4474	4.5895	66.7085
9.8553	4.8053	66.5308	10.4474	4.8053	66.7101
9.8553	5.0211	66.4820	10.4474	5.0211	66.7020
9.8553	5.2368	66.4472	10.4474	5.2368	66.6938
9.8553	5.4526	66.4357	10.4474	5.4526	66.6912
9.8553	5.6684	66.4509	10.4474	5.6684	66.6964
9.8553	5.8842	66.4901	10.4474	5.8842	66.7090
9.8553	6.1000	66.5458	10.4474	6.1000	66.7269

<i>Re</i>	σ	C_{ce}	<i>Re</i>	σ	C_{ce}
11.0395	2.0000	56.3149	11.6316	2.0000	50.5891
11.0395	2.2158	56.6829	11.6316	2.2158	51.1578
11.0395	2.4316	57.7113	11.6316	2.4316	52.7471
11.0395	2.6474	59.1985	11.6316	2.6474	55.0456
11.0395	2.8632	60.8814	11.6316	2.8632	57.6465
11.0395	3.0789	62.5104	11.6316	3.0789	60.1643
11.0395	3.2947	63.9066	11.6316	3.2947	62.3226
11.0395	3.5105	64.9840	11.6316	3.5105	63.9889
11.0395	3.7263	65.7397	11.6316	3.7263	65.1588
11.0395	3.9421	66.2237	11.6316	3.9421	65.9101
11.0395	4.1579	66.5072	11.6316	4.1579	66.3529
11.0395	4.3737	66.6587	11.6316	4.3737	66.5930
11.0395	4.5895	66.7316	11.6316	4.5895	66.7127
11.0395	4.8053	66.7624	11.6316	4.8053	66.7674
11.0395	5.0211	66.7730	11.6316	5.0211	66.7903
11.0395	5.2368	66.7759	11.6316	5.2368	66.7990
11.0395	5.4526	66.7770	11.6316	5.4526	66.8022
11.0395	5.6684	66.7791	11.6316	5.6684	66.8038
11.0395	5.8842	66.7829	11.6316	5.8842	66.8051
11.0395	6.1000	66.7881	11.6316	6.1000	66.8065

Re	σ	C_{ce}	Re	σ	C_{ce}
12.2237	2.0000	44.2301	12.8158	2.0000	38.5001
12.2237	2.2158	45.0218	12.8158	2.2158	39.4926
12.2237	2.4316	47.2340	12.8158	2.4316	42.2661
12.2237	2.6474	50.4333	12.8158	2.6474	46.2773
12.2237	2.8632	54.0538	12.8158	2.8632	50.8163
12.2237	3.0789	57.5585	12.8158	3.0789	55.2104
12.2237	3.2947	60.5629	12.8158	3.2947	58.9771
12.2237	3.5105	62.8826	12.8158	3.5105	61.8855
12.2237	3.7263	64.5115	12.8158	3.7263	63.9278
12.2237	3.9421	65.5580	12.8158	3.9421	65.2400
12.2237	4.1579	66.1755	12.8158	4.1579	66.0144
12.2237	4.3737	66.5111	12.8158	4.3737	66.4354
12.2237	4.5895	66.6793	12.8158	4.5895	66.6466
12.2237	4.8053	66.7572	12.8158	4.8053	66.7446
12.2237	5.0211	66.7904	12.8158	5.0211	66.7866
12.2237	5.2368	66.8036	12.8158	5.2368	66.8033
12.2237	5.4526	66.8084	12.8158	5.4526	66.8095
12.2237	5.6684	66.8102	12.8158	5.6684	66.8116
12.2237	5.8842	66.8110	12.8158	5.8842	66.8123
12.2237	6.1000	66.8114	12.8158	6.1000	66.8126

<i>Re</i>	σ	C_{ce}	<i>Re</i>	σ	C_{ce}
13.4079	2.0000	34.8409	14.0000	2.0000	34.2938
13.4079	2.2158	35.9616	14.0000	2.2158	35.4338
13.4079	2.4316	39.0937	14.0000	2.4316	38.6194
13.4079	2.6474	43.6232	14.0000	2.6474	43.2264
13.4079	2.8632	48.7489	14.0000	2.8632	48.4398
13.4079	3.0789	53.7109	14.0000	3.0789	53.4867
13.4079	3.2947	57.9644	14.0000	3.2947	57.8130
13.4079	3.5105	61.2487	14.0000	3.5105	61.1535
13.4079	3.7263	63.5550	14.0000	3.7263	63.4992
13.4079	3.9421	65.0367	14.0000	3.9421	65.0063
13.4079	4.1579	65.9113	14.0000	4.1579	65.8959
13.4079	4.3737	66.3867	14.0000	4.3737	66.3795
13.4079	4.5895	66.6253	14.0000	4.5895	66.6222
13.4079	4.8053	66.7360	14.0000	4.8053	66.7348
13.4079	5.0211	66.7836	14.0000	5.0211	66.7831
13.4079	5.2368	66.8025	14.0000	5.2368	66.8023
13.4079	5.4526	66.8094	14.0000	5.4526	66.8094
13.4079	5.6684	66.8118	14.0000	5.6684	66.8119
13.4079	5.8842	66.8126	14.0000	5.8842	66.8126
13.4079	6.1000	66.8128	14.0000	6.1000	66.8129

초 록

캐비테이션 침식은 프로펠러, 펌프, 터빈, 노즐 등 유체기계 장치에서 흔히 관찰되며 오랜 기간 동안 연구되어 왔다. 그러나 캐비테이션 침식 자체에 대한 연구는 많이 진행된 반면 캐비테이션을 예측할 수 있는 방법에 대한 연구는 많이 이루어지지 않았다. 이에 본 연구에서는 유체기계 장치의 성능에 치명적인 영향력을 미치는 캐비테이션 침식을 예측할 수 있는 실용적인 방법을 개발하였다.

캐비테이션 침식을 예측하는 실용적인 방법을 개발하기 위해 캐비티가 붕괴될 때의 충격과 속도와 표면의 침식이 유발되는 임계 속도를 정의하였다. 충격과 속도가 임계 속도보다 크면 캐비테이션 침식이 발생했다고 예측할 수 있다. 충격과 속도의 미계수를 결정하기 위해 전산유체역학 해석을 도입하였다.

전산유체역학을 이용하여 캐비테이션 유동장을 구현하기 위하여 소스공개 라이브러리를 이용하여 압력기반 비압축성, 등온 압축성 유동 해석자를 개발하였다. 셀 중심 방법을 이용하였으며, 대류항 TVD 스킴, 확산항은 중앙차분 도식, 난류값들은 2차의 상류차분 도식을 사용하여 이산화하였다.

개발된 해석자를 검증하기 위하여 비압축성, 등온 압축성 캐비테이션 유동장을 구현하였으며, 실험결과와 비교하였다.

비압축성 캐비테이션 유동장에 대해서는 얇은 층, 초, 구름형 캐비테이션을 구현하였다. 반구형 전두부 실린더에서 발생하는 얇은 층 캐비테이션을 구현하였고, 실험결과와의 비교를 통해 캐비테이션, 난류 모델을 선정하였다. Modified NACA66 수중익 (Brockett, 1966) 주위에 발생하는 얇은 층 캐비테이션을 구현하였으며, 실험결과와의 비교를 통해 캐비테이션 모델에 포함된 캐비티 생성과 소멸 계수를 선정하였다. 삼각형 형상의 캐비테이터 뒤에서 발생하는 초 캐비테이션에 대해 계산하였다. 계산된 캐비티의 길이는 해석해 및 비점성 유동 해석 해석자의 결과와 잘 일치하였다. 캐비테이터를 실제 문제에 적용하기 위하여 캐비테이터 뒤에 몸체를 붙여 계산하였으며, 실험결과와 비교를 통해 해석자의 정도를 검토하였다. 3차원 비틀어진 수중익 (Foeth, 2008) 주위에서 발생하는 구름형 캐비테이션을 구현하였다. 캐비티의 방출은 캐비티의 끝에서 발생하는 재 돌입 제트(re-entrant jet)와 측면 돌입 제트(side entrant jet)에 의해 결정되는 것을 확인하였다. 계산된 양력과 방출주기인 Strouhal 수는 실험과 비교적 잘 일치하였다. 얇은 층, 초, 구름형 캐비테이션에 대한 구현을 통해 비압축성 유동 해석자를 검증하였다. 등온 압축성 유동 해석자를 검증하기 위해 반구형 전두부 실린더 주위에서 발생하는 얇은 층 캐비테이션을 해석하였다. 해석결과 압축성 효과가 포함된 등온 압축성 유동 해석자를 캐비티의 움직임을 잘 모사하는 것을 확인할 수 있었다.

따라서 캐비테이션 침식 유동장 모사를 위해 등은 압축성 유동 해석자를 선택하였다.

검증된 해석자를 이용하여 충격과 속도의 미 계수를 결정하기 위해 축소-확대 노즐(Keil et al., 2011)과 수중익(Dular and Coutier-Delgossa, 2009) 주위의 캐비테이션 유동장을 구현하였다. 캐비테이션 유동장 계산을 통해 특정한 캐비테이션 수와 레이놀즈 수에서의 캐비테이션 침식 계수를 도출하였다. 캐비테이션 침식 계수는 메타모델링 방법과 곡선 맞춤법을 이용하여 레이놀즈 수와 캐비테이션 수의 형태로 표현하였다. 메타모델링 방법에서는 비선형적인 문제에도 적합한 크리깅 메타모델을 선정하여 캐비테이션 침식 계수를 레이놀즈 수와 캐비테이션 수에 따른 반응면으로 도출하였다. 곡선 맞춤법에서는 캐비테이션 수의 함수는 지수함수로 표현하였으며, 레이놀즈 수의 함수는 레이놀즈 수의 영향을 적게 하기 위하여 로그 함수의 형태로 표현하였다.

개발된 캐비테이션 침식 방법을 검증하기 위해 축 대칭 노즐 (Franc, 2009)의 캐비테이션 유동장을 해석하였다. 계산된 캐비테이션 침식 영역은 실험과 비교했을 때 유사한 위치인 것을 확인하였다. 끝으로 개발된 캐비테이션 침식 방법을 이용하여 선박 프로펠러에서 발생하는 캐비테이션 침식을 추정하였다. 추정결과, 실제 캐비테이션 침식이 발생한 위치와 추정결과가 유사한 위치인 것을 확인하였다.

본 논문에서 전산유체역학을 이용하여 캐비테이션 침식을 추정할 수 있는 실용적인 방법을 개발하였으며, 추진기, 펌프, 터빈, 노즐 등의 유체기계에서 발생하는 캐비테이션 침식을 예측하는데 유용하게 활용될 것으로 판단된다. 향후 버블 캐비테이션, 재료의 피로, 캐비티의 방출 주기를 고려한 캐비테이션 침식방법에 대한 연구가 필요하다. 또한, 실선의 추진기 캐비테이션 침식 추정을 위한 고 레이놀즈 수를 만족하는 캐비테이션 침식 추정방법에 대한 연구가 필요하다.

주요어: 캐비테이션, 캐비테이션 침식, 전산유체역학

학 번: 2009-30283